

FACILITY EFFECTS ON HELICON THRUSTER OPERATION

A Dissertation
Presented to
The Academic Faculty

By

Natalie R. S. Caruso

In Partial Fulfillment
Of the Requirements for the Degree
Doctor of Philosophy in Aerospace Engineering

Georgia Institute of Technology

May 2016

Copyright © Natalie R. S. Caruso 2016

FACILITY EFFECTS ON HELICON THRUSTER OPERATION

Approved by:

Dr. Mitchell Walker, Advisor
School of Aerospace Engineering
Georgia Institute of Technology

Dr. Jerry Seitzman
School of Aerospace Engineering
Georgia Institute of Technology

Dr. Wenting Sun
School of Aerospace Engineering
Georgia Institute of Technology

Dr. Suresh Menon
School of Aerospace Engineering
Georgia Institute of Technology

Dr. Sven Simon
Earth & Atmospheric Sciences
Georgia Institute of Technology

Date Approved: March 31, 2016

To my family for their boundless love and support.

ACKNOWLEDGEMENTS

Writing the acknowledgements section of my thesis holds a finality I have been looking forward to for a while. I think at this stage elation usually kicks in and the acknowledgements section is a summary of happy or poignant memories but to pretend my victory is not hard won would cheapen its value. I would prefer to honor the wound and instead acknowledge that I did not quit when quitting often felt so easy to do. Perhaps the ultimate benefit of attending graduate school is admittance into an exclusive group in which you can commiserate over the frustrations of graduate school. Regardless of its difficulty, graduate school has had many silver linings. What I will take with me after I graduate are the memories of the people who have come to mean so much to me during my tenure at Georgia Tech.

First of all, I would like to thank my advisor Dr. Mitchell Walker for taking me on as his student and for assisting me throughout my graduate career. I would also like to thank my committee members Dr. Seitzman, Dr. Sun, Dr. Menon, and Dr. Simon for reviewing my work and guiding my dissertation effort. In addition to my thesis committee, Dr. Juan Rogers was of great help in understanding my uncertainty analysis and I thank him for his many emails from the other side of the globe. Also, no experiment would be successful without the support of the AE machine shop and I thank the men there for taking the time to review my drawings and work within my timelines to ensure I was able to achieve success.

To Jeremy Mitchell, I am greatly indebted for all of your time and patience in helping me to find and repair (and repeatedly repair) VTF-1 over the last several years. Your help

in keeping the lights on and the chamber running has been invaluable. You have also been a good sounding board and friend. I would also like to thank Dr. Jagoda whose support and guidance helped me to clear my initial grad school hurdles.

Jason, I hope you will find the support you need to run the lab in Nathan and Connie. With their support and your lead, I think the lab will do just fine. Tom, I hope you find what you are seeking in a professional appointment. You have been a great resource during your term at the lab and I hope future students will get a chance to benefit from your wisdom. To Cheung, Tyler, and Christian, I have heard that life after lab is very fruitful and I wish you all the best. To Alex, who originally worked on the UW-Helicon project, I send my eternal thanks for your documentation and for the millions of pictures you took during its operation... for I took none. To Sherrie, keep at it! I know you will graduate soon enough.

Lake, you were one of the first faces I met when I first started work at the lab. Thank you for being a one-man welcome wagon to Atlanta. Gabi, I wish your time at the lab would have been longer but you certainly made the lab a great place to work in its heyday. I enjoyed your friendship. Logan and Gabe, you guys pretty much built the lab, both in equipment and personnel archetypes. You guys were great teachers in beating the grad school game (if that game also happens to be StarCraft). Logan, I gave life its lemons back... and thank you for your manifesto, it was critical in finishing my thesis. Scott, thank you for trying to make the lab more than just a place to work. Despite basketball being an inferior sport, I always loved hanging out with you. Aaron, thank you for the entertaining stories and that great brain of yours. You have been a valuable

colleague and great company. Sebastiano, I do not think the lab ever recovered from your departure... no, really.

Alex, Aude, and Scottie, you three have been a haven in the storm. Daniel, you are my rock. Without all your Star Trek themed gifts and grad school commiseration (and editing of my papers including this acknowledgements section), I would not have made it. Jon and Lizzie, thank you for being family. Thank you for outrageous adventures like campus movie-fest film making and irreplaceable memories like 'the margarita night'. You have been people I could always turn to for support and a laugh. To Brenna, Greg, and Kris, thank you for being great friends and all our game nights. Will, I think of you every time I walk through the student center; I miss our lunches.

Sam, it has been hard being at the lab without you since you left and moved on to grander science. I have missed your optimism (however misguided) and your strength. Your friendship has been one of the best things to come from my graduate school experience. My last day at the lab, I will lift my mug of Maxwell House coffee, brewed using the 'Samuel J. Langendorf Memorial Coffee Maker,' to the rubber bands you shot into the HVAC grate in the third office ceiling in commemoration of this crazy journey we shared together. I will then whip some rocks at the security guard's car for good measure.

To my parents, Kurt and Maria, I owe everything. You have always supported me and let me choose my own path... even if it's the toughest path on the map. And to my brother Paul, thank you for your faith, your love, and often reminding me that I am the unstoppable big sister.

And finally, to my husband Brent, Atlanta has brought us closer and made us stronger. You are my best friend and your support has given me the courage to pursue my dreams. I am grateful for your love and for our son Owen. I am excited to start this new and exciting journey with you by my side.

TABLE OF CONTENTS

| | |
|---|--------|
| Acknowledgments..... | iv |
| List of Tables | xi |
| List of Figures | xiii |
| Nomenclature | xxi |
| Summary | xxiii |
| Chapter I Introduction..... | 1 |
| 1.1 Electric Propulsion: Devices and Testing Practices..... | 1 |
| 1.1.1 Electric Propulsion Devices..... | 1 |
| 1.1.2 Vacuum Test Facilities | 3 |
| Chapter II Helicon Ion Thrusters..... | 5 |
| 2.1 Helicon Ion Thruster Operation | 5 |
| 2.1.1 Thruster Design | 5 |
| 2.1.2 Thrust Calculation | 8 |
| 2.1.3 Benefits..... | 10 |
| 2.2 Helicon Ion Thruster Performance | 11 |
| 2.2.1 Radio Frequency Coupling Modes..... | 11 |
| 2.2.2 Acceleration Mechanism: Double Layer Theory | 14 |
| Chapter III Facility Effects | 18 |
| 3.1 Helicon Ion Thruster Facility Effects | 18 |
| 3.1.1 Facility Effect Susceptibility | 18 |
| 3.1.2 Anticipated Results of Facility Effects..... | 20 |
| 3.2 Neutral Ingestion | 22 |
| 3.2.1 Predicted Ingestion Calculations | 22 |
| Chapter IV Research Questions | 25 |
| 4.1 Operating Pressure Conditions..... | 25 |
| 4.2 Neutral Ingestion Effects on Plasma Properties | 25 |
| 4.3 Neutral Ingestion Effects on Operating Parameters | 27 |
| 4.4 Neutral Ingestion at the 'High-Pressure Condition' versus Increased Volumetric Flow Rate at the 'Low-Pressure Condition' | 28 |
| 4.5 Neutral Ingestion Effects on RF Coupling Mode and Double Layer Formation | 29 |

| | | |
|------------|---|----|
| Chapter V | Experimental Set-up | 30 |
| 5.1 | Helicon Ion Thruster | 30 |
| 5.1.1 | MadHeX Replica | 30 |
| 5.2 | Vacuum Test Facility-1 | 32 |
| 5.2.1 | High-Pressure Condition | 34 |
| 5.2.2 | Low-Pressure Condition | 34 |
| 5.3 | Diagnostics | 34 |
| 5.3.1 | RF Compensated Emissive Probe | 34 |
| 5.3.2 | Retarding Potential Analyzer | 38 |
| 5.3.3 | RF-Compensated Langmuir Probe | 40 |
| 5.4 | Uncertainty Analysis | 42 |
| Chapter VI | Results | 44 |
| 6.1 | Neutral Ingestion Effects on Plasma Properties | 44 |
| 6.1.1 | Neutral Ingestion Effects on Plasma Properties at the ‘High-Pressure Condition’ | 44 |
| 6.1.2 | Neutral Ingestion Effects on Plasma Properties at the ‘Low-Pressure Condition’ | 48 |
| 6.1.3 | Comparison of Neutral Ingestion Effects on Plasma Properties Between Both Pressure Conditions | 52 |
| 6.2 | Neutral Ingestion Effects and Operating Parameters | 55 |
| 6.2.1 | Effect of Increasing RF Power on Neutral Ingestion Influence at the ‘High- Pressure Condition’ | 56 |
| 6.2.2 | Effect of Increasing RF Power on Neutral Ingestion Influence at the ‘Low- Pressure Condition’ | 60 |
| 6.2.3 | Comparison of the Effect of Increasing RF Power on Neutral Ingestion Influence at Both Pressure Conditions | 63 |
| 6.2.4 | Effect of Increasing Magnetic Field Strength on Neutral Ingestion Influence at the ‘High-Pressure Condition’ | 66 |
| 6.2.5 | Effect of Increasing Magnetic Field Strength on Neutral Ingestion Influence at the ‘Low-Pressure Condition’ | 69 |
| 6.2.6 | Comparison of the Effect of Increasing Magnetic Field Strength on Neutral Ingestion Influence at Both Pressure Conditions | 71 |
| 6.3 | The Effects of Increased Volumetric Flow Rate at the ‘Low-Pressure Condition’ Compared to the Effects of Neutral Ingestion at the ‘High Pressure Condition’ | 74 |
| 6.3.1 | Results | 74 |
| 6.4 | Neutral Ingestion Effects on Double Layer Formation and RF Coupling Mode Transitions | 78 |
| 6.4.1 | Double Layer | 78 |
| 6.4.2 | RF Coupling Modes | 80 |

| | |
|--|---------|
| Chapter VII Analysis | 81 |
| 7.1 Effects of Neutral Ingestion on Plasma Properties..... | 81 |
| 7.1.1 Ion-Neutral Collisions | 81 |
| 7.1.2 Plume Ionization..... | 85 |
| 7.1.3 Thrust Augmentation..... | 88 |
| 7.1.4 Electron Cooling..... | 94 |
| 7.1.5 Summary | 94 |
| 7.2 Neutral Ingestions Effects on Increasing RF Power and Performance | |
| Metrics..... | 95 |
| 7.2.1 RF Forward Power Absorption by Environmental Neutrals | 95 |
| 7.2.2 Neutral Ingestion Effects on Collision Frequency and Plume Ionization at | |
| Increasing RF Power | 98 |
| 7.2.3 Neutral Ingestion Effects on RF Coupling Mode Transitions at Increasing RF | |
| Power..... | 102 |
| 7.2.4 Neutral Ingestion Effects on Double Layer formation at Increasing RF | |
| Power..... | 103 |
| 7.2.5 Magnitude of Estimated Thrust Augmentation due to Neutral Ingestion | |
| While Increasing RF Power | 104 |
| 7.2.6 Summary of Neutral Ingestion Effects with Increasing RF Power on Thrust | |
| Generation, Plasma Properties, RF Coupling Mode Transition, and Double | |
| Layer Formation | 106 |
| 7.3 Neutral Ingestions Effects and Increasing Magnetic Field Strength..... | 107 |
| 7.3.1 Neutral Ingestion Effects on Charge Exchange Collisions and Plume | |
| Ionization at Increasing Magnetic Field Strength | 108 |
| 7.3.2 Thrust Augmentation and Increasing Magnetic Field Strength | 110 |
| 7.3.3 Summary of Neutral Ingestion Effects while Increasing Magnetic Field | |
| Strength on Thrust Generation and Plasma Properties..... | 112 |
| 7.4 Volumetric Flow Rate Effects at the ‘Low-Pressure Condition’ | 112 |
| 7.4.1 Trends of Increasing Volumetric Flow Rate Compared to Neutral Ingestion | |
| Trends..... | 113 |
| 7.4.2 Summary of Increased Volumetric Flow Rate Effects and Neutral Ingestion | |
| Effects..... | 114 |
| Chapter VIII Conclusions | 116 |
| 8.1 Effect of Neutral Ingestion on Helicon Ion Thruster Operation | 116 |
| 8.2 Future Work | 118 |
| Appendix A: Derivation of Quasi-1-D Model of Thrust Force for an Expanding Plasma in | |
| a Magnetic Nozzle | 119 |
| Appendix B: Diagram of Neutral Ingestion Effects on MadHeX Replica | 122 |
| References..... | 123 |

LIST OF TABLES

| | | |
|-----|--|----|
| 2.1 | Ionization physics explanations and ion density profile information for the capacitive, inductive and Helicon RF coupling modes..... | 13 |
| 3.1 | Calculated neutral ingestion volumetric flow rates for the MadHeX Replica in an argon environment | 23 |
| 5.1 | Summary of equipment and diagnostic uncertainty..... | 43 |
| 5.2 | Plasma property uncertainties due to diagnostic and analysis errors specific to the presented experimental results in Chapter VI of this work..... | 43 |
| 6.1 | Differences in most probable voltages (corrected and uncorrected) recorded on thruster centerline for 2 sccm argon volumetric flow rate, 100 W RF power, and 340 G magnetic field strength thruster operating conditions between the ‘low-pressure condition’ and the ‘high-pressure condition.’ | 53 |
| 7.1 | Comparison of argon neutral ingestion rates for both the ‘Low-Pressure Condition’ and ‘High-Pressure Condition’ at 2 sccm argon volumetric flow rate, 100 W RF power, and 340 G magnetic field strength thruster operation. | 83 |
| 7.2 | Charge exchange collision mean free paths (λ_{CT}) and momentum transfer mean free paths (λ_{MT}) for both the ‘Low-Pressure Condition’ and ‘High-Pressure Condition’ at 2 sccm argon volumetric flow rate, 100 W RF power, and 340 G magnetic field strength thruster operation..... | 85 |
| 7.3 | Charge exchange collision frequencies (ν_{CT}) and momentum transfer collision frequencies (ν_{MT}) at the ‘High-Pressure Condition’ at 2 sccm argon volumetric flow rate, 100 W RF power, and 340 G magnetic field strength thruster operation | 85 |
| 7.4 | Mean free path lengths and ion production rates for plume neutral ionization for both the ‘Low-Pressure Condition’ and ‘High-Pressure Condition’ at 2 sccm argon volumetric flow rate, 100 W RF power, and 340 G magnetic field strength thruster operation for plume neutral ionization | 87 |
| 7.5 | Estimated thrust density contributions from the accelerated ion beam, electron pressure, and newly ionized plume neutrals calculated for the centerline ($r = 0$ m) at a location 66 mm downstream of the exit plane for both the ‘Low-Pressure Condition’ and ‘High-Pressure Condition’ at 2 sccm argon volumetric flow rate, 100 W RF power, and 340 G magnetic field strength thruster operation | 92 |

| | | |
|-----|---|-----|
| 7.6 | Comparison of the rate of increase in most probable voltage with increasing RF Power for 2 sccm argon volumetric flow rate and 340 G source region magnetic field strength between ‘Low-Pressure Condition’ and ‘High-Pressure Condition.’ | 96 |
| 7.7 | Comparison of charge exchange (v_{CT}) and momentum exchange (v_{MT}) collision frequencies at the ‘high-pressure condition’ at the exit plane at 2 sccm argon volumetric flow rate and 340 G magnetic field strength thruster operation for charge exchange collisions and plume argon ionization over an RF power range of ~100 W – ~500 W | 99 |
| 7.8 | Comparison of plume neutral ionization collision frequencies and production rates for both the ‘Low-Pressure Condition’ and the ‘High-Pressure Condition’ at the exit plane at 2 sccm argon volumetric flow rate and 340 G magnetic field strength thruster operation for charge exchange collisions and plume argon ionization over an RF power range of ~100 W – ~500 W | 99 |
| 7.8 | Comparison of plume ion production rates for both the ‘Low-Pressure Condition’ and the ‘High-Pressure Condition’ at the exit plane at 2 sccm argon volumetric flow rate and 100 W RF power thruster operation for charge exchange collisions and plume argon ionization over a magnetic field strength range of 340 G to 700 G | 110 |

LIST OF FIGURES

| | | |
|-----|---|----|
| 2.1 | Electrical diagram of a gridded ion thruster. Stage 1: Ionization. Stage 2. Ion Acceleration. Stage 3: Plume neutralization..... | 6 |
| 2.2 | Electrical diagram of a Helicon ion thruster tested at Georgia Tech (Left). Image of Helicon ion thruster with thruster stages labeled (Right). Stage 1: Ionization. Stage 2: Acceleration..... | 7 |
| 2.3 | MadHeX thruster operating on argon while immersed in a vacuum environment at Georgia Institute of Technology..... | 8 |
| 2.4 | Sample potential drop (ϕ) located at the boundary of the source region and exhaust plume..... | 15 |
| 5.1 | Fully assembled MadHeX replica. (Yard stick included for scale.)..... | 30 |
| 5.2 | MadHeX replica exit area. Centerline along which measurements are recorded denoted by axis; 0 coordinated corresponds to exit plane. | 31 |
| 5.3 | Vacuum Test Facility–1 at Georgia Tech..... | 33 |
| 5.4 | (Left) RF-compensated probe assembly with emissive probe tip attached and RF-compensation circuit. (Right) Tungsten loop probe tip. | 35 |
| 5.5 | (Left) Sample of smoothed I-V curves at multiple heating currents. (Right) Derivative curves of each I-V curve at different heating currents. | 35 |
| 5.6 | (Left) Sample plot of difference in ion current (ion current collected for the non-emitting case – ion current collected during emission) vs. the voltage at which the maximum derivative occurs. (Right) Sample linear trend line fitted to data to determine local plasma potential at point of zero emission. | 36 |
| 5.7 | Electrical schematic of four-grid, AFRL designed RPA. | 38 |
| 5.8 | Sample smoothed I-V curves from RPA (Left). Sample derivative trace of I-V curve (Right). | 39 |
| 5.9 | (Left) RF-compensated probe assembly with Langmuir probe tip attached and modified compensation circuit. (Right) Planar tungsten probe tip. | 40 |

| | | |
|------|--|----|
| 5.10 | (Left) Sample I-V curves from Langmuir probe voltage sweep. (Right) Sample log plot of I-V curve with intersecting trend lines to determine plasma potential | 41 |
| 6.1 | IEDFs recorded on thruster centerline for 2 sccm argon volumetric flow rate, 100 W RF power, and 340 G magnetic field strength thruster operating conditions at the ‘high-pressure condition.’ | 45 |
| 6.2 | Most probable voltages recorded on thruster centerline for 2 sccm argon volumetric flow rate, 100 W RF power, and 340 G magnetic field strength thruster operating conditions at the ‘high-pressure condition.’ | 45 |
| 6.3 | Potentials of interest recorded on thruster centerline by the emissive probe (E.P.) and the Langmuir probe (L.P.) for 2 sccm argon volumetric flow rate, 100 W RF power, and 340 G magnetic field strength thruster operating conditions at the ‘high-pressure condition.’ | 46 |
| 6.4 | Electron temperatures recorded on thruster centerline for 2 sccm argon volumetric flow rate, 100 W RF power, and 340 G magnetic field strength thruster operating conditions at the ‘high-pressure condition.’ | 47 |
| 6.5 | Ion densities recorded on thruster centerline for 2 sccm argon volumetric flow rate, 100 W RF power, and 340 G magnetic field strength thruster operating conditions at the ‘high-pressure condition.’ | 47 |
| 6.6 | IEDFs recorded on thruster centerline for 2 sccm argon volumetric flow rate, 100 W RF power, and 340 G magnetic field strength thruster operating conditions at the ‘low-pressure condition.’ | 49 |
| 6.7 | Most probable voltages recorded on thruster centerline for 2 sccm argon volumetric flow rate, 100 W RF power, and 340 G magnetic field strength thruster operating conditions at the ‘low-pressure condition.’ | 49 |
| 6.8 | Potentials of interest recorded on thruster centerline by the emissive probe (E.P.) and the Langmuir probe (L.P.) for 2 sccm argon volumetric flow rate, 100 W RF power, and 340 G magnetic field strength thruster operating conditions at the ‘low-pressure condition.’ | 51 |
| 6.9 | Electron temperature recorded on thruster centerline for 2 sccm argon volumetric flow rate, 100 W RF power, and 340 G magnetic field strength thruster operating conditions at the ‘low-pressure condition.’ | 51 |
| 6.10 | Ion number density recorded on thruster centerline for 2 sccm argon volumetric flow rate, 100 W RF power, and 340 G magnetic field strength thruster operating conditions at the ‘low-pressure condition.’ | 51 |

| | | |
|------|--|----|
| 6.11 | Most probable voltages recorded on thruster centerline for 2 sccm argon volumetric flow rate, 100 W RF power, and 340 G magnetic field strength thruster operating conditions at both the ‘low-pressure condition’ (Low P) and ‘high-pressure condition’ (High P)..... | 53 |
| 6.12 | Electron temperature recorded on thruster centerline for 2 sccm argon volumetric flow rate, 100 W RF power, and 340 G magnetic field strength thruster operating conditions at both the ‘low-pressure condition’ (Low P) and ‘high-pressure condition’ (High P)..... | 54 |
| 6.13 | Ion number density recorded on thruster centerline for 2 sccm argon volumetric flow rate, 100 W RF power, and 340 G magnetic field strength thruster operating conditions at both the ‘low-pressure condition’ (Low P) and ‘high-pressure condition’ (High P)..... | 54 |
| 6.14 | Ion saturation currents recorded on thruster centerline for 2 sccm argon volumetric flow rate, 100 W RF power, and 340 G magnetic field strength thruster operating conditions at both the ‘low-pressure condition’ (Low P) and ‘high-pressure condition’ (High P)..... | 54 |
| 6.15 | IEDFs recorded at the exit plane for 2 sccm argon volumetric flow rate and 340 G magnetic field strength thruster operating conditions over an RF power range of 100 W – 500 W at the ‘high-pressure condition.’ | 56 |
| 6.16 | Most probable voltages (corrected) recorded at the exit plane for 2 sccm argon volumetric flow rate and 340 G magnetic field strength thruster operating conditions over an RF power range of 100 W – 500 W at the ‘high-pressure condition.’ | 57 |
| 6.17 | IEDFs for Trials 3 (T3) and 7 (T7) recorded at the exit plane for 2 sccm argon volumetric flow rate, 214 W RF power, and 340 G magnetic field strength thruster operating condition at the ‘high-pressure condition.’ | 57 |
| 6.18 | Potentials of interest recorded at the exit plane by the emissive probe (E.P.) and the Langmuir probe (L.P.) for 2 sccm argon volumetric flow rate and 340 G magnetic field strength thruster operating conditions over an RF power range of 100 W – 500 W at the ‘high-pressure condition.’ | 57 |
| 6.19 | Electron temperatures recorded at the exit plane for 2 sccm argon volumetric flow rate and 340 G magnetic field strength thruster operating conditions over an RF power range of 100 W – 500 W at the ‘high-pressure condition.’ | 58 |

| | | |
|------|--|----|
| 6.20 | Ion number densities recorded at the exit plane for 2 sccm argon volumetric flow rate and 340 G magnetic field strength thruster operating conditions over an RF power range of 100 W – 500 W at the ‘high-pressure condition.’ | 59 |
| 6.21 | IEDFs recorded at a distance of 16 mm from the exit plane for 2 sccm argon volumetric flow rate and 340 G magnetic field strength thruster operating conditions over an RF power range of 116 W – 319 W at the ‘low-pressure condition.’ | 61 |
| 6.22 | Most Probable Voltage (corrected) recorded at a distance of 16 mm from the exit plane for 2 sccm argon volumetric flow rate and 340 G magnetic field strength thruster operating conditions over an RF power range of 116 W – 319 W at the ‘low-pressure condition.’ | 61 |
| 6.23 | Potentials of interest recorded by the emissive probe (E.P.) and the Langmuir probe (L.P.) at the exit plane for 2 sccm argon volumetric flow rate and 340 G magnetic field strength thruster operating conditions over an RF power range of 100 W – 500 W at the ‘low-pressure condition.’ | 62 |
| 6.24 | Electron temperatures recorded at the exit plane for 2 sccm argon volumetric flow rate and 340 G magnetic field strength thruster operating conditions over an RF power range of 100 W – 500 W at the ‘low-pressure condition.’ | 62 |
| 6.25 | Ion number densities recorded at the exit plane for 2 sccm argon volumetric flow rate and 340 G magnetic field strength thruster operating conditions over an RF power range of 100 W – 500 W at the ‘low-pressure condition.’ | 62 |
| 6.26 | Most probable voltage (corrected) recorded for 2 sccm argon volumetric flow rate and 340 G magnetic field strength thruster operating conditions over a range of 100 W – 300 W RF power at both the ‘low-pressure condition’ (Low P) at a distance of 16 mm from the exit plane and ‘high-pressure condition’ (High P) on the exit plane. | 64 |
| 6.27 | Electron temperatures recorded at the exit plane for 2 sccm argon volumetric flow rate and 340 G magnetic field strength thruster operating conditions over a range of 100 W – 500 W RF power at both the ‘low-pressure condition’ (Low P) and ‘high-pressure condition’ (High P) | 64 |

| | | |
|------|--|----|
| 6.28 | Ion number densities recorded at the exit plane for 2 sccm argon volumetric flow rate and 340 G magnetic field strength thruster operating conditions over a range of 100 W – 500 W RF power at both the ‘low-pressure condition’ (Low P) and ‘high-pressure condition’ (High P) | 65 |
| 6.29 | Ion saturation currents recorded at the exit plane for 2 sccm argon volumetric flow rate and 340 G magnetic field strength thruster operating conditions over a range of 100 W – 500 W RF power at both the ‘low-pressure condition’ (Low P) and ‘high-pressure condition’ (High P). | 65 |
| 6.30 | IEDF recorded at the exit plane for 2 sccm argon volumetric flow rate and 116 W RF power operating conditions over a range of 340 G – 700 G magnetic field strength at the ‘high-pressure condition.’ | 67 |
| 6.31 | Most probable voltage (corrected) recorded at the exit plane for 2 sccm argon volumetric flow rate and 116 W RF power operating conditions over a range of 340 G – 700 G magnetic field strength at the ‘high-pressure condition.’ | 67 |
| 6.32 | Potentials of interest recorded by the emissive probe (E.P.) and the Langmuir probe (L.P.) at the exit plane for 2 sccm argon volumetric flow rate and 100 W RF power operating conditions over a range of 340 G – 700 G magnetic field strength at the ‘high-pressure condition.’ | 68 |
| 6.33 | Electron temperatures recorded at the exit plane for 2 sccm argon volumetric flow rate and 116 W RF power operating conditions over a range of 340 G – 700 G magnetic field strength at the ‘high-pressure condition.’ | 68 |
| 6.34 | Ion number densities recorded at the exit plane for 2 sccm argon volumetric flow rate and 116 W RF power operating conditions over a range of 340 G – 700 G magnetic field strength at the ‘high-pressure condition.’ | 68 |
| 6.35 | IEDF recorded 56 mm downstream from the exit plane for 2 sccm argon volumetric flow rate and 116 W RF power operating conditions over a range of 340 G – 700 G magnetic field strength at the ‘low-pressure condition.’ | 70 |
| 6.36 | Most probable voltages (corrected) recorded 56 mm downstream from the exit plane for 2 sccm argon volumetric flow rate and 116 W RF power operating conditions over a range of 340 G – 700 G magnetic field strength at the ‘low-pressure condition.’ | 70 |

| | | |
|------|---|----|
| 6.37 | Potentials of interest recorded by the Langmuir probe (L.P.) and emissive probe (E.P.) at the exit plane for 2 sccm argon volumetric flow rate and 100 W RF power operating conditions over a range of 340 G – 500 G magnetic field strength at the ‘low-pressure condition.’ | 70 |
| 6.38 | Electron temperatures recorded at the exit plane for 2 sccm argon volumetric flow rate and 100 W RF power operating conditions over a range of 340 G – 500 G magnetic field strength at the ‘low-pressure condition.’ | 71 |
| 6.39 | Ion number densities recorded at the exit plane for 2 sccm argon volumetric flow rate and 100 W RF power operating conditions over a range of 340 G – 500 G magnetic field strength at the ‘low-pressure condition.’ | 71 |
| 6.40 | Most probable voltage (corrected) recorded for 2 sccm argon volumetric flow rate and 100 W RF power thruster operating conditions over a range of 340 G – 700 G magnetic field strength at both the ‘low-pressure condition’ (Low P) at a distance of 56 mm from the exit plane and the ‘high-pressure condition’ (High P) on the exit plane..... | 72 |
| 6.41 | Electron temperatures recorded at the exit plane for 2 sccm argon volumetric flow rate and 100 W RF power thruster operating conditions over a range of 340 G – 700 G magnetic field strength at both the ‘low-pressure condition’ (Low P) and the ‘high-pressure condition’ (High P). | 72 |
| 6.42 | Ion number densities recorded at the exit plane for 2 sccm argon volumetric flow rate and 100 W RF power thruster operating conditions over a range of 340 G – 700 G magnetic field strength at both the ‘low-pressure condition’ (Low P) and the ‘high-pressure condition’ (High P). | 72 |
| 6.43 | Ion saturation currents recorded at the exit plane for 2 sccm argon volumetric flow rate and 100 W RF power thruster operating conditions over a range of 340 G – 700 G magnetic field strength at both the ‘low-pressure condition’ (Low P) and the ‘high-pressure condition’ (High P). | 73 |
| 6.44 | IEDF recorded at the exit plane for 100 W RF power and 340 G source region magnetic field strength operating conditions over a range of 1.3 – 10 sccm argon volumetric flow rate (Top) and over a range of 20 – 60 sccm argon volumetric flow rate (Bottom) at the ‘low-pressure condition.’ | 75 |
| 6.45 | Most probable voltage (corrected) recorded at the exit plane for 100 W RF power and 340 G source region magnetic field strength operating conditions over a range of 1.3 – 60 sccm argon volumetric flow rate at the ‘low-pressure condition.’ | 75 |

| | | |
|------|--|----|
| 6.46 | Potentials of interest recorded by the Langmuir probe (L.P.) and the emissive probe (E.P.) at the exit plane for 100 W RF power and 340 G source region magnetic field strength operating conditions over a range of 1.3 – 60 sccm argon volumetric flow rate at the ‘low-pressure condition.’ | 76 |
| 6.47 | Electron temperatures recorded at the exit plane for 100 W RF power and 340 G source region magnetic field strength operating conditions over a range of 1.3 – 60 sccm argon volumetric flow rate at the ‘low-pressure condition.’ | 76 |
| 6.48 | Ion number densities recorded at the exit plane for 100 W RF power and 340 G source region magnetic field strength operating conditions over a range of 1.3 – 60 sccm argon volumetric flow rate at the ‘low-pressure condition.’ | 77 |
| 6.49 | Ion saturation currents recorded at the exit plane for 100 W RF power and 340 G source region magnetic field strength operating conditions over a range of 1.3 – 60 sccm argon volumetric flow rate at the ‘low-pressure condition.’ | 77 |
| 6.50 | IEDFs recorded at 2 sccm argon volumetric flow rate, 200 W RF power, and 340 G magnetic field strength thruster operating condition at the exit plane for the ‘high-pressure condition’ (High P) and 16 mm downstream of the exit plane for the ‘low-pressure condition’ (Low P)..... | 79 |
| 6.51 | IEDFs recorded at 2 sccm argon volumetric flow rate, 300 W RF power, and 340 G magnetic field strength thruster operating condition at the exit plane for the ‘high-pressure condition’ (High P) and 16 mm downstream of the exit plane for the ‘low-pressure condition’ (Low P)..... | 80 |
| 7.1 | Linear plasma potential trend lines for Langmuir probe plasma potential measurements for both the ‘Low-Pressure Condition’ and ‘High-Pressure Condition’ at 2 sccm argon volumetric flow rate, 100 W RF power, and 340 G magnetic field strength thruster operation. Linear trends calculated based on plasma potential measurements from the thruster exit plane to 216 mm downstream of the thruster exit plane..... | 92 |
| 7.2 | Ambient argon ionization around RF coaxial cable at the ‘High-Pressure Condition’ at 2 sccm argon volumetric flow rate, 100 W RF power, and 340 G magnetic field strength thruster operation. | 97 |

| | | |
|-----|--|-----|
| 7.3 | (Left) Ratio of the plume ion production rate at the ‘high- pressure condition’ divided by the ion production rate at the ‘low- pressure condition’ at 2 sccm argon volumetric flow rate and 340 G magnetic field strength thruster operation over an RF power range of 100 W – 500 W. (Right) Ratio of the ion number density at the ‘high- pressure condition’ divided by the ion number density at the ‘low-pressure condition’ at 2 sccm argon volumetric flow rate and 340 G magnetic field strength thruster operation over an RF power range of 100 W – 500 W. | 101 |
| 7.4 | Total calculated magnitude of thrust generated at $r = 0$ for 2 sccm argon volumetric flow rate and 340 G source region magnetic field strength at the ‘low-pressure condition’ and the ‘high-pressure condition’ over an RF power range of ~ 100 W – ~ 500 W. | 104 |
| 7.5 | Magnitude of thrust generated at $r = 0$ for 2 sccm argon volumetric flow rate and 100 W RF Power thruster operation at the ‘low-pressure condition’ and the ‘high-pressure condition’ over 340 G – 600 G magnetic field strength. | 109 |
| B.1 | Diagram of collision mean free paths resulting from neutral ingestion at both pressure conditions for MadHeX replica operation at 2 sccm argon volumetric flow rate, 340 G source region magnetic field strength, and 100 W RF forward power. Diagram is to scale. | 122 |

NOMENCLATURE

| | | |
|--------------------|---|--|
| <i>A</i> | = | Amps; Open Exit plane area of Thruster |
| <i>CFM</i> | = | Cubic Feet per Minute |
| <i>CCP</i> | = | Capacitively-Coupled Plasma |
| <i>cm</i> | = | Centimeters |
| <i>DAQ</i> | = | Data Acquisition Unit |
| <i>EP</i> | = | Electric Propulsion |
| E_{LOESS} | = | Error Due to Smoothing using LOESS Algorithm |
| <i>eV</i> | = | Electron Volt |
| <i>G</i> | = | Gauss |
| <i>GITs</i> | = | Gridded Ion Thrusters |
| <i>HETs</i> | = | Hall Effect Thrusters |
| <i>HPEPL</i> | = | High-Power Electric Propulsion Laboratory |
| <i>ICP</i> | = | Inductively-Coupled Plasma |
| <i>IEDF</i> | = | Ion Energy Distribution Function |
| <i>I-V</i> | = | Current – Voltage |
| I_i | = | Average Current for Voltage |
| I_{is} | = | Ion Saturation Current |
| $I_{LOESS,i}$ | = | New Current for Voltage i after smoothing |
| $I_{Sat,emit}$ | = | Ion Saturation Current Collected for Non-Emitting Case |
| $I_{Sat,non-emit}$ | = | Ion Saturation Current Collected for Emitting Case |
| <i>L/s</i> | = | Liters/second |
| <i>MadHeX</i> | = | Madison Helicon eXperiment |
| <i>m</i> | = | Meters |
| M_a | = | Mass of Atom (AMU) |
| <i>mg/s</i> | = | Milligrams per Second |
| m_i | = | Mass of Ion |
| <i>MHz</i> | = | Megahertz |
| <i>m/s</i> | = | Meters per Second |
| <i>N</i> | = | Neutral Number Density Expelled from Thruster |
| <i>n</i> | = | Loess Sweep Sample Size; Plasma Number Density |
| η_c | = | Conductance Between Thruster and Test Chamber |
| n_e | = | Electron Number Density |
| n_i | = | Ion Number Density |
| <i>RF</i> | = | Radio Frequency |
| <i>RPA</i> | = | Retarding Potential Analyzer |
| $r_p(z)$ | = | Radius of Plasma at Axial Position ‘z’ |
| <i>s</i> | = | Seconds |
| <i>sccm</i> | = | Standard Cubic Centimeters per Minute |
| <i>SWR</i> | = | Standing Wave Ratio |
| T_B | = | Thrust due to Magnetic Field Pressure |
| T_e | = | Electron Temperature |
| T_{iB} | = | Accelerated Ion Beam Temperature |

| | | |
|-------------------|---|---|
| T_N | = | Neutral Atom Temperature |
| T_s | = | Thrust due to Electron Pressure |
| T_{Total} | = | Total Thrust Produced |
| Q_{in} | = | User Defined Volumetric Flow Rate |
| $Q_{ingested}$ | = | Volumetric Flow Rate due to Neutral Ingestion |
| Q_{Total} | = | Total Volumetric Flow Rate |
| <i>UW-Madison</i> | = | University of Wisconsin-Madison |
| V | = | Volts |
| \bar{v} | = | Average Velocity |
| V_f | = | Floating Potential |
| V_{mp} | = | Most Probable Voltage |
| $V_{mp,corr}$ | = | Corrected Most Probable Voltage |
| V_p | = | Plasma Potential |
| <i>VTF</i> | = | Vacuum Test Facility |
| W | = | Watt |

SUMMARY

Helicon ion thrusters are high-efficiency, high-density plasma sources with applications in electric propulsion. Their ability to accelerate ions without the use of lifetime limiting electrodes sets them apart from traditional gridded ion thrusters (GITs) that require biased grids and neutralizing cathodes for optimal operation. The extended expected lifetime of helicon ion thrusters makes them desirable for long duration space missions and warrants continued research dedicated to their development.

In order for Helicon ion thruster performance to be properly evaluated, thruster characterization must occur during operation in a ‘space-like’ environment such as a vacuum test facility. For other electric propulsion applications such as Hall effect thrusters (HETs), operation in vacuum test facilities has been found to influence plasma properties and thruster performance characteristics. Due to the range of facility operating pressures in which Helicon ion thrusters are characterized, the presumed benefits offered by Helicon ion thrusters cannot be confirmed until the effects of neutral ingestion on their thrust contributing plasma properties are understood.

This study considers the effect of facility backpressure and subsequent neutral ingestion on the performance of Helicon ion thrusters by examining their effects on the plasma properties that influence thrust. Properties examined in this work include electron temperature (T_e), ion number density (n_i), the ion energy distribution function (IEDF), and the local plasma potential (V_p). Plasma properties are recorded during operation of a replica of the Madison Helicon eXperiment (MadHeX) at two distinct operating pressure environments. The ‘low-pressure condition’ has an operating pressure of 1.2×10^{-5} to

2.4×10^{-5} Torr corrected for argon corresponding to 0.8 sccm ingested argon volumetric flow rate. The ‘high-pressure condition’ has an operating pressure of 3.0×10^{-4} to 3.7×10^{-4} Torr corrected for argon corresponding to 3.8 sccm ingested argon volumetric flow rate. Plasma properties measured at both pressure conditions are compared to understand the physical mechanisms caused by neutral ingestion.

Differences in plasma behavior between both pressure conditions are attributed to three primary neutral-plume interactions: charge exchange collisions, momentum transfer collisions, and plume neutral ionization. Increased collision frequencies between ions and neutrals at the ‘high-pressure condition’ result in energy losses for the accelerated beam ions. In addition, downstream ionization occurs at greater rates at the ‘high-pressure condition’ due to the increased rate of electron-neutral collisions downstream of the thruster exit plane.

Examining the effect of increasing RF power on neutral ingestion mechanisms reveals that increases in most probable voltage occur at greater rates for the ‘low-pressure condition.’ In addition, electron temperatures are consistently lower and ion number densities higher at the ‘high-pressure condition’ with few noted exceptions. An examination of the effects of altering additional operating conditions on the mechanisms resulting from neutral ingestion is also conducted for magnetic field strength and volumetric flow rate. The primary effects of increasing magnetic field strength are minimal and can be attributed to increased electron confinement and reduced electron mobility. Increasing volumetric flow rate at the ‘low-pressure condition’ produces similar behavior to that observed at the ‘high-pressure condition’ such as reduced electron temperature, decreased most probable voltages, and an overall increase in ion number

density. Increases in source neutrals however, do not yield the same magnitude of plasma property change as operation at higher operating pressures implying that Helicon ion thrusters are affected by neutral ingestion predominantly in the exhaust plume.

In summary, unlike facility effects observed in the operation of HETs, neutral ingestion in the plume of the Helicon ion thruster does affect the accelerated ion beam core. Changes in plasma properties on the thruster centerline imply that neutral ingestion in the exhaust plume is pervasive and the density of the ion beam is not high enough to rely on scattering collisions at the edges of the exhaust plume to maintain the accelerated ion beam core as observed in the study of facility effects on HET operation. Helicon ion thrusters subject to neutral ingestion experience altered performance characteristics as a result of neutral-plume interactions.

CHAPTER I

INTRODUCTION

1.1 Electric Propulsion: Devices and Testing Practices

1.1.1 Electric Propulsion Devices

In order to maneuver spacecraft through the solar system or orient satellites in orbit, propulsion devices capable of delivering precise amounts of thrust are required. Electric propulsion (EP) devices achieve high exit velocities that generate thrust applicable for deep space missions or satellite station keeping applications. Unlike chemical propulsion, exhaust velocities in EP devices are not constrained by the finite energy of the chemical bonds, but on the power available and the thruster architecture.¹ This quality makes EP devices a desirable alternative to their chemical counterparts.

Any device that uses electricity to increase propellant exhaust velocity falls under the umbrella of EP. There are three overall types of EP thrusters distinguished by the method of power deposition: electrothermal, electrostatic, and electromagnetic.¹ Electrothermal devices employ propellant heating to achieve high exit velocities. Alternatively, electrostatic and electromagnetic devices use electric and magnetic fields to ionize propellant and accelerate ions to high exit velocities through a variety of ways.

Ion thrusters considered in this work are a subset of the electromagnetic family of devices. Ion thrusters use a wide range of methods to ionize and accelerate large fractions of propellant to generate thrust. Compared to other EP devices, ion thrusters boast the highest ionization efficiency (60% to >80%) and a high specific impulse range (2,000 s to

> 10,000 s).¹ Another benefit of ion thrusters is their use of monatomic gases for propellant making their fuel easy to store and transport. These qualities make ion thrusters appealing for onboard applications and provide motivation for continuing research dedicated to their development.

Ion thruster operation is divided into two primary stages as discussed in Sec. 2.1.1: an ionization stage and an acceleration stage. The ionization stage occurs in the source region where propellant is ionized via energy deposition. The acceleration stage generates thrust through momentum transfer with accelerated ions. These two stages operate independently simplifying device design and operation. The uncoupled nature of the ion thruster means that optimization of either region yields an overall boost in performance for the entire thruster design.²

A particular ion thruster architecture of interest is the helicon ion thruster. The high ionization efficiency, high specific impulse, and ease of design of an ion thruster coupled with the lack of electrodes and neutralizing cathode required for thrust generation of the helicon ion thruster make Helicons appealing for application as EP devices. Helicon ion thruster performance is evaluated either directly or by measuring the electron temperature, ion energy distribution function (IEDF), ion density, and plasma potential during operation in a vacuum environment to predict performance values such as specific impulse, thrust, and efficiency. These plasma properties are also used to determine the radio frequency (RF) coupling mode and active ion acceleration mechanism at work for a given operating condition, both of which influence thrust generation. The active RF coupling mode and ion acceleration mechanism are considered performance metrics in

this work. Testing occurs in a vacuum test facility that produces a ‘space-like’ environment by lowering the pressure of the device’s exhaust environment.

1.1.2 Vacuum Test Facilities

In order to assess the viability of EP devices for operation on satellites and spacecraft, extensive characterization of device performance is conducted on the ground. In order to quantify performance values of EP thrusters, measurement of plasma properties and performance values occurs during operation in a vacuum test facility. These facilities lower the pressure inside a test vessel in an effort to reproduce the high-vacuum condition of outer space. The exhaust of the thruster is expelled into the test vessel and measurements are recorded. These values represent the best estimates of thruster performance available until an in-space test can be conducted. Onboard satellite tests have a great amount of risk and cost associated with evaluating an unproven propulsive device making ground testing a logical first step in thruster development.

Vacuum test facilities, however, differ in size, pumping speed, and operating pressure (the recorded pressure inside the test vessel while the thruster is operating and propellant is exhausted from the device). For Hall effect thrusters (HETs), differences in facility environment have been found to influence plasma behavior and thruster performance leading to discrepancies between predicted performance and actual performance during space flight.³ Neutral ingestion is an example of a facility effect caused by the finite pumping speed inside a vacuum test facility. Neutral ingestion is the recirculation of previously expelled neutral propellant into the exhaust plume and ionization region of an EP device. HETs subject to neutral ingestion during operation inside a vacuum test facility have multiple opportunities to ionize previously expelled neutral propellant

leading to an increase in recorded thrust values as compared to HETs free of neutral ingestion.⁴ Similar performance inflation is hypothesized for Helicon ion thrusters subjected to neutral ingestion, but the effects are undocumented.²²

Ion sources operating in ground based test facilities generate a back pressure of neutral propellant due to the finite pumping speeds of the research environment. Penetration of neutrals into the ion beam plasma and the subsequent interactions that occur modify plasma potential, plasma density, electron temperature, and ion energies, which influence performance parameters.⁵ Alterations in these plasma properties are indicative of changes in plume momentum that has led to performance inflation in other EP devices. Due to the wide range of facility environments available, facility effects must be documented across multiple testing environments in order to better compare performance data of EP devices.³ Understanding the influence of facility effects on Helicon ion thruster performance is the motivation for this work.

CHAPTER II

HELICON ION THRUSTERS

2.1 Helicon Ion Thruster Operation

One of the common types of ion thruster is the RF ion thruster, which uses radio waves to ionize propellant. The two types of RF ion thrusters considered in this work are the gridded ion thruster (GIT) and the Helicon ion thruster, differentiated by the methods of ion acceleration employed. Note, there are other methods of ion acceleration for GITs than are detailed in Sec. 2.1.2, but they will not be considered in this study.

2.1.1 Thruster Design

In classical GITs, there are three main stages to thruster operation as depicted in Fig. 2.1.¹ The first stage consists of the generation of positively-charged ions from the excitation of a noble gas propellant. Following ionization, electrons travel upstream to be collected by a positively-biased anode while the ions travel downstream towards the thruster exit due to their attraction to the electric field generated by the acceleration grid assembly. The grid assembly consists of two optically-aligned, electrically conductive grids. The first grid, called the screen grid, is biased below the anode potential and ensures that the positive ions are aligned along the axial direction of the device in order to maximize thrust upon their exit. The negatively-biased acceleration grid completes the circuit generating a favorable electric field which attracts and accelerates the ions in stage

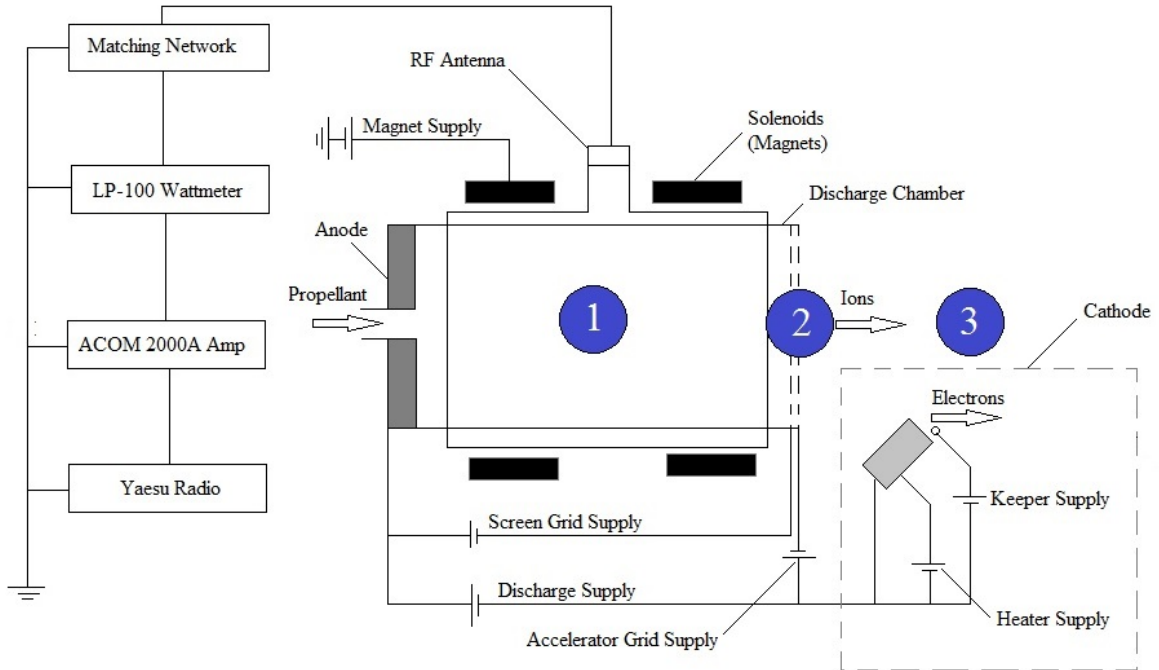


Figure 2.1: Electrical diagram of a gridded ion thruster. Stage 1: Ionization. Stage 2. Ion Acceleration. Stage 3: Plume neutralization.

two. Stage three consists of expelling electrons from a neutralizer cathode at the thruster exit in an effort to achieve charge neutrality in the exhaust plume.

In Helicon ion thrusters, only two operating stages are required to generate thrust as depicted in Fig. 2.2. In the first stage, a monatomic propellant is ionized through the use of RF wave excitation. An antenna broadcasts RF waves into the source region of the thruster at a designated frequency (13.56 MHz for this work) depositing RF power leading to propellant ionization in the presence of an axial magnetic field on the order of a few hundred Gauss (G). In the second stage, ions are accelerated across a potential drop at the thruster exit generating thrust. The ions exit the thruster in a quasi-neutral plume without the use of a cathode to achieve charge neutrality. Quasi-neutral plumes are distinguished as having a Debye length (as defined in Eq. 2.1) much smaller than the

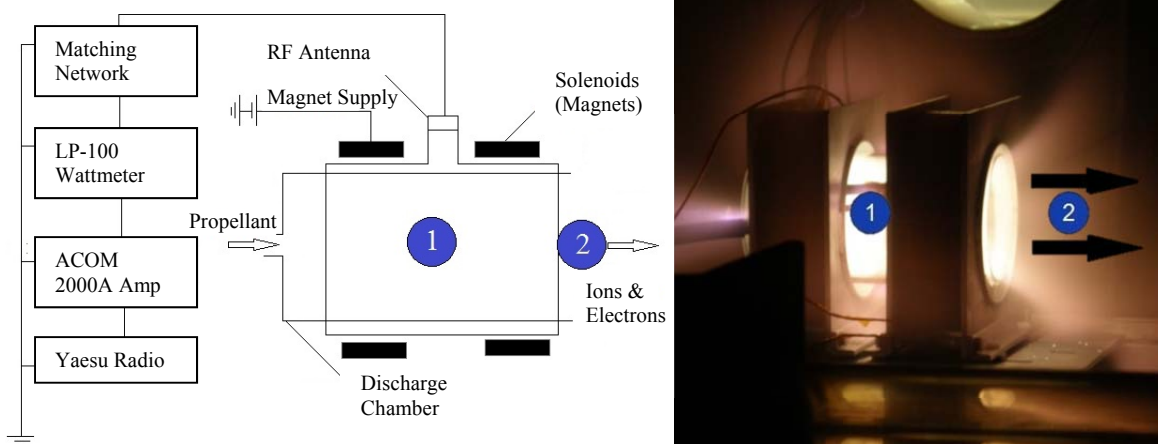


Figure 2.2: Electrical diagram of a Helicon ion thruster tested at Georgia Tech (Left). Image of Helicon ion thruster with thruster stages labeled (Right). Stage 1: Ionization. Stage 2: Acceleration

characteristic length of the system. Quasi-neutrality shields the bulk plasma from local charge concentrations and external potentials at short distances.⁶

In Eq. 2.1, T_e represents the electron temperature in electron volts (eV), n is the plasma number density, and m_i is the mass of the ion. In quasi-neutral plasmas, the plasma density can be assumed to be approximately equal to the ion number density (n_i) which can be assumed to equal the electron number density (n_e) as shown in Eq. 2.2.

$$\lambda_D = 7430 \left(\frac{T_e}{n} \right)^{1/2} m_i \quad (\text{Eq. 2.1})$$

$$n_i \cong n_e \cong n \quad (\text{Eq. 2.2})$$

In order to optimize Helicon ion thruster operation (propellant flow rate, RF power, magnetic field strength etc.), the method of ion acceleration must be understood. Several highly-debated acceleration mechanisms have been theorized; viability of a particular



Figure 2.3: MadHeX thruster operating on argon while immersed in a vacuum environment at Georgia Institute of Technology.

mechanism hinges on proper characterization of the plasma plume.⁷ The acceleration mechanism considered in this work is the Double Layer theory detailed in Sec. 2.2.2.

2.1.2 Thrust Calculation

When comparing the viability of the Helicon ion thruster as a replacement for the GIT, an evaluation of the thrust generating capabilities of the Helicon ion thruster must be conducted. Helicon ion thrusters are theorized to generate thrust without the use of biased acceleration grids due to a potential differential that forms near the thruster exit naturally. Ions are accelerated across the potential difference similar to the way ions are accelerated between the biased grids of the GIT. Thrust of the Helicon ion thruster is generated by a transfer of momentum between the accelerated ions and the thruster due to interaction between the exiting ions and the magnetic field. Thrust can be measured directly, but direct thrust measurements are not common in the characterization of Helicon ion thrusters. Since direct thrust measurements require the entire thruster to be immersed in a vacuum environment as shown in Fig. 2.3, and a significant portion of published Helicon ion thruster data is measured while the thruster characterized is

mounted externally to the vacuum chamber and exhausted into a vacuum environment, plasma properties are often used in place of direct thrust measurement to calculate thrust.⁷⁻¹²

The Helicon ion thruster considered in this work has a magnetic nozzle (detailed in Section 5.1.1). Due to the plasma expansion through the magnetic nozzle, thrust (in Newtons) for the MadHeX replica has two main contributions: thrust due to electron pressure (T_S) and thrust due to magnetic field pressure (T_B) as shown in Eq. 2.3.¹³⁻¹⁴

$$T_{Total} = T_S + T_B \quad (\text{Eq. 2.3})$$

Equation 2.3 can be broken down into the plasma properties of interest as shown in equations 2.4 and 2.5. A complete derivation for Eq. 2.4 can be found in Appendix A. Equation 2.4 is a quasi-one dimensional model of the total thrust produced at a given axial condition integrated across the radius of the plasma ($r_p(z)$) by a Helicon ion thruster with a magnetic nozzle.^{1,13-14} Total thrust is a function of the ion number density, accelerated ion beam temperature (T_{iB}), electron temperature, neutral number density expelled from the thruster (N), and neutral atom temperature (T_N). Temperatures (in eV) appear in the thrust equation due to their relationship with velocity. Since the velocity of the ions is a function of the difference in the potential of where the ions formed and the potential at the ions' current location, accelerated ion beam temperature can be expressed as the difference between the most probable voltage (V_{MP}) of the ion energy distribution function (IEDF) and the local plasma potential (V_p). This value is known as the corrected most probable voltage ($V_{MP,corr}$).

$$T_{Total} \equiv 1 \times 10^{-18} \int_0^{r_p(z)} [n_i(T_{iB} + T_e) + NT_N] r dr \quad (\text{Eq. 2.4})$$

$$T_{iB} = V_{MP,corr} = V_{MP} - V_p \quad (\text{Eq. 2.5})$$

This study focuses on the thrust contributions from the ions and electrons only. The four variables of interest in this study are ion number density, most probable voltage of the IEDF, electron temperature, and plasma potential.

2.1.3 Benefits

Ion acceleration without acceleration grids or neutralizing cathodes are the primary advantages of Helicon ion thrusters. Acceleration grids are costly, lifetime limiting components required for thrust generation in a GIT. The ion plume outside the spacecraft created by the acceleration grids requires a cathode to provide electrons enabling recombination of the propellant in an effort to achieve charge neutrality outside the thruster exit plane. Like the acceleration grids, cathodes are also lifetime-limiting components that also require dedicated structure and high-purity propellant sources for operation; features that can significantly increase the cost of the spacecraft.² Longer lifetimes, lower cost, and a reduction in launch weight make Helicon ion thrusters an attractive option for deep space missions.¹⁵ This expected increase in thruster lifetime is the motivation for continued research into Helicon ion thruster development.

2.2 Helicon Ion Thruster Performance

Performance of a Helicon ion thruster is governed by both thruster operating parameters and physics-driven, source region behavior. The Helicon ion thruster has operating conditions including propellant flow rate, RF power, and source region magnetic field strength that affect performance directly. Indirectly, thruster operating parameters cause changes in the physics driven behavior of the generated plasma that can also affect thruster performance.

Previously identified plasma properties of interest for thrust generation include ion number density and the most probable voltage of the thruster ion beam. These values can be modified due to changes in the thruster operating parameters but are subject to greater changes by physics-driven plasma behavior. Ion number density and most probable voltage are altered by the RF coupling mode and ion acceleration mechanism respectively, both of which are physics driven behavior that cannot be controlled directly. Due to the correlation with thrust generation, the RF coupling mode and acceleration mechanism are considered performance metrics in this study. The RF coupling mode and acceleration mechanism of the Helicon ion thruster are discussed in Sections 2.2.1 and 2.2.2, respectively.

2.2.1 Radio Frequency Coupling Modes

Ion number density in an RF Helicon ion thruster is controlled by the RF coupling mode induced in the source region of the thruster during operation. RF coupling modes are distinguished by the physics-driven behavior of the particles in the source region resulting in ionization. There are three main RF coupling modes possible in an RF ion

thruster: capacitive mode, inductive mode, and Helicon mode. The Helicon RF coupling mode generates the highest ion density and, thus, the greatest possible thrust for a given acceleration potential drop. This correlation makes achieving the Helicon RF coupling mode desirable in order to optimize performance of a given Helicon ion thruster.

In order to understand how ionization of the propellant occurs in the source region, familiarity with the RF coupling modes is required. Each RF coupling mode is distinguished by the magnitude of the ion number density and the density profile at the thruster exit as well as the physics causing ionization as described in Table 2.1. A mode change is marked by a discontinuous increase in ion density or a change in the ion number density profile at the thruster exit plane.

Capacitively-coupled plasmas (CCPs) have the lowest overall ion number density with the radial density profile characterized by an annular or ‘M’ shape at the thruster exit with a ring of maximum density located between the thruster centerline and the edge of the discharge chamber. Each thruster will have a different power requirement to achieve each coupling mode, but within the operating power range of that thruster, a CCP will occur at the lowest powers available that result in an ionized propellant. Ionization occurs when RF waves propagate through the entire volume of propellant in the source region. The majority of energy deposited into a CCP works towards ion acceleration instead of ionization, but CCPs have fluctuating ion densities that make steady state operation difficult.¹⁶ When the ion density changes in a CCP, the resistance of the plasma inside the thruster also changes altering the load connected to the RF system. Plasma load changes require active management by the thruster operator or an automatic matching network. The matching network must change its inductance and capacitance or else risk

hardware damage due to reflected power, *i.e.* power which is unable to be deposited into the plasma and travels back to the RF power source. Changes in ion density for a CCP can be too fast for an operator or the equipment to accommodate making CCPs difficult to maintain.

Inductively-coupled plasmas (ICPs) are observed at the first discontinuous increase in plasma density with increasing RF power, although hysteresis behavior among the modes is possible. ICPs have higher densities than CCPs and have a density profile that plateaus across the thruster exit diameter, a density profile commonly desired for gridded operation. In ICPs, RF waves only penetrate the skin depth of the plasma volume marking a change in ionization physics from the capacitive mode.¹⁶

Table 2.1: Ionization physics explanations and ion density profile information for the capacitive, inductive and Helicon RF coupling modes.

| RF Coupling Mode: | Capacitive | Inductive | Helicon |
|-----------------------------|--|---|---|
| Ionization Physics: | RF waves propagate through entire volume of propellant | RF waves penetrate skin depth of plasma volume. | RF waves induce bounded whistler waves in plasma volume |
| Ion Density Profile: | Annular or ‘M’ shaped ion density profile | Plateau shaped ion density profile | Parabolic ion density profile |

The last discontinuous increase in density magnitude occurs at the transition from an ICP to Helicon mode. The Helicon mode supports the highest plasma density on centerline and is characterized by a peaked density profile at the thruster exit. In Helicon mode, RF waves induce Helicon waves or bounded whistler waves that result in high density, uniform plasma generation. Their high ionization density results in a greater percentage of the propellant achieving an accelerated exhaust velocity contributing to

thrust generation. Helicon mode occurs in the high power range of the operational power limits a given thruster and is often characterized by a blue core observed inside the discharge chamber.¹⁶ It is in this final mode that a Helicon ion thruster is intended to operate due to the availability of large ion densities compared to the ion densities available during operation in the other RF coupling modes for a given thruster architecture.

In this study, identification of the Helicon RF coupling mode involves two separate criteria. First, a blue core in the plasma source region must be observed. Second, two distinct, discontinuous increases of the order of magnitude of the ion number density must also occur.

2.2.2 Acceleration Mechanism: Double Layer Theory

Ion velocity in a Helicon ion thruster is directly related to specie temperature as illustrated in Eq. 2.4 and explained in Appendix A. The velocity that ions have at any given axial location along the Helicon ion thruster axis can be expressed as the difference between the most probable voltage (plasma potential at the location where ions are formed) and the local plasma potential. The maximum possible velocity gain is the total potential drop that occurs along the thruster axis. In Fig. 2.4, the most probable voltage of the ions is 60 V. The ions would have a final velocity corresponding to the 40 V potential decrease at the 130 mm location. The 40 V difference represents the corrected most probable voltage at the 130 mm location.

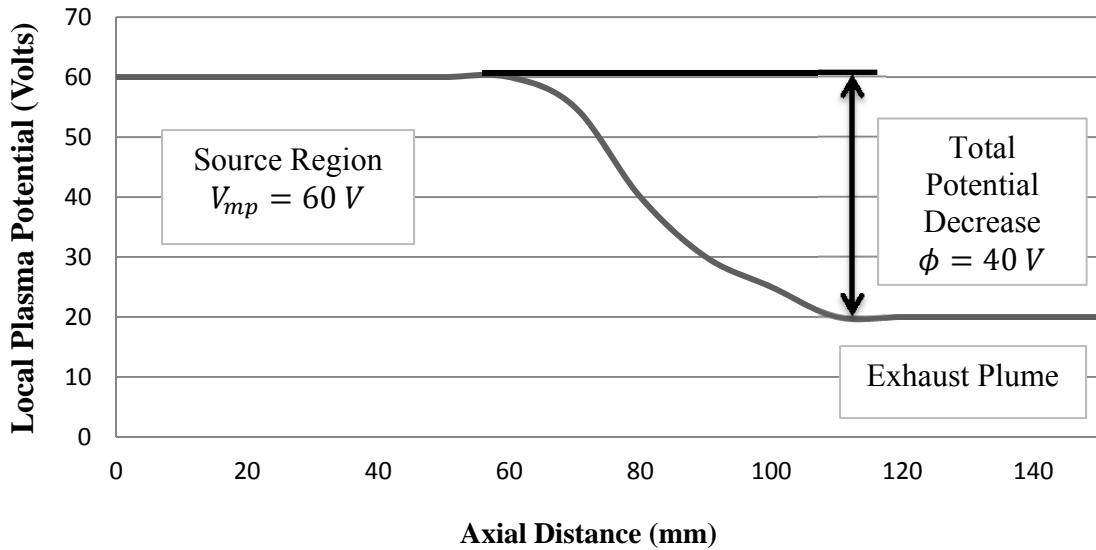


Figure 2.4: Sample potential drop (ϕ) located at the boundary of the source region and exhaust plume.

The potential drop depicted in Fig. 2.4 is the acceleration mechanism for ions in the Helicon ion thruster. There are many theories for how the potential drop is formed. A particular theory of ion acceleration that has garnered significant attention, and has been observed during previous operation of the thruster considered in this work, is the Double Layer theory. A Double Layer is characterized as an electric field occurring downstream of a low-pressure, high-ion number density, magnetized plasma source resulting in ion acceleration.¹⁷ The electric field itself is a drop in plasma potential occurring over a distance on the order of a few Debye lengths. Ions formed upstream of the Double Layer are accelerated down the potential hill at the thruster exit, generating thrust.

Formation of a Double Layer can be identified in the following ways. The presence of an accelerated ion beam is the strongest indication of a Double Layer in an expanding plasma device.¹⁸⁻¹⁹ An accelerated ion beam would be recognized as a double-peaked IEDF where the first peak represents the local ion population energy and the second,

higher energy peak corresponds to the accelerated ion beam. Axially mapping the IEDF using a Retarding Potential Analyzer (RPA) downstream of the thruster exit is the optimal way to determine if a Double Layer is present.¹⁷ IEDF measurements are discussed in greater detail in Sec. 5.3.2.

Observable plasma characteristics resulting from Double Layer formation include a large increase in plasma density in the source region coinciding with a slight decrease in downstream plasma density.¹⁷ This increase in density is thought to occur when the Larmor radius of the ions becomes smaller than the inner discharge chamber radius of the thruster, reducing the radial loss of ions to the chamber walls. Such a transition would be instigated by changing the operating conditions of the Helicon ion thruster such as increasing the magnetic field strength in the source region, increasing confinement. The resulting reduction in ion losses causes a discontinuous density increase that enables the magnitude of the potential gradient at the thruster exit to increase forming a Double Layer.¹⁷ The maximum energy of the accelerated ion beam directly relates to the plasma potential of the source region.

In order to identify a Double Layer, several methods are considered. Measurement of the plasma density in this work uses electrostatic probes and due to the confined space of the discharge chamber, it becomes difficult to maintain the electrostatic probe orientation required for proper plasma measurements in a magnetized, RF plasma source. Since electrostatic probes are unavailable for identification of a Double Layer in this work, an RPA will be used at the thruster exit to determine if a Double Layer forms as indicated by a double-peaked IEDF. However, as double-peaked IEDFs can also indicate oscillating

RF sheaths, multiple IEDF sweeps at a given operating condition and axial location will be required to confirm Double Layer formation.²⁰

The Double Layer is only one of many theorized ion acceleration mechanisms observed during operation of Helicon ion thrusters. Across different vacuum testing facilities, multiple types of plasma potential drops have been observed leading to discordant theories explaining how ion acceleration is achieved across each different type of potential profile. Some profiles however, cannot be reproduced leading to much conjecture on their validity and applicability for in space thruster operation.¹⁶ Double Layer theory is a highly contested acceleration mechanism and is chosen as a point of interest in this study due to its appearance during previous runs of the Madison Helicon eXperiment at the University of Wisconsin-Madison test facility.^{7, 21-22}

CHAPTER III

FACILITY EFFECTS

3.1 Helicon Ion Thruster Facility Effects

EP devices are typically characterized in ground-based vacuum test environments in an effort to predict thruster performance in space. Measurements of plasma properties and performance values of these devices recorded during operation in a vacuum test facility differ from the performance observed in orbit or in deep space.^{4,8} Unlike during operation in space, where expelled propellant will not travel back towards the thruster exit plane, EP devices operating in vacuum test facilities are subject to neutral ingestion. During neutral ingestion, previously expelled neutral propellant travels back towards the thruster exit plane where neutral atoms may ionize and accelerate across local potential differentials. This behavior has resulted in inflated thrust values for HETs.⁴ The magnitude of neutral ingestion, and the acceleration of newly ionized propellant due to neutral ingestion, depends on facility operating pressure and the available thruster exit area open to neutral particle ingestion. The open discharge chamber exit plane of the Helicon ion thruster makes them highly susceptible to neutral ingestion.

3.1.1 Facility Effect Susceptibility

Helicon ion thrusters have been tested across a wide breadth of vacuum facility environments ranging from small expansion chambers connected to the thruster exit plane to chambers in which the thruster is immersed in a vacuum environment.^{7-9,11-12,21-22}

The range of facility environments used to characterize Helicons has led to the observation of multiple ion acceleration mechanisms as discussed in Sec. 2.2.2. In order to advance the understanding of Helicon ion thruster technology, a better understanding of the ion acceleration mechanisms is required. Given the effect neutral ingestion has on HET performance, Helicon ion thruster performance for space applications cannot be accurately predicted until the effect of neutral ingestion is understood.

Goebel and Katz remark that the differences in plume characterization observed between vacuum facility operation and real space application is due to background gas pressure.¹ The supposition that Helicon ion thrusters are subject to facility effects is illustrated in an example by Charles.²³ Charles calculates that for a pumping speed of 300 /s in a vessel volume of 30 l, the residence time of an argon atom would be approximately 100 ms. Assuming a neutral velocity of 300 m/s gives the particle 30 m of travel before being removed by the vacuum pumps. This calculation assumes free molecular flow where the neutral atoms will travel without colliding with the solid walls of the vacuum vessel and their mean free path exceeds the characteristic length of the vacuum chamber allowing them to recirculate.²⁴ Without the acceleration grids present in GITs, an atom is free to return to the ionization region of the Helicon by traveling back through the exit plane unimpeded. Due to the long residence times of neutral propellant in a vacuum vessel, an argon atom is free to re-enter the source region and exhaust plume of a Helicon ion thruster multiple times. Neutral ingestion allows for multiple ionization opportunities of neutral propellant while also raising the neutral pressure inside the discharge chamber of the Helicon ion thruster. This pressure rise is an artificial product of finite pumping capabilities of vacuum test facilities that would not appear during

operation of a Helicon ion thruster in space where neutral propellant is unlikely to travel upstream in the exhaust plume.

Helicon ion thrusters must contend with performance modification caused by neutral ingestion due to the open area of the thruster exit plane. Neutral ingestion may effect RF coupling mode and active ion acceleration mechanisms in addition to general plasma properties due to the effect of increased neutral particle collisions. Understanding the effect on performance of neutral ingestion as it relates to thrust production is critical in order to determine the Helicon's potential as a GIT alternative.

3.1.2 Anticipated Results of Facility Effects

The anticipated effect of neutral atom recirculation described by Charles on Helicon ion thruster plasma properties is performance inflation.²³ The artificial pressure rise due to neutral ingestion mimics some aspects of operation at a higher volumetric flow rate than the flow rate provided to the thruster. The total volumetric flow rate is the summation of the provided flow rate and the ingested flow rate as shown in Eqn. 3.1 in Sec. 3.1.3. Plasma densities and RF coupling mode transitions are affected by neutral ingestion. Thruster operating conditions based on performance in ground-based test facilities subject to neutral ingestion will not represent operating conditions required for equal performance in a space-like environment. Changes in thruster behavior may also alter the operating conditions necessary to change RF coupling modes or cause a particular ion acceleration mechanism to form.

In addition to inflating the overall volumetric flow rate, background pressure of the vacuum vessel will change the residence times of neutral propellant inside the discharge chamber. Across any pressure gradient, molecules will travel to areas of lower pressure.

Inside the discharge chamber, a pressure gradient exists between the propellant inlet (higher pressure) and the thruster exit (facility operating pressure). At lower exit plane pressures, propellant will leave the discharge chamber sooner resulting in shorter residence times in the source region. Shorter residence times decrease the interaction time between the neutral propellant and the magnetic flux from the RF antenna that results in ionization. Shorter residence times require higher flow rates or higher RF power levels in order to initiate plasma formation in the source region. Pressure gradients of lower magnitude along the thruster centerline occurring in facilities with higher operating pressure will maintain plasma at lower flow rates than those possible in facilities with larger pressure gradients. The end results of this behavior are greater propellant and power demands when operating in space than predicted during ground testing.

The influence of operating pressure and neutral ingestion in particular on Helicon ion thruster performance is unclear. While it can be inferred that performance would improve due to artificially inflated propellant flow rates and lower required RF power, the magnitude of performance enhancement has not been quantified. In addition, ambient gases present at higher operating pressures external to the thruster may absorb RF power from the antenna instead of the intended propellant in the thruster source region lowering the overall power available for ion acceleration. In order for Helicon ion thrusters to become a more viable option for onboard applications, an accurate assessment of the influence of facility effects, particularly neutral ingestion, on device performance characteristics is required.

3.2 Neutral Ingestion

In order to determine the potential effect of neutral ingestion on Helicon ion thrusters, the quantity of propellant ingested must be estimated. The flow rate ingested can then be added to the provided thruster flow rate to estimate the artificial operating flow rate that influences thruster performance. Performance differences between the thruster defined flow rate and the total flow rate including neutral ingestion is of interest in this study.

3.2.1 Predicted Ingestion Calculations

Total volumetric flow rate in sccm for an EP device (Q_{Total}) is the sum of the thruster defined volumetric flow rate (Q_{in}) and the volumetric flow rate due to neutral ingestion ($Q_{ingested}$) as shown in Eq. 3.1.¹

$$Q_{Total} = Q_{in} + Q_{ingested} \quad (\text{Eq. 3.1})$$

where

$$Q_{ingested} = (7.82 \times 10^8) \frac{P A \eta_c}{\sqrt{T_N M_a}} \quad (\text{Eq. 3.2})$$

The ingested volumetric flow rate is a function of the background pressure in Torr (P), open area in m^2 subject to neutral ingestion (A), conductance between the thruster discharge chamber and vacuum test facility (η_c), temperature in kelvin of the back-flowing neutral propellant (T_N), and the gas mass in AMU of the back-flowing neutral propellant (M_a). Since the exit plane area of the Helicon ion thruster is open to the vacuum chamber, the entire exit area ($0.0079 m^2$) is considered subject to neutral ingestion with a conductance of 1. Ambient chamber temperature (294 K) is assumed for the back-flowing neutral argon propellant (39.948 AMU) as an ambient temperature would yield the highest ingested flow rate. Eq. 3-2 becomes a function of backpressure

only reducing to Eq. 3.3 when considering the MadHeX Replica running on argon. Calculated ingestion volumetric flow rates in sccm for three common magnitudes of facility backpressure, assuming the entirety of the background gas is argon, are shown in Table 3.1.

$$Q_{ingested} = (5.699 \times 10^4)P \quad (\text{Eq. 3.3})$$

Table 3.1: Calculated neutral ingestion volumetric flow rates for the MadHeX Replica in an argon environment.

| <u>Facility Operating Pressure (Argon)</u> | <u>Calculated Neutral Ingestion Flow rate</u> |
|--|---|
| 10^{-3} Torr | Maximum of 57 sccm |
| 10^{-4} Torr | Maximum of 6 sccm |
| 10^{-5} Torr | Maximum of 1 sccm |

Some facility background pressures can result in ingestion rates on the same order of magnitude as the propellant ingestion rate of the thruster. For some Helicon ion thrusters including the MadHeX replica considered in this study, 1 sccm of ingested neutral propellant is on the same order of magnitude as the provided thruster flow rate of 2 sccm. Guidelines regarding acceptable ingestion flow rates or minimum operating pressures required for data collection have not yet been established for Helicon ion thrusters but have been investigated for other EP devices such as HETs.

In the examination of the effect of neutral ingestion on HET performance, Randolph *et al.* suggests that vacuum chamber operating pressure can be no greater than 5×10^{-5} Torr for reliable performance evaluation.²⁵ Randolph's limit is based on reducing the

amount of previously expelled neutral propellant entrained by the thruster and has been experimentally verified for ion thrusters. Due to the characteristically low flow rates required for Helicon ion thrusters (on the order of 1-10 sccm) compared to HETs (on the order of 100 sccm) and knowing that neutral ingestion affects HET performance, it is concluded that neutral ingestion will affect the performance of Helicon ion thrusters. Although the ingested flow rate will not be below Randolph's ingested mass flow rate limit of 3% of the provided thruster flow rate, Randolph's additional criteria for the pressure limitation including free molecular flow of neutral particles in a vacuum chamber for an EP device operating at ≤ 1 kW of power and having an unimpeded exit plane provides the foundation for choosing the operating environments used in this study to examine the effects of neutral ingestion on Helicon ion thrusters. Background pressures of interest in this study are discussed in Sec. 4.1. An examination of neutral ingestion effects on Helicon ion thruster plasma properties will be examined in this work. Determination of maximum operating pressure requirements for proper device performance evaluation is outside the scope of this work.

CHAPTER IV

RESEARCH QUESTIONS

4.1 Operating Pressure Conditions

One way to assess the influence of neutral ingestion on Helicon ion thruster performance, is to characterize the plasma properties near the thruster exit plane at different operating pressures. Changes in plasma properties and behavior can be used to determine the physical mechanisms caused by neutral ingestion near the thruster exit. In order to choose the proper starting foundation for pressure environments of interest, facility effect literature of other EP devices is consulted.^{4-5,25} Due to the depth of results available, the groundwork for this study stems from the facility effect literature on HETs.

Evaluation of Helicon ion thruster performance is conducted for two distinct operating pressure environments based on Randolph's limit discussed in Sec. 3.2.1. The first environment considered is below Randolph's suggested limit with an operating pressure between 1.2×10^{-5} to 2.4×10^{-5} Torr. The other operating pressure considered is above Randolph's limit between 3.0×10^{-4} to 3.7×10^{-4} Torr. These environments are referred to as the 'low-pressure condition' and the 'high-pressure condition,' respectively and are further detailed in Sec. 5.1.

4.2 Neutral Ingestion Effects on Plasma Properties

The first portion of this investigation is to consider the effect of neutral ingestion resulting from increased facility background pressure on individual plasma plume

properties. Properties to be considered in this work include plasma potential, most probable voltage of the IEDF, electron temperature, and ion number density due to the relationship between these properties and thrust generation as illustrated by Eq. 2.3-2.5 and discussed in Section 2.1.2. These plasma properties are also of interest as indicators of how energy is exchanged in the propellant volume studied. Analysis of energy transfer in the propellant volume will help identify the physical mechanisms resulting from neutral ingestion.

To measure the effect of neutral ingestion on plasma properties, each property is compared directly between pressure conditions. Measurements are conducted along the thruster centerline as shown in Fig. 5.2 from the exit plane up to 216 mm downstream (and in some cases for the RPA, up to 79 mm upstream of the exit plane inside the discharge chamber) for both the ‘high-pressure condition’ and the ‘low-pressure condition.’ Values and trends for each plasma property are compared for thruster operation at ~100 W RF power, 2 sccm argon volumetric flow rate (0.059 mg/s argon), and 340 G source region magnetic field strength.

Contributions from this analysis include an examination of the mechanisms at work leading to changes in plasma properties due to neutral ingestion, as well as quantitative comparisons of property behaviors from both pressure conditions. Values of interest include mean free path, collision frequency, and thrust augmentation. Direct comparisons of plasma properties are also conducted for electron temperature, most probable voltage, ion number density, and the IEDF.

4.3 Neutral Ingestion Effects on Operating Parameters

The next portion of this study examines plasma property behavior at both pressure conditions over a range of thruster operating conditions. After identifying the physical mechanisms that cause changes in plasma properties due to neutral ingestion, the magnitudes of those changes at different RF power levels and magnetic field strengths are compared. This analysis provides insight into the way thruster operation affects the scale of performance change due to neutral ingestion.

To complete this portion of the study, a volumetric flow rate of 2 sccm argon is maintained while RF power is raised from ~100 W to 500 W (up to 700 W for some cases) for a magnetic field strength of 340 G in the source region. Plasma potential, the most probable voltage of the IEDF, electron temperature, and ion number density are recorded approximately every 100 W. A separate analysis is then conducted while maintaining a volumetric flow rate of 2 sccm argon and ~100 W RF power while increasing the magnetic field strength from 340 G to 500 G (up to 700 G for some cases) while measuring the same aforementioned plasma properties. Behaviors of interest for this analysis include variations in the values and changes in the property trends of the most probable voltage, plasma potential, electron temperature, and ion saturation current over changing RF power or magnetic field strength. All these behaviors are compared between both pressure conditions with the objective of quantifying the effect of neutral ingestion at different operating conditions.

This portion of the study endeavors to quantify how different thruster operating conditions influence the effects of neutral ingestion. A direct comparison between values of plasma potential, most probable voltage, electron temperature, and ion number density

at corresponding operating conditions is conducted to track how energy is exchanged by the propellant. This portion of the study provides a benchmark for performance changes anticipated during operation in different pressure environments and the effects of thruster operating conditions on the mechanisms driving the performance changes caused by neutral ingestion.

4.4 Neutral Ingestion at the ‘High-Pressure Condition’ versus Increased Volumetric Flow Rate at the ‘Low-Pressure Condition’

Following an examination of the relationships between plasma properties and thruster operating parameters at each pressure condition, a comparison study is conducted between thruster operation at the ‘high-pressure condition’ at a volumetric flow rate of 2 sccm argon, 100 W RF power, and 340 G source region magnetic field strength with volumetric flow rates ranging from 1.3-60 sccm argon, 100 W RF power, and 340 G magnetic field strength at the ‘low-pressure condition.’ This examination will determine whether neutral ingestion effects are comparable to increases in propellant volumetric flow rate and whether performance changes can be ameliorated at lower pressures by inflating the provided thruster operating volumetric flow rate.

Plasma potential, most probable voltage of the IEDF, electron temperature, ion number density, and the IEDFs are analyzed for variations in the values and changes in the property trends at each flow rate when compared to the ‘high-pressure condition’ case. The goal of this study is to compare the changes in plasma properties caused by an increase in neutral flow into the thruster and the changes caused by an increase in neutral ingestion due to background pressure.

4.5 Neutral Ingestion Effects on RF Coupling Mode and Double Layer Formation

The final area of interest in this study is an examination of the availability of the Double Layer acceleration mechanism and the Helicon RF coupling mode for thruster operation. Availability of these physics-based operating conditions is necessary in order to produce and accelerate the greatest possible amount of ions to generate thrust.

IEDFs from all operating conditions at both pressure conditions are examined for the presence of a Double Layer characterized by a persistent, double-peaked IEDF indicating an accelerated ion population. Densities and ion saturation currents for increasing RF power and increasing magnetic field strength are examined for any discontinuous increases in ion number density indicating an RF coupling mode transition. Two separate, discontinuous increases indicate a transition from the capacitive mode to the inductive mode and then from the inductive mode to the Helicon mode.

The aim of this study is a feasibility assessment of physics-based operating conditions for low-pressure Helicon ion thruster operation. An understanding of the environmental conditions required to induce particular performance conditions of interest will aid researchers in understanding thrust generation in Helicon ion thrusters.

CHAPTER V

EXPERIMENTAL SET-UP

5.1 Helicon Ion Thruster

In order to ensure that certain performance metrics of interest are possible, a thruster geometry was selected with a history of producing the Double Layer acceleration mechanism and Helicon RF coupling mode. A replica of the Madison Helicon eXperiment (MadHeX) is used in this study for the explicit reason that both performance metrics of interest have been observed during thruster operation.^{7,21-22}

5.1.1 MadHeX Replica

The MadHeX is a six-solenoid RF Helicon plasma source with a maximum mirror ratio of 1.44 between an axial magnetic field strength of 1000 G located 28 cm

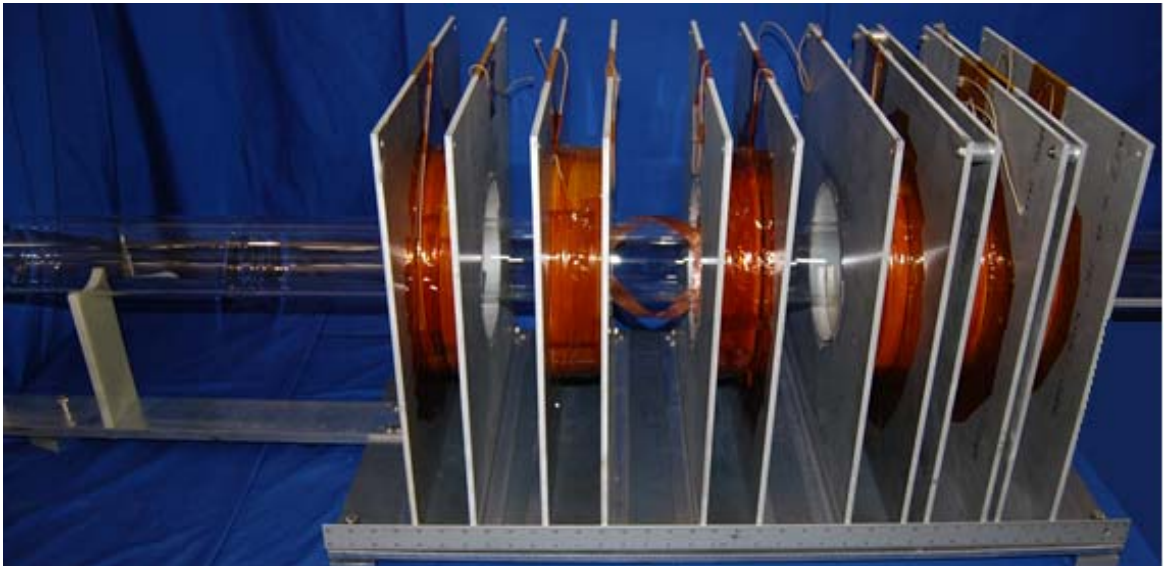


Figure 5.1: Fully assembled MadHeX replica. (Yard stick included for scale.)

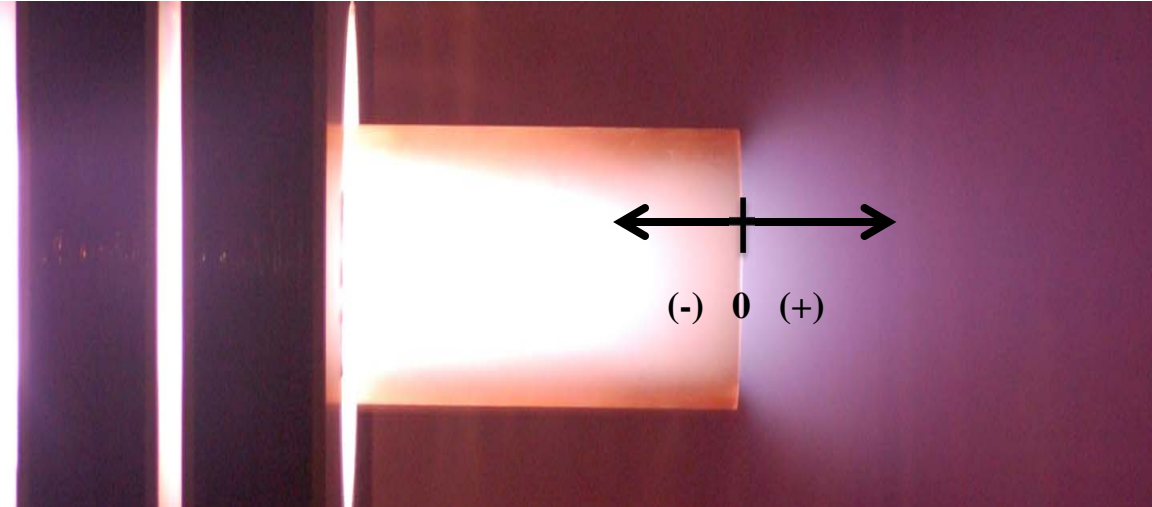


Figure 5.2: MadHeX replica exit area. Centerline along which measurements are recorded denoted by axis; 0 coordinated corresponds to exit plane.

downstream of the antenna and an axial magnetic field strength of about 700 G in the source region. The argon plasma properties and thruster design of the MadHeX have been highly characterized by Wiebold at the University of Wisconsin-Madison (UW-Madison) who observed both the Double Layer acceleration mechanism and Helicon RF coupling mode during the MadHeX's operation.^{7,21-22} The MadHeX replica at the Georgia Institute of Technology has six 500-turn solenoids arranged around a 10-cm diameter Pyrex discharge chamber. The positioning of the solenoids as well as their physical dimensions and the dimensions of the half-turn, double helix antenna are identical to those of the MadHeX at the UW-Madison. The exit plane of the MadHeX replica is approximately 60 cm away from the downstream edge of the RF antenna. The magnetic field profile of the MadHeX replica is verified through experimental measurements using a Gaussmeter and magnetic field simulations performed using Infolytica MagNet commercial software.

Unlike the experimental setup at UW-Madison, there is no steel mesh surrounding the discharge chamber and there is no aluminum endplate at the propellant inlet. During testing, the entire thruster assembly at Georgia Tech is operated completely inside the

Vacuum Test Facility-1 (VTF-1) at a location that placed the center of the exit plane approximately 0.8 m radially away from the facility sidewall and approximately 3.5 m axially away from the graphite beam dump at the rear of the facility.

High-purity (99.9995%) argon propellant is fed to the thruster propellant inlet using stainless-steel Swagelok lines with a 3 cm nylon hose connector at the Pyrex propellant inlet. Propellant flow rate is regulated by an MKS 1179A mass flow controller calibrated before each testing cycle. The mass flow controller has an uncertainty up to 7%.²⁶ The RF signal for the MadHeX replica is generated by a Yaesu FT-540 HF transceiver and amplified by an ACOM2000A linear amplifier. The matching network used is a custom Pi-type network and the standing wave ratio (SWR), measured by an LP-100 wattmeter, is held below 1.05 for all experiments with an uncertainty of ± 1 W for power and ± 0.05 for SWR.²⁷ An electrical set-up identical to that shown in Fig. 2.2 is employed.

5.2 Vacuum Test Facility-1

In order to quantify the effect of neutral ingestion due to background pressure, two separate vacuum environments are required. Using Randolph's suggested threshold for HET performance evaluation as a guide, two facility environments are used to evaluate the effect of neutral ingestion on Helicon ion thruster operation.²⁵ The 'high-pressure condition' (Sec. 5.2.1) operates above Randolph's limit of 5×10^{-5} Torr and the 'low-pressure condition' (Sec. 5.2.2) operates below Randolph's limit. Both pressure conditions are generated inside VTF-1 at the Georgia Tech High-Power Electric Propulsion Laboratory (HPEPL) shown in Fig. 5.3.



Figure 5.3 Vacuum Test Facility–1 at Georgia Tech.

The VTF–1 measures 7 m long and 4 m in diameter. For this work, different configurations of pumps will be used in order to change chamber pumping speeds to allow thruster characterization at both pressure conditions. For both pressure conditions, the chamber is evacuated to moderate vacuum (base pressure of 0.03 Torr) by two 3800 CFM blowers and two 495 CFM rotary-vane pumps. Facility operation differs beyond this point depending on the desired pressure condition and is detailed in the following sections. Pressure in VTF-1 is measured using an Agilent BA 571 hot filament ionization gauge mounted externally to VTF-1 controlled by an Agilent XGS-600 Gauge Controller. Operating pressure is corrected for argon. Pressure measured by the ion gauge has an uncertainty of +20% to –10%.²⁸ Probe positions in VTF-1 are controlled using a two-axis Parker Daedal 406XR precision linear motion stage system with a positional uncertainty for each motion stage of $\pm 159 \mu\text{m}$.

5.2.1 High-pressure condition

The ‘high-pressure condition’ reaches a base pressure of about 2.9×10^{-4} Torr and ranges in operating pressure from 3.0×10^{-4} Torr to 3.7×10^{-4} Torr corrected for argon. This condition is achieved by shutting off the CFM blowers and CFM rotary-vane pumps after moderate vacuum is achieved and engaging an Edwards STP-XA3203 turbomolecular pump with a pumping speed of 3200 L/s on nitrogen to get down to the final base pressure. An Edwards GV80 dry scroll pump provides vacuum line back pumping for the turbopump with a maximum pumping speed of 64.6 CFM.

5.2.2 Low-Pressure Condition

The ‘low-pressure condition’ reaches a base pressure of about 1.0×10^{-5} Torr and ranges in operating pressure from 1.2×10^{-5} Torr to 2.4×10^{-5} Torr corrected for argon. This condition is achieved using six NRC/CVC Varian HS48-95,000 fractionating diffusion pumps with copper baffles chilled by three Polycold fast cycle water vapor cryopumps running on HC 1100 refrigerant yielding a total pumping speed of 125,000 L/s on argon.⁹

5.3 Diagnostics

5.3.1 RF Compensated Emissive Probe

The plasma potential is the average local potential at a given location in the plume of the thruster. An emitting, RF-compensated emissive probe shown in Fig. 5.4 is used to measure plasma potential in this work.

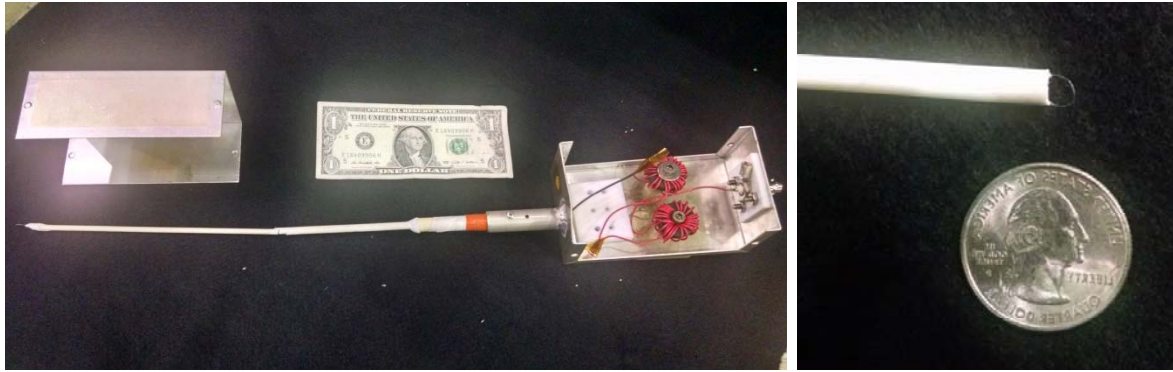


Figure 5.4: (Left) RF-compensated probe assembly with emissive probe tip attached and RF-compensation circuit. (Right) Tungsten loop probe tip.

The probe tip is a thoriated-tungsten wire curved into a 0.127 mm diameter loop fed through a 1.5-mm diameter, double bore ceramic tube. The double-bore ceramic tube is inserted into another ceramic tube that is secured to the RF compensation box. The compensation box houses two, M-series ferrite toroids (one on each side of the probe tip) each wrapped 25 times with the signal wire to remove RF interference from the recorded data. Each choke provides an impedance of 5600 Ohms for an RF signal of 13.56 MHz.⁹ The overall probe length is approximately 84 cm. The probe is oriented perpendicular to the bulk flow of the plasma and perpendicular to the magnetic field. The plane of the probe tip is oriented parallel to the thruster exit allowing plasma to pass through the loop after exiting the thruster.¹⁰

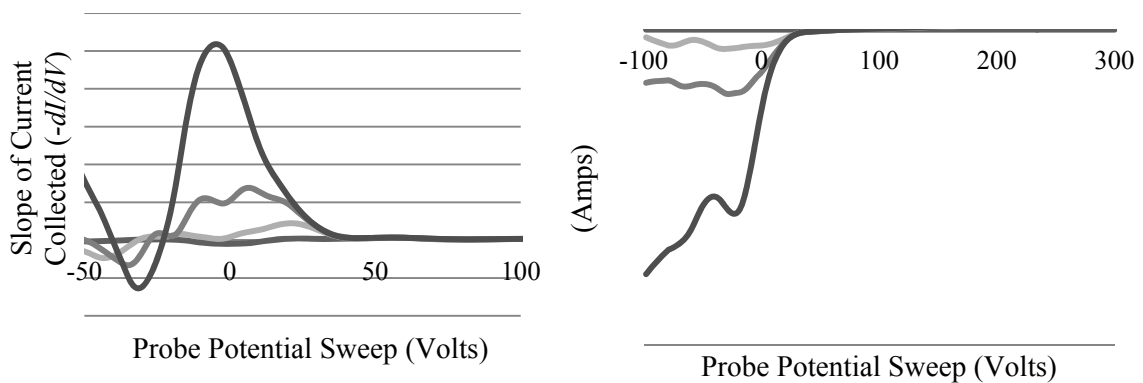


Figure 5.5: (Left) Sample of smoothed I-V curves at multiple heating currents. (Right) Derivative curves of each I-V curve at different heating currents.

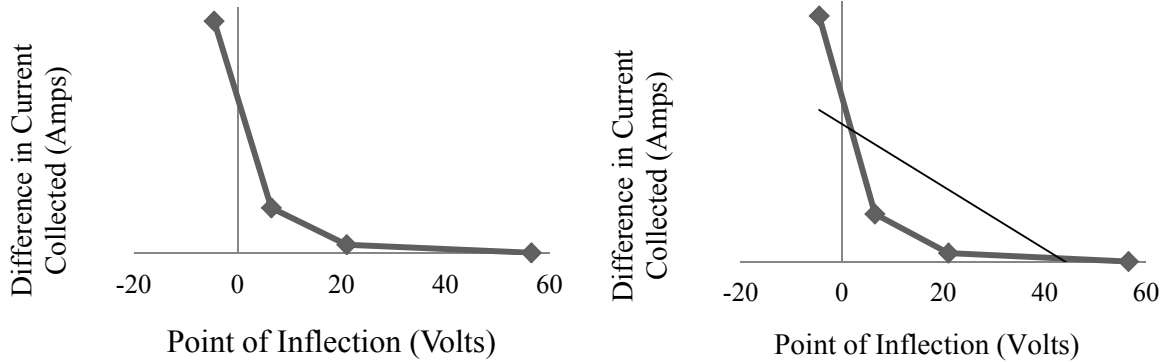


Figure 5.6: (Left) Sample plot of difference in ion current (ion current collected for the non-emitting case – ion current collected during emission) vs. the voltage at which the maximum derivative occurs. (Right) Sample linear trend line fitted to data to determine local plasma potential at point of zero emission.

The thoriated-tungsten probe tip emits electrons at a constant heating current while the probe bias is swept across a voltage potential range of interest. A current-voltage (I-V) trace is generated for that particular heating current. Several traces are recorded for multiple heating currents at the same thruster operating condition and at the same probe location.

Plasma potential is determined using the Inflection Point Method.²⁹⁻³⁰ The derivatives for each curve are calculated to determine the voltage associated with the maximum of the $-dI/dV$ curve shown in Fig 5.5 (right). The associated voltage for each maximum is plotted for each curve against the difference in current between the ion saturation current of the emitting case and the ion saturation current of a non-emitting case as shown in Fig 5.6 (left). A linear trend can be inferred from this data and the voltage for the non-emitting case can be calculated as the voltage at which the difference in current is zero illustrated in Fig 5.6 (right). This voltage is the local plasma potential.

Electron emission from the thoriated-tungsten tip is achieved by providing a constant DC current from a Xantrex XPD 60-9 power supply. A Keithley 2410 Sourcemeter is used to bias the probe as well as collect the current emitted and current collected at the probe tip. These values are all recorded using an Agilent 34970A data acquisition unit (DAQ). LabView is used to control the instruments and capture the I-V trace. Excel is used to plot the data, calculate each curve derivative, find each curve maximum, and predict the potential at a point of zero emission. To prevent noise from affecting the derivative of the I-V trace leading to false maximum values, LOESS smoothing is used with a smoothing parameter of 0.1.

Uncertainty from the use of the inflection point method is on the order of $\pm T_e/10$ which is calculated to range between 0.2 V and 0.6 V in this work. Probe tip heating produces an offset of the resulting plasma potential due to a voltage drop across the entire probe circuit of approximately half of the heating voltage applied. The potential drop across the probe tip is estimated to be approximately (3.5-5) V for all cases; all emissive probe data is inflated by (3.5-5) V. Total instrument uncertainty is about 0.03%.³¹⁻³² Error due to smoothing falls within the error of the inflection point method and is considered negligible in comparison.

5.3.2 Retarding Potential Analyzer

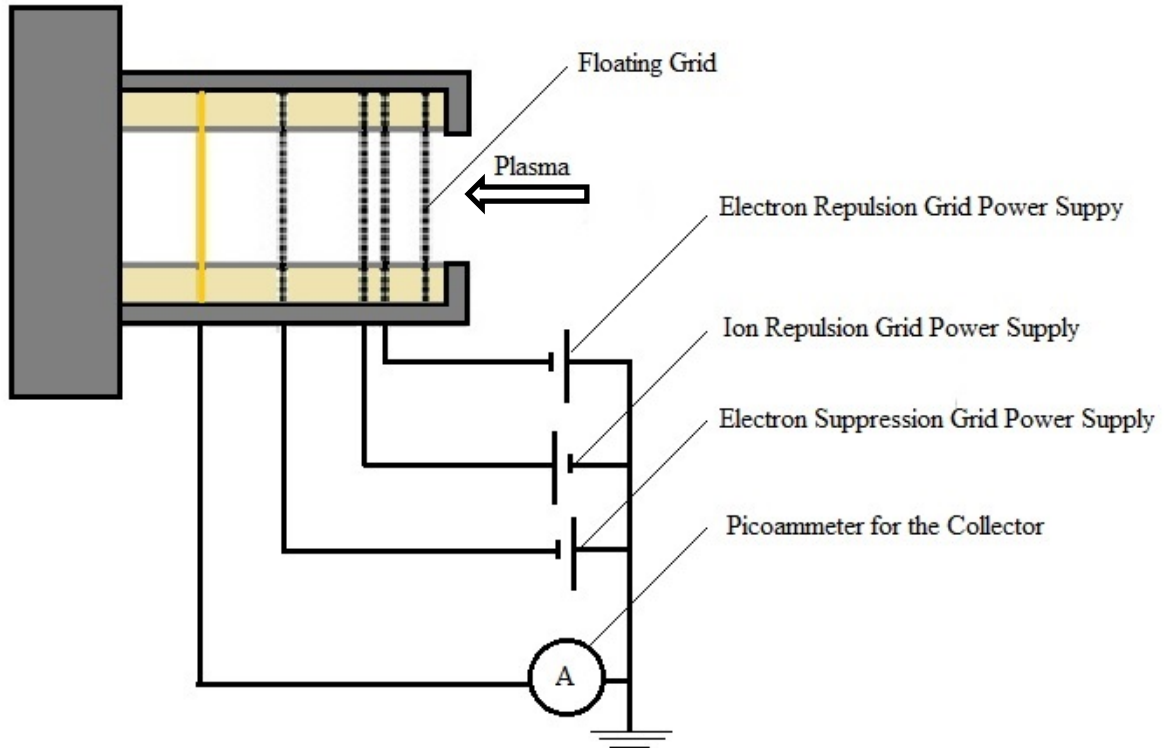


Figure 5.7: Electrical schematic of four-grid, AFRL designed RPA.

The IEDF is required to determine the most probable voltage or the potential associated with the accelerated ion beam. The IEDF is measured using a four-grid, AFRL designed Retarding Potential Analyzer (RPA).³³

The RPA in this study has four grids and an ion current collector. As illustrated in Fig 5.7, the order of the grids from plasma to collector is: floating, electron repulsion, ion repulsion, electron suppression, and a solid copper collector that is 0.8 mm thick and 3.15 cm in diameter.⁹ All the RPA grids are made of 316 stainless steel and are each 203- μm thick with a collection diameter of 3.15 cm. Each grid has a 31% transparency with aperture diameters of 229- μm arranged at a 394- μm pitch in a hexagonal hole pattern. The RPA is oriented along the centerline of the discharge chamber with the floating grid

facing the open end of the Helicon ion thruster. The chassis of the RPA remains floating during data collection along with the floating front grid. Preliminary sweeps were recorded for both floating and grounded chassis configurations with negligible difference in sweep behavior. The electron repulsion grid is biased negative to ground in order to prevent electrons from entering the RPA. The ion repulsion grid is swept across a voltage range of interest until the current on the collector reaches zero. The electron suppression grid is biased negative relative to ground to prevent electrons that are sputtered from the collector from being collected on the ion repulsion grid.

During data collection, all grid biases are held constant except for the ion repulsion grid. An I-V trace from the current measured on the collector is generated as the ion repulsion grid sweeps across a voltage range of interest until current collection reaches 0 A. The negative derivative of the I-V trace is calculated as shown in Fig. 5.8. The derivative represents the distribution of ion energies. The associated voltage for the maximum $-dI/dV$ value is the uncorrected most probable voltage. To calculate the corrected most probable voltage, the plasma potential must be subtracted as illustrated in Eq. 2.3. This analysis method is described in Reference 34.

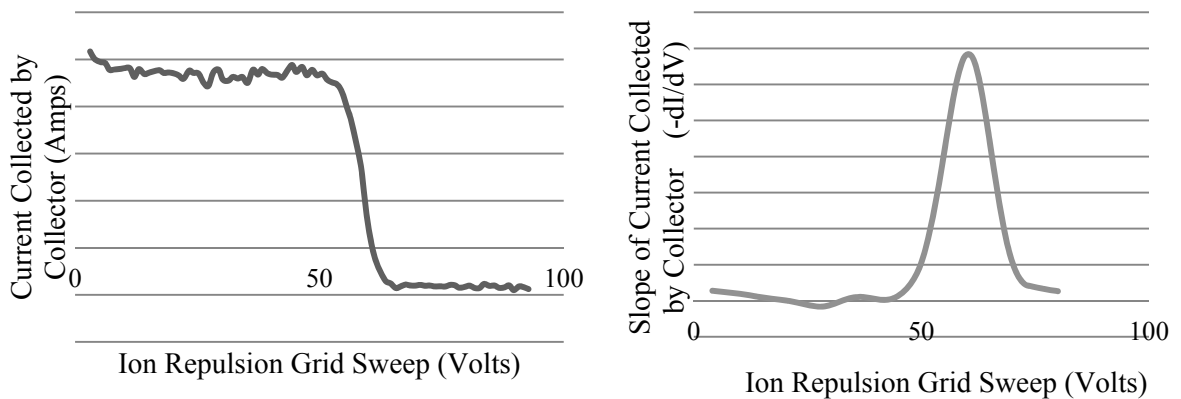


Figure 5.8: Sample smoothed I-V curves from RPA (Left). Sample derivative trace of I-V curve (Right).

Ion current is collected using a Keithley 6485 Picoammeter. Ion repulsion grid voltage is supplied by a Keithley 2410 Sourcemeter. These values are collected by the DAQ and stored in LabView. Before taking measurements at each operating condition, the RPA bias scheme is optimized by adjusting the potential of the electron repulsion and electron suppression grids separately, while in the plasma plume, until maximum ion current is collected.

Error for this analysis method of the IEDF sweeps is approximately $\pm 4\%$.⁹ Total instrument uncertainty (accounting for error in picoammeter, sourcemeter, and DAQ) is less than 0.03%.³¹⁻³² Error due to smoothing falls within the error of the analysis method and is considered negligible in comparison.

5.3.3 RF-Compensated Langmuir Probe



Figure 5.9: (Left) RF-compensated probe assembly with Langmuir probe tip attached and modified compensation circuit. (Right) Planar tungsten probe tip.

The final diagnostic, an RF-compensated Langmuir probe, determines the electron temperature and ion number density in the plasma plume. The Langmuir probe also provides an alternative plasma potential measurement for determining electron temperature along with the plasma floating potential.

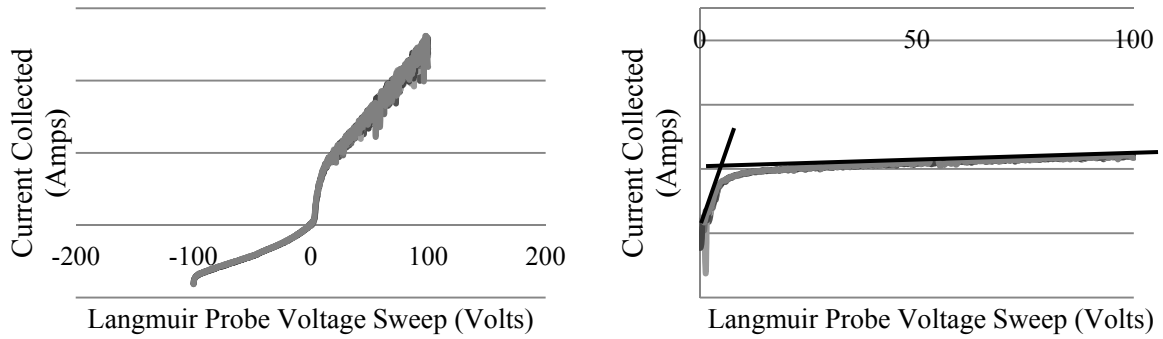


Figure 5.10: (Left) Sample I-V curves from Langmuir probe voltage sweep. (Right) Sample log plot of I-V curve with intersecting trend lines to determine plasma potential.

The same probe assembly as described in Sec. 4.3.1 is used for the Langmuir probe. In order to filter the RF waves during data collection as a Langmuir probe, the toroids are placed in series ahead of the probe tip in the signal line. A planar tungsten probe tip of diameter (d_{probe}) 7.62 mm replaces the thoriated-tungsten loop as emission is not desired. Probe orientation is again perpendicular to bulk propellant flow and the magnetic field.³⁰ The plane of the probe tip disc is parallel to the exit plane of the thruster.

Ion current collected on the probe tip is recorded as the probe bias is swept over a voltage range of interest ending when the curve knees over reaching the electron saturation current. In order to calculate electron temperature and ion number density, several potentials of interest must first be determined. The floating potential (V_f) is the voltage where collected current is zero. Since the probe structures inside the chamber are not connected to ground, the floating potential represents the lowest potential available from the point of view of the plasma. Ion saturation current (I_{i_s}) must be collected at least 60 V below the plasma potential and for all cases is assumed to be the current from the I-V trace at -60 V.⁹ Plasma potential is determined as the voltage at which two linear trend lines corresponding to the two different sloped portions of the log plot of the I-V trace

intersect as shown in Fig. 5.10 (right).⁹ Plasma potential measured by the Langmuir probe is used primarily for calculation of electron temperature as the emissive probe is a more accurate method of plasma potential measurement.

Electron temperature is determined via the positive slope of the increasing portion of the I-V trace calculated using Eq. 5.2. Ion number density in $ions/m^3$ is calculated using Equation 5-3.

$$T_e(eV) = \frac{V_p - V_f}{5.2} \quad \text{Eq. 5.2}^{35}$$

$$n_i = (4.3 \times 10^{15}) \frac{I_{is}}{\sqrt{T_e(d_{probe})^2}} \quad \text{Eq. 5.3}^{35}$$

Current is collected using a Keithley 6485 Picoammeter. The voltage sweep is supplied by a Keithley 2410 Sourceter. These values are collected by the DAQ and stored in LabView. Uncertainty using this method of calculating electron temperature has an uncertainty of $\pm 17\%$.³⁵ Uncertainty associated with the ion number density calculation is $\pm 50\%$.³⁵ Total instrument uncertainty includes the picoammeter, sourceter, and DAQ and is less than 0.03% .³⁰⁻³¹

5.4 Uncertainty Analysis

Equipment and diagnostic uncertainties are summarized in Table 5.1. Equipment uncertainties include resolution and measurement uncertainty as well as accuracy limitations. Diagnostic uncertainties include the analysis method error as well as affiliated instrument uncertainties not captured in the general equipment errors.

Diagnostic uncertainties are combined in Table 5.2 to summarize the error associated with each plasma property measurement. These errors are used in the formation of the vertical error bars displayed on the experimental results presented in Chapter VI with the exception of the emissive probe voltage offset. Emissive probe plasma potential values presented in this work are not corrected for the heating voltage offset used for electron emission. All plasma potential values measured by the emissive probe are increased artificially by 3.5 to 5 V. Conversely, corrected most probable voltage values are artificially decreased by 3.5 to 5 V. Experimental results are also not altered to reflect the equipment errors listed in Table 5.1.

Table 5.1: Summary of equipment and diagnostic uncertainty.

| Equipment | | Uncertainty | |
|-----------------------------|----------------------|----------------------------|---------------|
| RF System Assembly | | ± 1 W & ± 0.05 SWR | |
| Mass Flow Controller | | ± 4 -7% | |
| Linear Motion Tables | | ± 159 μ m | |
| Ionization Gauge | | + 20% to -10% | |
| Diagnostic | Analysis | Instrument | Offset |
| Emissive Probe | $\pm T_e/10$ V | 0.03% | 3.5 – 5 V* |
| RPA | ± 4 % | 0.03% | - |
| Langmuir Probe | <i>See Table 5.2</i> | 0.03% | - |

*not reflected in experimental results

Table 5.2: Plasma property uncertainties due to diagnostic and analysis errors specific to the presented experimental results in Chapter VI of this work.

| Plasma Property | Uncertainty |
|------------------------------|--------------------|
| Most Probable Voltage | ± 4.03 % |
| Plasma Potential | ± 1 V |
| Electron Temperature | ± 17.03 % |
| Ion Number Density | ± 50.03 % |

CHAPTER VI

RESULTS

6.1 Neutral Ingestion Effects on Plasma Properties

The first portion of this study considers the effect of neutral ingestion caused by facility background pressure on individual plasma properties. Each property is considered in isolation for a thruster operating condition of 2 sccm argon volumetric flow rate, 340 G magnetic field strength in the source region, and approximately 100 W RF power. Properties considered include plasma potential, floating potential, the most probable voltage of the IEDF, the half maximum widths of the IEDF, electron temperature, ion number density, and ion saturation current. Measurements are recorded on the thruster centerline along the thruster's main axis with the 0 location representing the exit plane and numerically positive positions on the axis corresponding to locations of increasing distance downstream of the thruster exit as depicted in Fig 5.2

6.1.1 Neutral Ingestion Effects on Plasma Properties at the 'High-Pressure Condition'

The IEDF for the 'high-pressure condition' is measured from a distance of 79 mm upstream of the exit plane to a distance of 66 mm downstream of the exit plane. IEDFs become shorter and shift towards lower voltages as measurements move in the downstream direction as illustrated in Fig. 6.1. The uncorrected most probable voltage decreases from 29 V at a distance of -79 mm from the exit plane to 10 V at a distance of 66 mm from the exit plane with an average decrease of 0.13 V/mm along the thruster

centerline as shown in Fig. 6.2. Local plasma potential is a maximum of 4 V at the exit plane and decreases to about 1 V at a location of 66 mm downstream. The average decrease in plasma potential is ~ 0.05 V/mm. Corrected most probable voltage decreases linearly upon exiting the thruster.

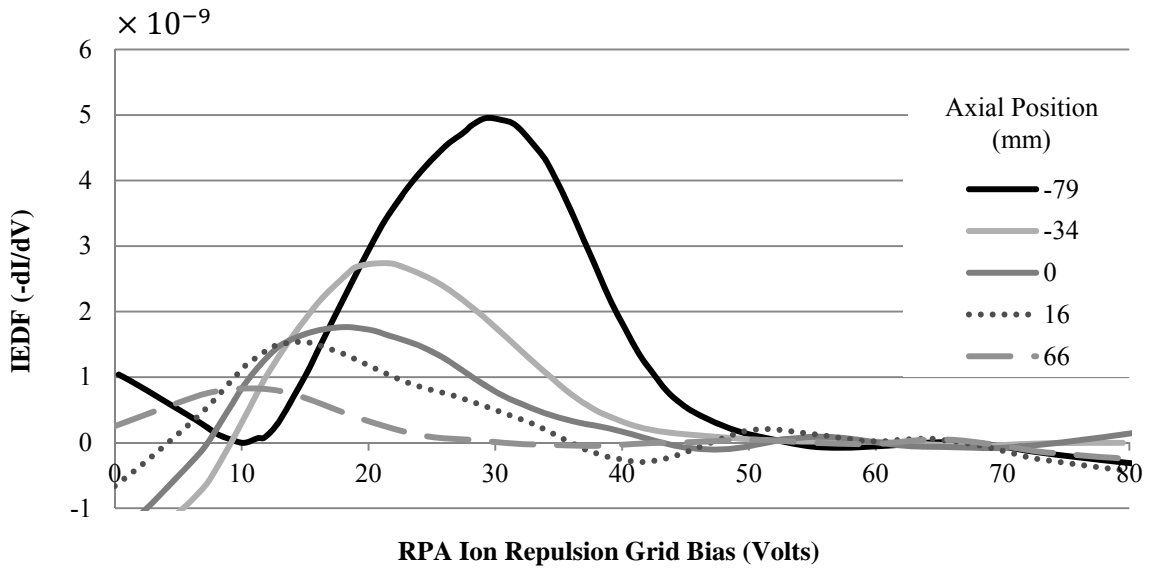


Figure 6.1: IEDFs recorded on thruster centerline for 2 sccm argon volumetric flow rate, 100 W RF power, and 340 G magnetic field strength thruster operating conditions at the 'high-pressure condition.'

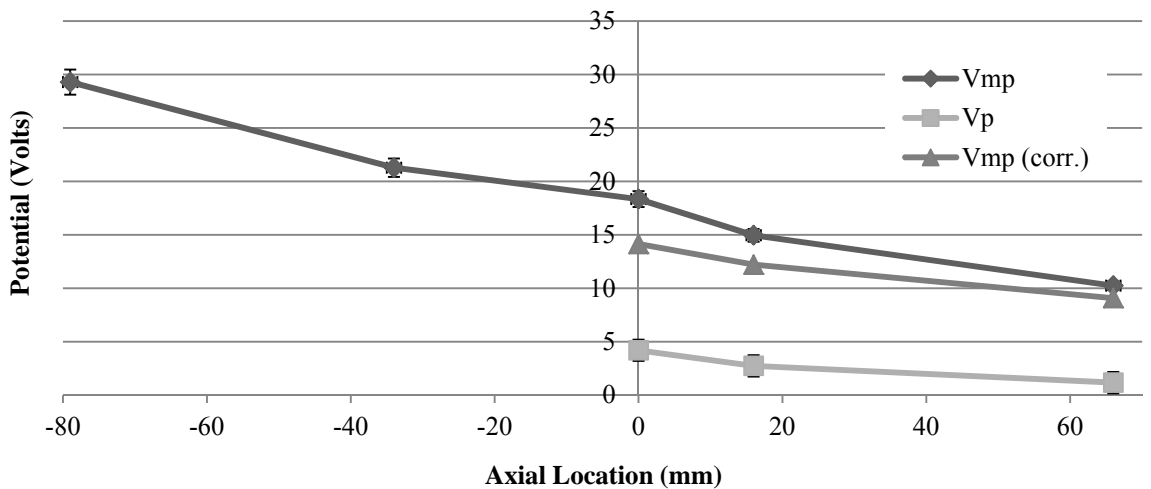


Figure 6.2: Most probable voltages recorded on thruster centerline for 2 sccm argon volumetric flow rate, 100 W RF power, and 340 G magnetic field strength thruster operating conditions at the 'high-pressure condition.'

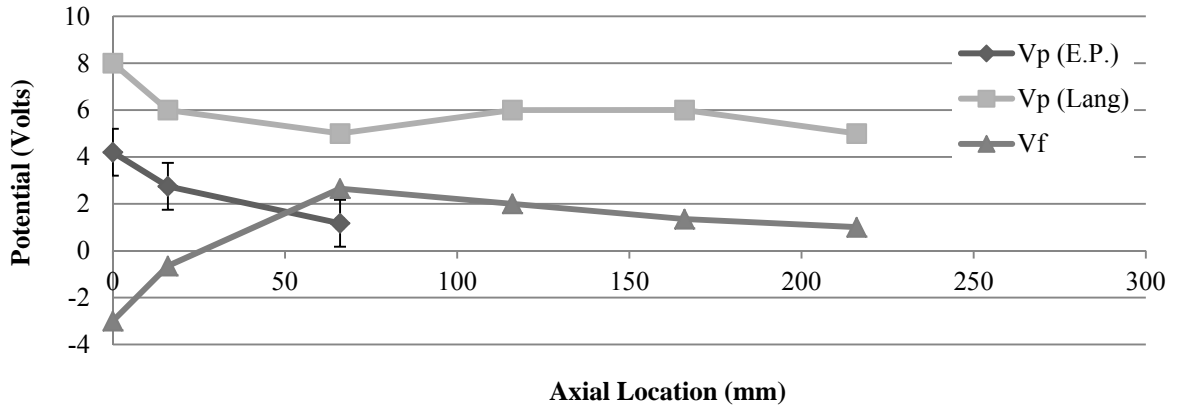


Figure 6.3: Potentials of interest recorded on thruster centerline by the emissive probe (E.P.) and the Langmuir probe (L.P.) for 2 sccm argon volumetric flow rate, 100 W RF power, and 340 G magnetic field strength thruster operating conditions at the ‘high-pressure condition.’

Potentials of interest include the plasma potential and floating potential measured by the Langmuir probe and the plasma potential measured by the emissive probe. Floating potential increases from the thruster exit from -3 V reaching a maximum of 2.65 V at a distance of 66 mm downstream of the exit plane after which it linearly decreases to 1 V at a distance of 216 mm from the exit plane. Plasma potential measured by the Langmuir probe decreases from 8 V to 5 V from the thruster exit plane to a distance of 66 mm downstream of the exit plane after which it remains steady fluctuating within 1 V of the 5 V value for the remaining 150 mm as seen in Fig. 6.3. Both the emissive probe and Langmuir probe plasma potentials decrease at a rate of 0.05 V/mm from the exit plane to a location 66 mm downstream of the exit plane.

Electron temperature for the ‘high-pressure condition’ is 2 eV at the exit plane and decreases to 0.5 eV at a location 66 mm downstream of the exit plane. For the remaining 150 mm, electron temperature remains within 0.5 eV of this minimum value as shown in Fig. 6.4.

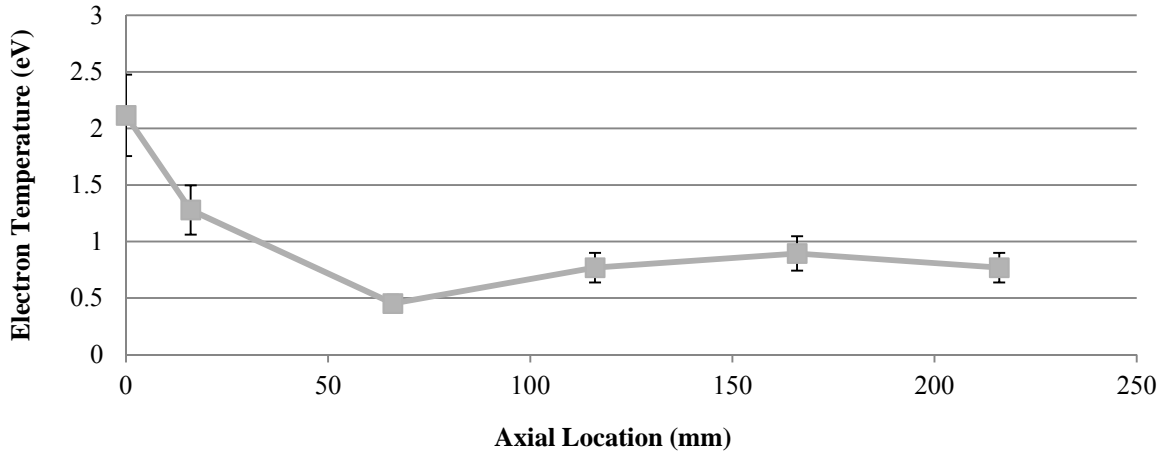


Figure 6.4: Electron temperatures recorded on thruster centerline for 2 sccm argon volumetric flow rate, 100 W RF power, and 340 G magnetic field strength thruster operating conditions at the ‘high-pressure condition.’

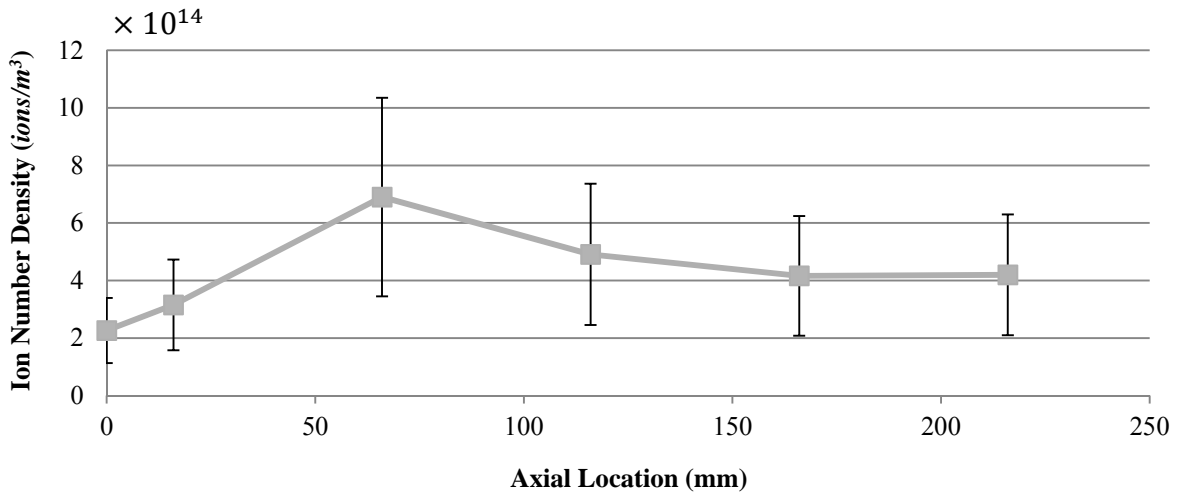


Figure 6.5: Ion densities recorded on thruster centerline for 2 sccm argon volumetric flow rate, 100 W RF power, and 340 G magnetic field strength thruster operating conditions at the ‘high-pressure condition.’

Ion number densities are calculated from the associated electron temperatures along the thruster axis using Eq. 5.3. Ion density increases from 2.3×10^{14} to 6.9×10^{14} ions/m³ from the exit plane to a distance 66 mm downstream of the exit plane. For the remaining 150 mm, ion density asymptotically approaches a value of 4.1×10^{14} ions/m³.

6.1.2 Neutral Ingestion Effects on Plasma Properties at the ‘Low-Pressure Condition’

The IEDF for the low-pressure condition is measured from a distance of 79 mm upstream of the exit plane to a distance of 216 mm downstream of the exit plane. IEDFs become shorter while the most probable voltages increase with increasing distance from the exit plane as shown in Fig. 6.6. The most probable voltage increases from 61 V at a distance of 79 mm upstream of the exit plane to 82 V at the exit plane, the largest increase in most probable voltage across the full range of interest as shown in Fig. 6.7. After exiting the thruster, the most probable voltage increases another 9 V to a final value of 91 V at a distance of 216 mm downstream of the exit plane. Plasma potential measured by the emissive probe on the other hand, decreases from 49 V at the thruster exit to 44 V at a distance of 16 mm downstream of the exit plane and then increases to 67 V at a distance of 66 mm from the exit plane. This behavior in plasma potential results in a corrected most probable voltage that increases from 33 V to 41 V over the 16 mm distance downstream of the exit plane and then falls to 21 V at a location of 66 mm downstream of the exit plane. This behavior is in opposition to the plasma potential determined using the Langmuir probe shown in Fig. 6.8.

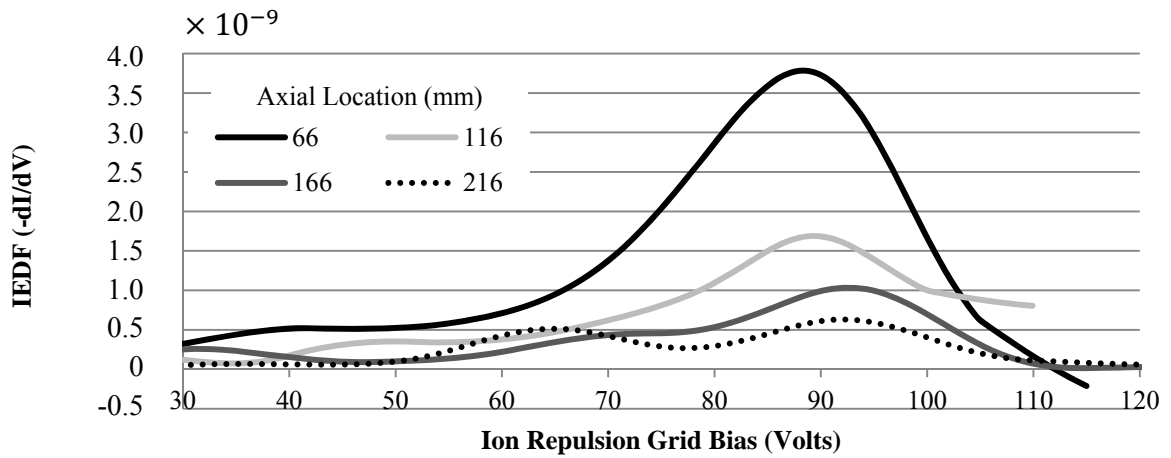
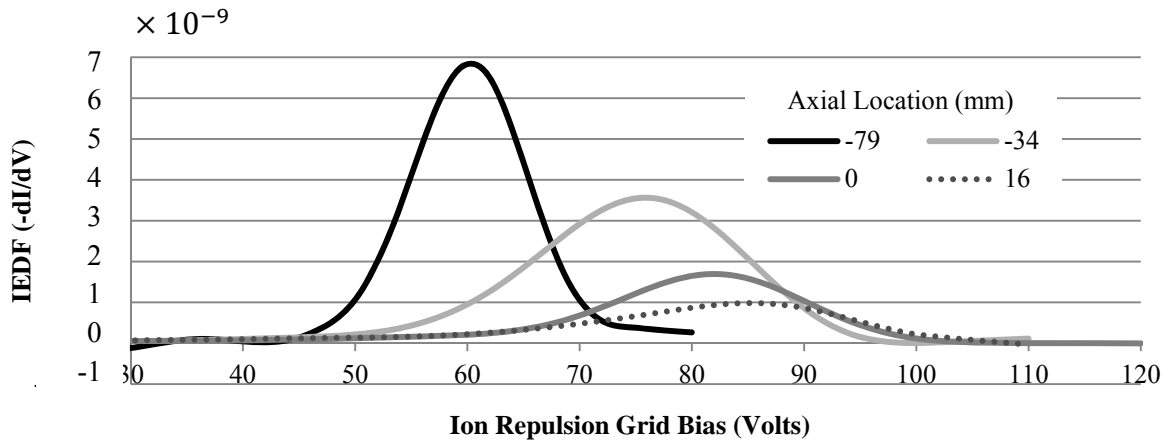


Figure 6.6: IEDFs recorded on thruster centerline for 2 sccm argon volumetric flow rate, 100 W RF power, and 340 G magnetic field strength thruster operating conditions at the ‘low-pressure condition.’

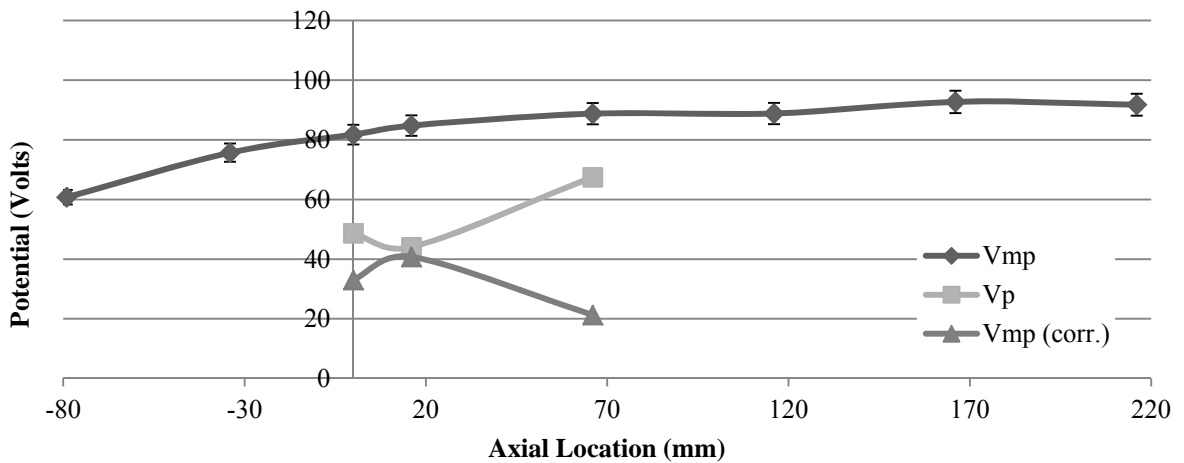


Figure 6.7: Most probable voltages recorded on thruster centerline for 2 sccm argon volumetric flow rate, 100 W RF power, and 340 G magnetic field strength thruster operating conditions at the ‘low-pressure condition.’

Plasma potential measured by the Langmuir probe increases from 65 V at the exit plane to 72 V at a distance of 16 mm downstream of the exit plane before decreasing to 45 V at a distance of 66 mm from the exit plane. Plasma potential then oscillates between 66 V and 45 V up to a distance of 216 mm downstream of the exit plane. This oscillating behavior is also observed in the floating potential data that decreases 10 V from a value of 33 V at the exit plane to 23 V at a distance of 66 mm downstream of the exit plane. Floating potential then oscillates between 55 V and 37 V until a distance of 216 mm from the exit plane. Despite the oscillating potentials, electron temperature remains steady at approximately 2 eV from a distance of 116 mm to a distance of 216 mm downstream of the exit plane as shown in Fig. 6.9. Electron temperature asymptotically approaches 2 eV after reaching a maximum temperature of 7 eV at a distance of 16 mm from the exit plane.

Despite a steady decrease in electron temperature, ion number density drops from 5.3×10^{13} ions/ m^3 at the exit plane to 2.8×10^{13} ions/ m^3 at a distance of 66 mm downstream from the exit plane after which it approaches its final value of 6.7×10^{13} ions/ m^3 at a distance of 216 mm from the exit plane as illustrated in Fig. 6.10. These oscillations, however, mostly remain within the 50% error of the ion number density estimation.

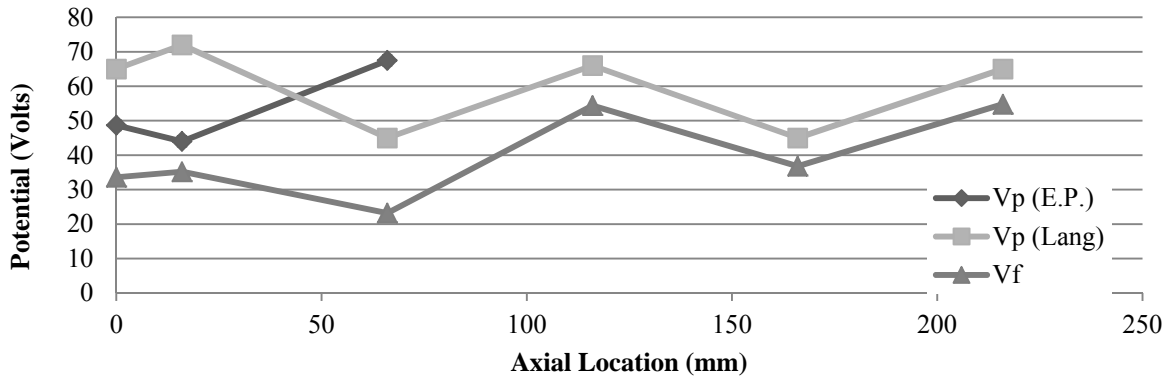


Figure 6.8: Potentials of interest recorded on thruster centerline by the emissive probe (E.P.) and the Langmuir probe (L.P.) for 2 sccm argon volumetric flow rate, 100 W RF power, and 340 G magnetic field strength thruster operating conditions at the ‘low-pressure condition.’

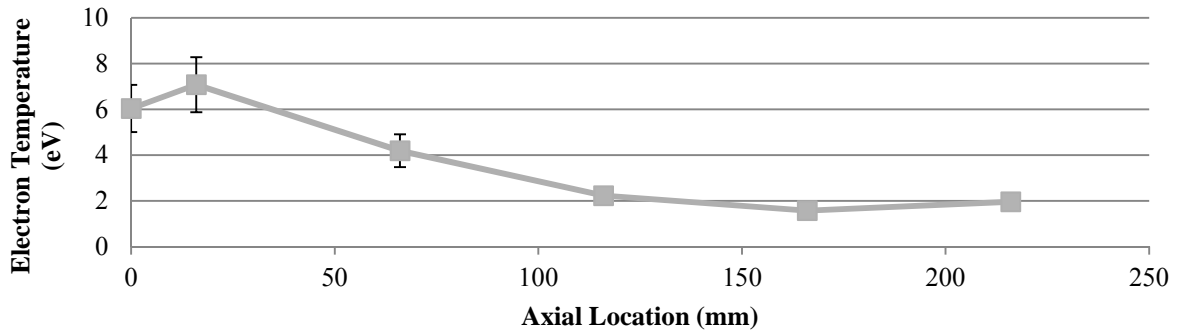


Figure 6.9: Electron temperature recorded on thruster centerline for 2 sccm argon volumetric flow rate, 100 W RF power, and 340 G magnetic field strength thruster operating conditions at the ‘low-pressure condition.’

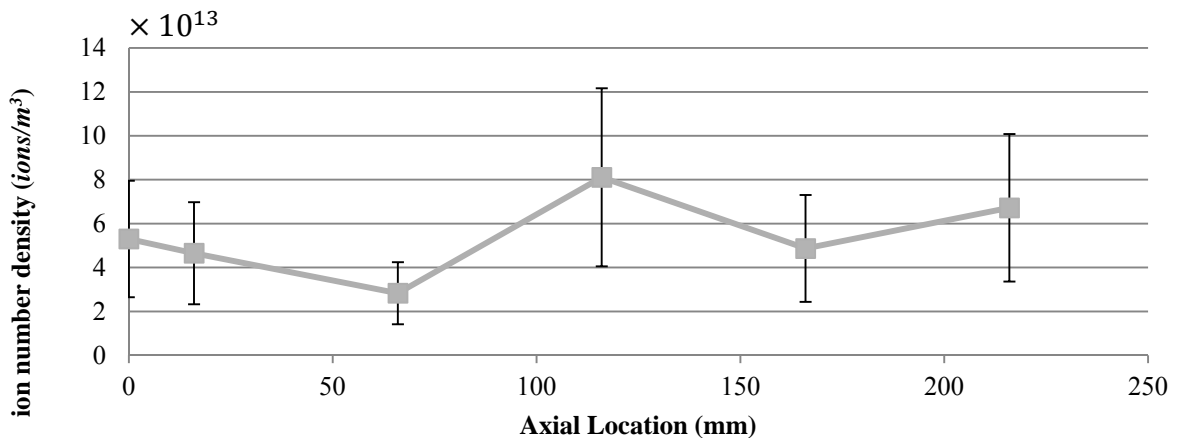


Figure 6.10: Ion number density recorded on thruster centerline for 2 sccm argon volumetric flow rate, 100 W RF power, and 340 G magnetic field strength thruster operating conditions at the ‘low-pressure condition.’

6.1.3 Comparison of Neutral Ingestion Effects on Plasma Properties Between Both Pressure Conditions

Direct comparison of uncorrected most probable voltage for the two pressure cases yields two separate trends. For the ‘low-pressure condition,’ most probable voltage increases approximately 20 V inside the thruster over a distance of 79 mm and then climbs 10 V in the next 66 mm downstream of the exit plane as shown in Fig. 6.11. The ‘high-pressure condition’ however, decreases 10 V inside the thruster from a distance of 79 mm upstream of the exit plane and drops another 10 V within 66 mm of the exit plane after exiting the thruster. Despite the different trends in uncorrected most probable voltage, corrected most probable voltage for both cases decreases from a distance of 16 mm to a distance of 66 mm downstream of the exit plane. Differences between the corrected most probable voltage for both pressure cases and the uncorrected most probable voltage for both pressure cases are shown in Table 6.1. The difference in uncorrected most probable voltage from the ‘low-pressure condition’ to the ‘high-pressure condition’ increases continuously from 31 V at a location 79 mm upstream of the exit plane to 79 V at a distance of 66 mm from the exit plane. The difference in corrected most probable voltage however reaches a minimum of 12 V at a distance of 66 mm from the exit plane.

Electron temperature at the exit plane for the low-pressure case is 4 eV higher than the electron temperature for the high-pressure case with a maximum difference of 6 eV at a location 16 mm downstream from the exit plane as shown in Fig. 6.12. Electron temperature decreases monotonically for both cases from a distance of 16 mm to 216 mm downstream of the exit plane to within a 1 eV difference with the ‘low-pressure

condition' still at a higher temperature of 2 eV. Both pressure cases have reached their final value by a distance of 116 mm from the exit plane.

Ion number density is four times higher for the 'high-pressure condition' than the low-pressure condition' at the exit plane as shown in Figure 6.13. Ion number density increases up to three times its exit plane value for the 'high-pressure condition' by a distance of 66 mm downstream of the exit plane after which ion number density asymptotically decreases approaching its final value of $4.1 \times 10^{14} \text{ ions/m}^3$.

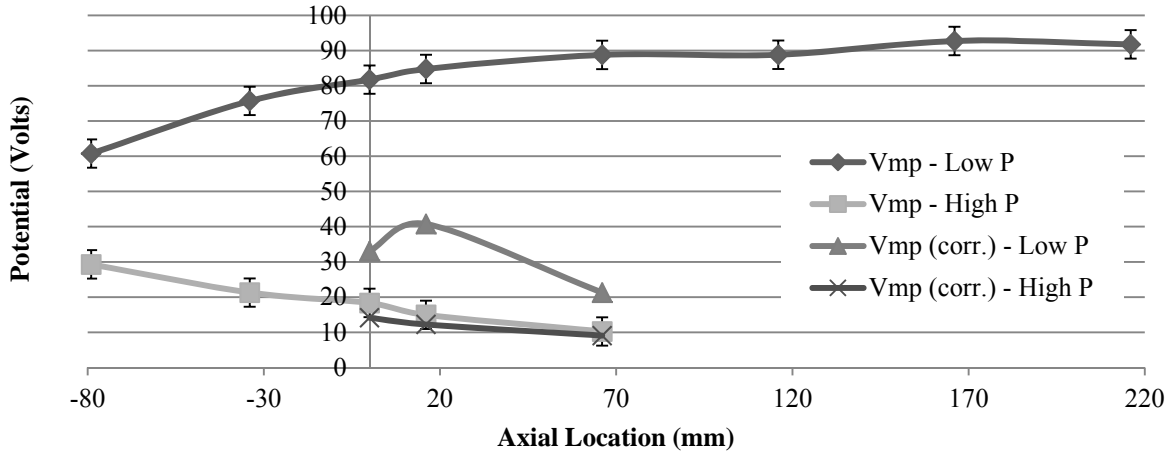


Figure 6.11: Most probable voltages recorded on thruster centerline for 2 sccm argon volumetric flow rate, 100 W RF power, and 340 G magnetic field strength thruster operating conditions at both the 'low-pressure condition' (Low P) and 'high-pressure condition' (High P).

Table 6.1: Differences in most probable voltages (corrected and uncorrected) recorded on thruster centerline for 2 sccm argon volumetric flow rate, 100 W RF power, and 340 G magnetic field strength thruster operating conditions between the 'low-pressure condition' and the 'high-pressure condition.'

| Position | -79 mm | -34 mm | 0 mm | 16 mm | 66 mm |
|---------------|--------|--------|------|-------|-------|
| $V_{mp,corr}$ | - | - | 19 V | 29 V | 12 V |
| V_{mp} | 31 V | 54 V | 63 V | 70 V | 79 V |

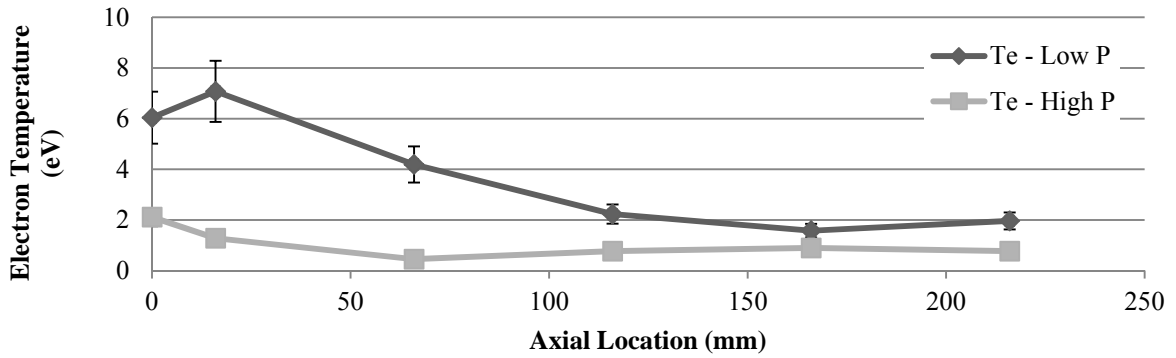


Figure 6.12: Electron temperature recorded on thruster centerline for 2 sccm argon volumetric flow rate, 100 W RF power, and 340 G magnetic field strength thruster operating conditions at both the ‘low-pressure condition’ (Low P) and ‘high-pressure condition’ (High P).

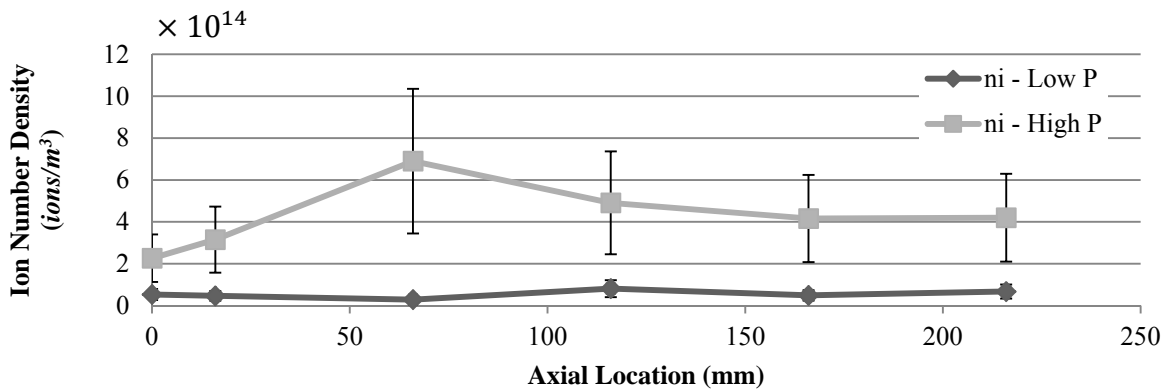


Figure 6.13: Ion number density recorded on thruster centerline for 2 sccm argon volumetric flow rate, 100 W RF power, and 340 G magnetic field strength thruster operating conditions at both the ‘low-pressure condition’ (Low P) and ‘high-pressure condition’ (High P).

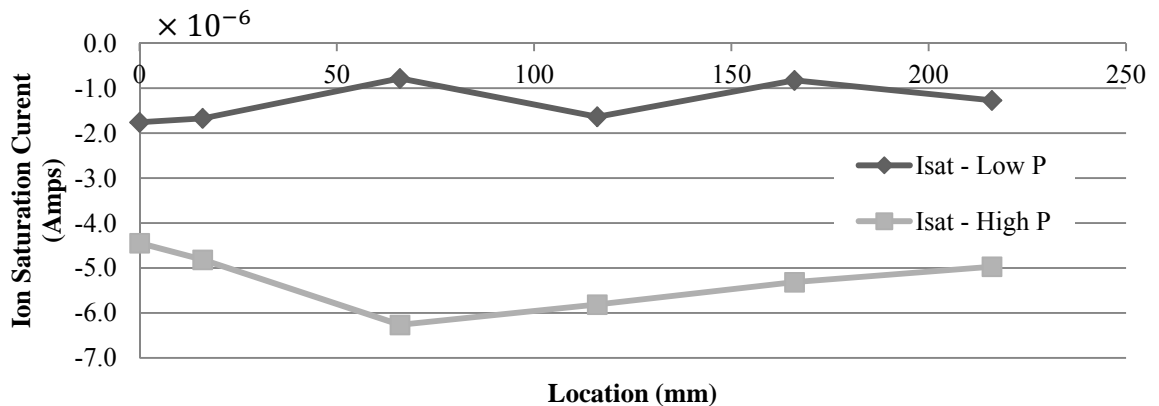


Figure 6.14: Ion saturation currents recorded on thruster centerline for 2 sccm argon volumetric flow rate, 100 W RF power, and 340 G magnetic field strength thruster operating conditions at both the ‘low-pressure condition’ (Low P) and ‘high-pressure condition’ (High P).

Despite differing behaviors, ion number density for both pressure conditions may be constant when allowing for analysis error across the distance of interest within each pressure condition considered. Ion number density for the ‘high-pressure condition’ however, remains consistently greater than ion number density at the ‘low-pressure condition’ even when accounting for analysis error. Ion number density behavior for both cases follows the trends exhibited in the ion saturation current as shown in Fig. 6.14. The magnitude of ion current for both cases is in the 10^{-6} A range with the ion saturation current for the ‘high-pressure condition’ consistently greater by a minimum of 1.7×10^{14} A as compared to the ion saturation current at the ‘low-pressure condition.’

6.2 Neutral Ingestion Effects and Operating Parameters

The next portion of this study considers the effect of neutral ingestion caused by facility background pressure on individual plasma properties when changing the thruster operating parameters. Plasma properties are measured over an RF power range of 100 W to 500 W (up to 700 W for some cases) and a source region magnetic field strength of 340 G to 500 G (up to 700 G for some cases). The MadHeX replica maintains a 2 sccm argon volumetric flow rate for all cases. The magnetic field strength is maintained at 340 G when changing RF power. The RF power is maintained at 100 W when changing the magnetic field strength in the source region. Properties considered include plasma potential, floating potential, the most probable voltage of the IEDF, half maximum widths of the IEDF, electron temperature, ion number density, and ion saturation current.

Measurements are recorded on the thruster centerline at the exit plane except when noted otherwise.

6.2.1 Effect of Increasing RF Power on Neutral Ingestion Influence at the ‘High-Pressure Condition’

The IEDFs for the ‘high-pressure condition’ are measured at the thruster exit plane over a range of 100 W to 527 W forward RF power. The IEDF for the 100 W case is the tallest distribution at the lowest uncorrected most probable voltage of 18 V as shown in Fig. 6.15. Uncorrected most probable voltage shifts to higher voltages with increasing RF power settling at 30 V for the 527 W case as shown in Fig. 6.16. Conversely, plasma potential does not experience a sizable increase and remains between 5 V to 10 V for all power levels considered.

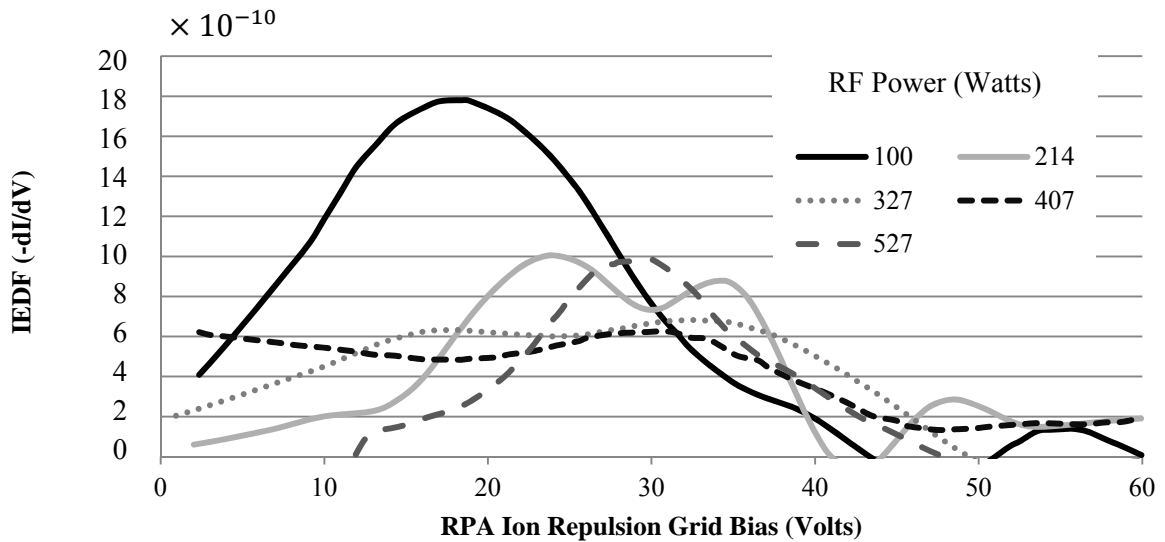


Figure 6.15: IEDFs recorded at the exit plane for 2 sccm argon volumetric flow rate and 340 G magnetic field strength thruster operating conditions over an RF power range of 100 W – 500 W at the ‘high-pressure condition.’

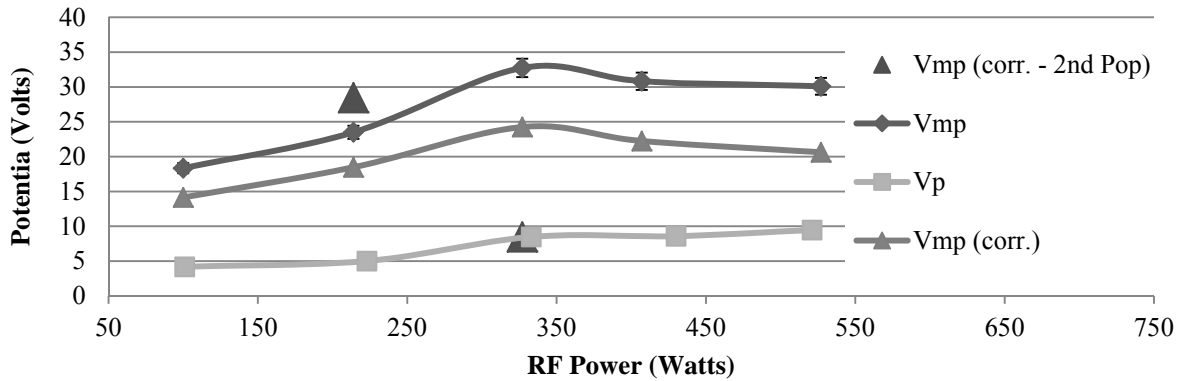


Figure 6.16: Most probable voltages (corrected) recorded at the exit plane for 2 sccm argon volumetric flow rate and 340 G magnetic field strength thruster operating conditions over an RF power range of 100 W – 500 W at the ‘high-pressure condition.’

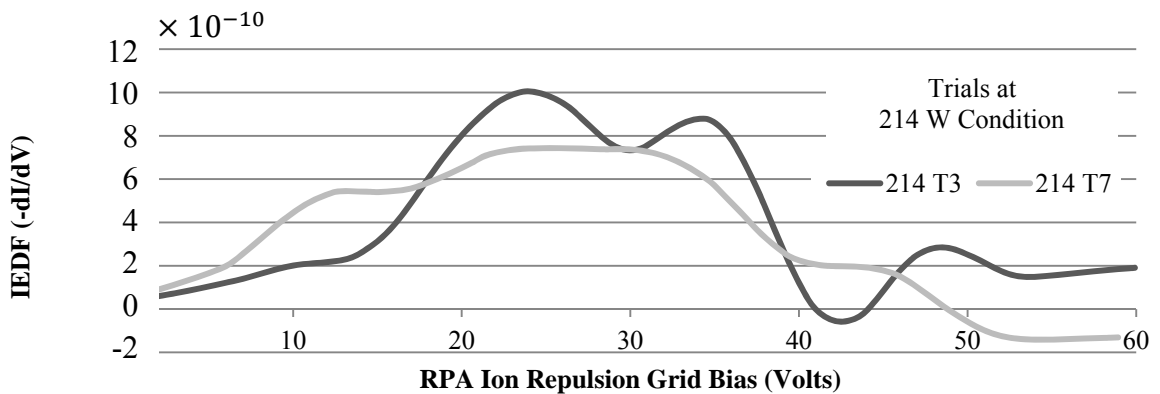


Figure 6.17: IEDFs for Trials 3 (T3) and 7 (T7) recorded at the exit plane for 2 sccm argon volumetric flow rate, 214 W RF power, and 340 G magnetic field strength thruster operating condition at the ‘high-pressure condition.’

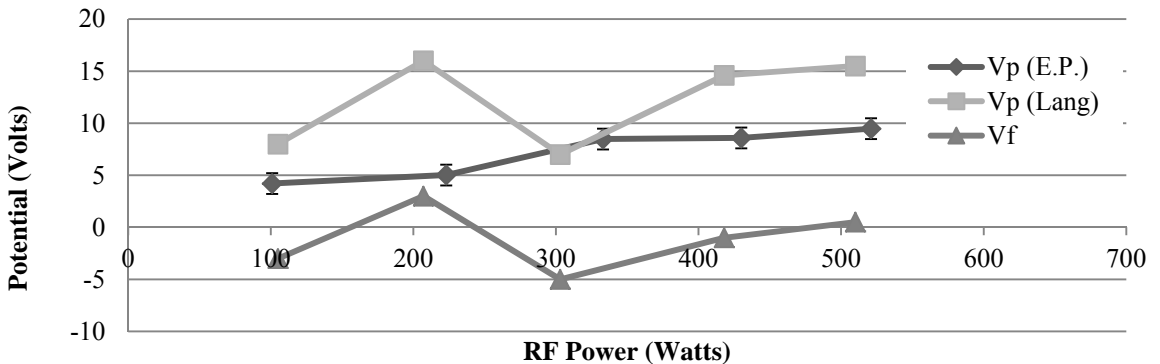


Figure 6.18: Potentials of interest recorded at the exit plane by the emissive probe (E.P.) and the Langmuir probe (L.P.) for 2 sccm argon volumetric flow rate and 340 G magnetic field strength thruster operating conditions over an RF power range of 100 W – 500 W at the ‘high-pressure condition.’

Further examination of the 214 W condition on Fig. 6.17 shows two distinct maximums on the IEDF for the third trial (T3) at 2 sccm argon volumetric flow rate and 340 G magnetic field strength. The seventh trial (T7) at the 214 W condition shows a 27 V wide, single maximum distribution. Changes observed in the distribution profile may be due to probe resolution or indicate an oscillating RF sheath or a non-steady state Double Layer condition.²⁰

The corrected most probable voltages for T3 of the 214 W condition shown in Fig 6.16 are 18 V and 28 V. The 327-W RF power condition may also have two distinct ion energy populations upon examination of Fig. 6.15. These two populations shown on Fig. 6.16 are located at 8 V and 24 V with the lower energy population close to the 8.5 V plasma potential. The primary corrected most probable voltage populations are considered to be the voltages at which the absolute maximum of each ion energy distribution is located. All primary corrected most probable voltages follow the behavior of the uncorrected most probable voltages across the full range of RF powers considered.

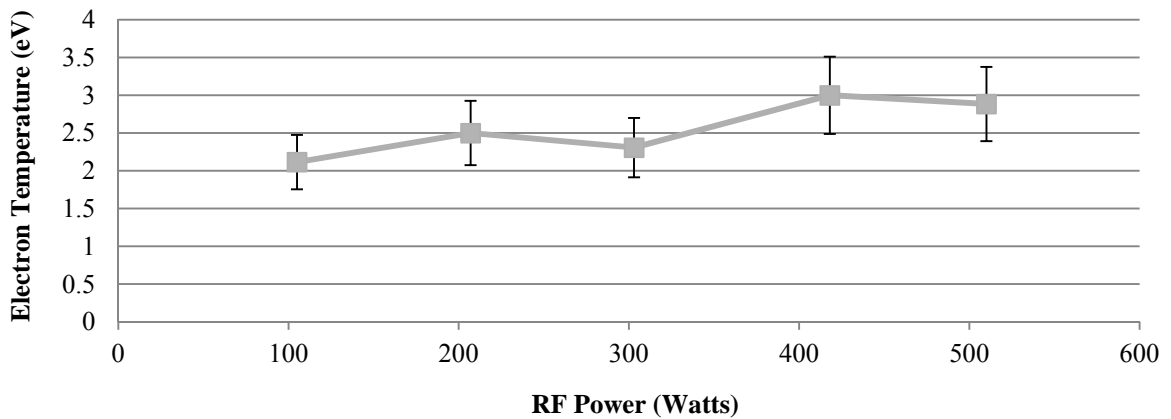


Figure 6.19: Electron temperatures recorded at the exit plane for 2 sccm argon volumetric flow rate and 340 G magnetic field strength thruster operating conditions over an RF power range of 100 W – 500 W at the ‘high-pressure condition.’

Plasma potential determined using emissive probe data is recorded for RF power levels ranging from 101 W to 521 W. The electron temperature and ion number density from the Langmuir probe is recorded over a range of 105 W to 510 W RF power. Both traces are displayed in Fig. 6.18. Plasma potential recorded using the emissive probe measures between 5 V to 10 V across the entire range of RF power levels. Plasma potential measured from the Langmuir probe is within ± 6 V of the 10 V potential at the 100 W RF power condition. Plasma potential measured from the Langmuir probe I-V sweeps follows the behavior of the floating voltage that stays within ± 6 V of the -3 V floating voltage at the 100 W RF power condition.

Electron temperature determined from the Langmuir probe sweeps stays between 2.3 eV and 3 eV across the entire range of RF power considered as shown in Fig. 6.19. Ion number density from the Langmuir probe data remains relatively constant up to the 300 W case after which ion number density increases from 2.5×10^{14} ions/m³ to 7.0×10^{14} ions/m³ over the last 200 W of the RF power range as shown in Fig. 6.20.

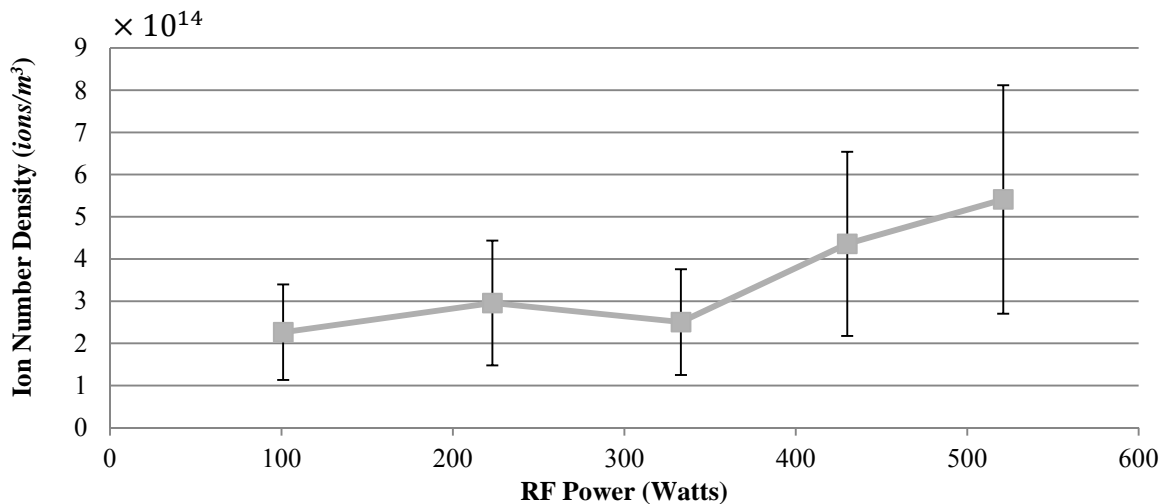


Figure 6.20: Ion number densities recorded at the exit plane for 2 sccm argon volumetric flow rate and 340 G magnetic field strength thruster operating conditions over an RF power range of 100 W – 500 W at the ‘high-pressure condition.’

6.2.2 Effect of Increasing RF Power on Neutral Ingestion Influence at the ‘Low-Pressure Condition’

The IEDF for the ‘low-pressure condition’ and corresponding most probable voltages are recorded over an RF power range of 116 W to 319 W at a distance of 16 mm from the exit plane. Ion energies are recorded in power ranges adjacent to the 214 W condition due to interest in the double peaked IEDF observed for the ‘high-pressure condition.’ IEDFs are recorded at a distance of 16 mm downstream of the exit plane instead of at the thruster exit to increase the likelihood of observing Double Layer formation should one exist at the ‘low-pressure condition.’ By recording downstream of the expected Double Layer, any Double Layer formed at any point upstream of the RPA will be captured on the IEDF.¹⁹ The inconsistency in Double Layer formation at the ‘high-pressure condition’ may be due to its formation on the exit plane, a source of error eliminated in the measurements for the ‘low-pressure condition’ by measuring the IEDF at a distance of 16 mm downstream of the exit plane.

IEDFs pictured in Fig. 6.21 are single peaked and increase in most probable voltage from 90 V at the 116 W condition to 135 V at the 319 W condition. Plasma potential measured from the emissive probe ranges between 49 V and 26 V and still yields a consistently increasing corrected most probable voltage. The most probable voltage rises at a rate of approximately 0.26 V/W from 41 V at the 116 W operating condition to 94 V at the 319 W operating condition as shown in Fig 6.22. It is important to note that the most probable voltage is corrected using plasma potential measurements at the exit plane, the trends however are expected to remain.

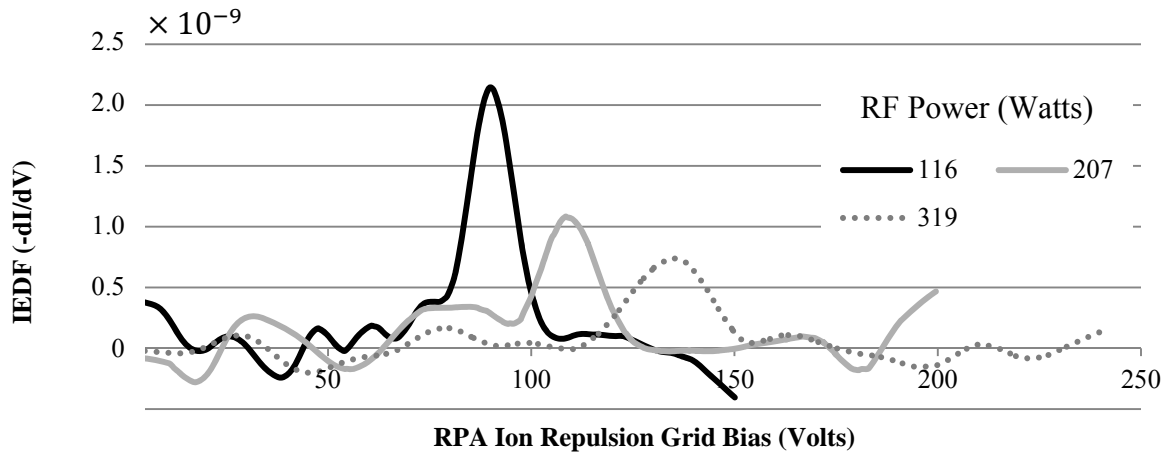


Figure 6.21: IEDFs recorded at a distance of 16 mm from the exit plane for 2 sccm argon volumetric flow rate and 340 G magnetic field strength thruster operating conditions over an RF power range of 116 W – 319 W at the ‘low-pressure condition.’

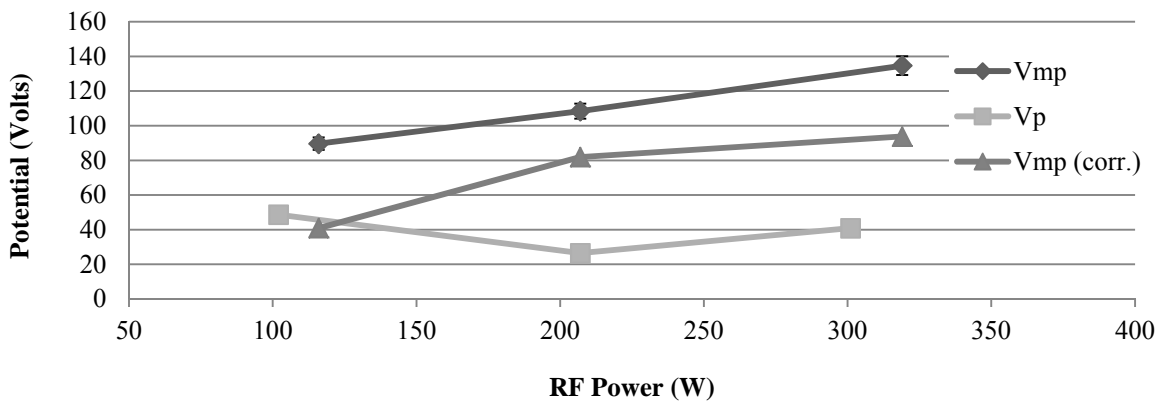


Figure 6.22: Most Probable Voltage (corrected) recorded at a distance of 16 mm from the exit plane for 2 sccm argon volumetric flow rate and 340 G magnetic field strength thruster operating conditions over an RF power range of 116 W – 319 W at the ‘low-pressure condition.’

Plasma potential determined using the emissive probe is recorded from 102 W to 505 W RF power. All Langmuir probe measurements are recorded across an RF power range of 100 W to 485 W. Plasma potential from the Langmuir probe varies wildly from 59 V at the 100 W operating condition to 150 V at the 485 W operating condition. This behavior however is repeated by the floating potential that increases from 38 V at the 100 W operating condition to 130 V at the 485 W operating condition as shown in Fig. 6.23.

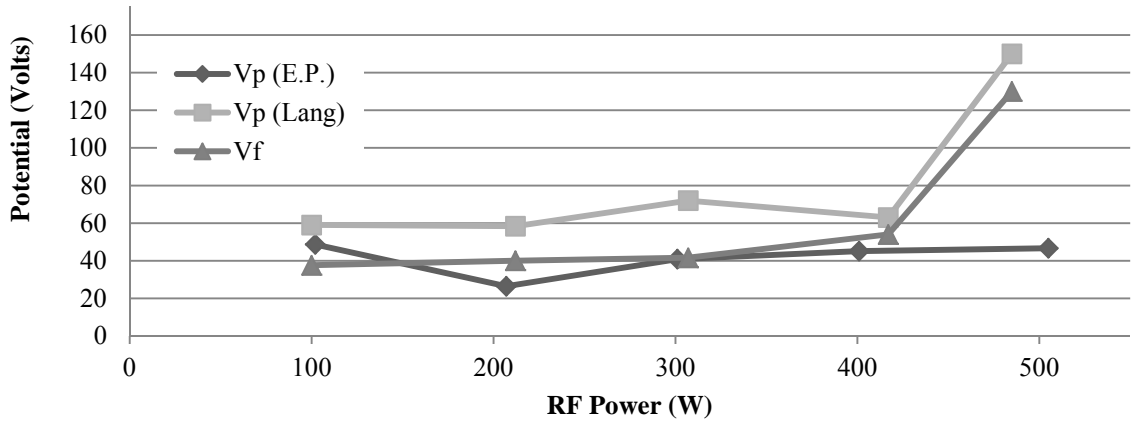


Figure 6.23: Potentials of interest recorded by the emissive probe (E.P.) and the Langmuir probe (L.P.) at the exit plane for 2 sccm argon volumetric flow rate and 340 G magnetic field strength thruster operating conditions over an RF power range of 100 W – 500 W at the ‘low-pressure condition.’

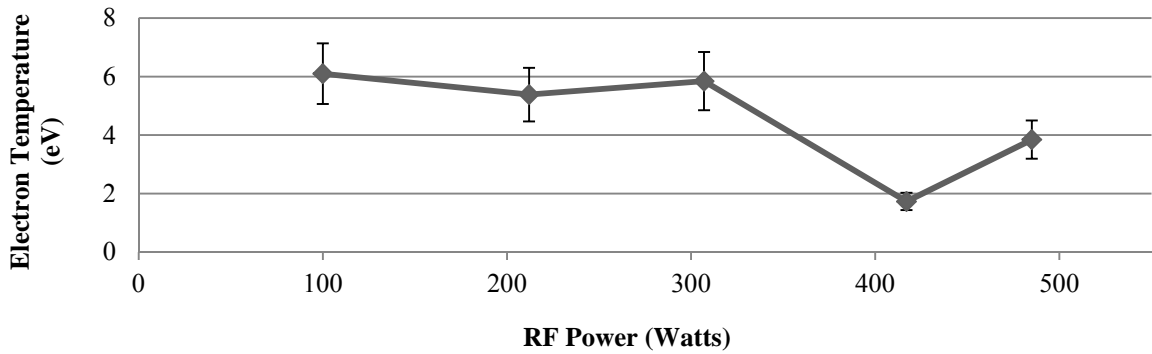


Figure 6.24: Electron temperatures recorded at the exit plane for 2 sccm argon volumetric flow rate and 340 G magnetic field strength thruster operating conditions over an RF power range of 100 W – 500 W at the ‘low-pressure condition.’

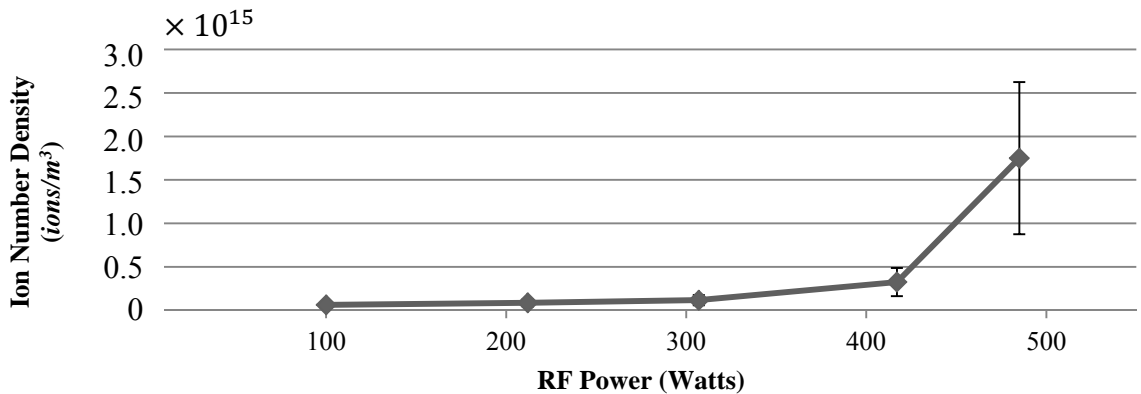


Figure 6.25: Ion number densities recorded at the exit plane for 2 sccm argon volumetric flow rate and 340 G magnetic field strength thruster operating conditions over an RF power range of 100 W – 500 W at the ‘low-pressure condition.’

Electron temperature averages approximately 5.7 eV with a deviation of 0.4 eV up until 300 W after which electron temperature drops to 1.7 eV at the 417 W operating condition as shown in Fig. 6.24. Ion density shown in Fig. 6.25 remains relatively unchanged until the 417 W condition when it increases three times its density at 307 W RF power from $1.17 \times 10^{14} \text{ ions/m}^3$ to $3.25 \times 10^{14} \text{ ions/m}^3$ and almost 5.5 times from 417 W to 485 W RF power when ion number density increases to a final value of $1.75 \times 10^{15} \text{ ions/m}^3$.

6.2.3 Comparison of the Effect of Increasing RF Power on Neutral Ingestion Influence at Both Pressure Conditions

Direct comparison of most probable voltages in Fig. 6.26 shows that for both pressure cases, most probable voltage increases with increasing RF power through the 300 W condition. The ‘high-pressure condition’ however only increases 15 V over the 200 W increase achieving a maximum of 33 V uncorrected most probable voltage. The ‘low-pressure condition’ most probable voltage on the other hand increases three times that amount from 90 V to 135 V over the same 200 W increase. The corrected most probable voltage increases 16 V and 53 V over the 200 W increase for the ‘high-pressure and ‘low-pressure conditions,’ respectively. For all comparable RF powers, the ‘low-pressure condition’ corrected most probable voltages are 33 V to 70 V higher than the ‘high-pressure condition’ corrected most probable voltages including consideration of the possible second populations at the 200 W and 300 W operating conditions.

Examining electron temperatures shown in Fig. 6.27 shows that the ‘low-pressure condition’ temperatures remain relatively constant until the 300 W condition after which they hit a minimum of 1.7 eV. Increasing RF power at the ‘high-pressure condition’

minimally effects electron temperature with limited fluctuations of up to ± 0.5 eV across the full range of consideration.

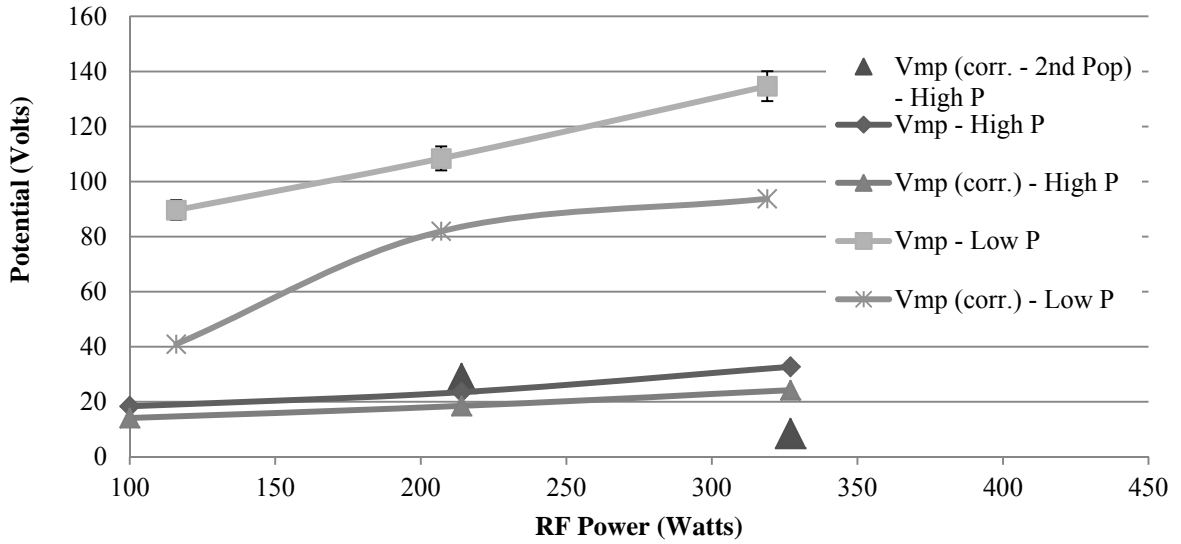


Figure 6.26: Most probable voltage (corrected) recorded for 2 sccm argon volumetric flow rate and 340 G magnetic field strength thruster operating conditions over a range of 100 W – 300 W RF power at both the ‘low-pressure condition’ (Low P) at a distance of 16 mm from the exit plane and ‘high-pressure condition’ (High P) on the exit plane.

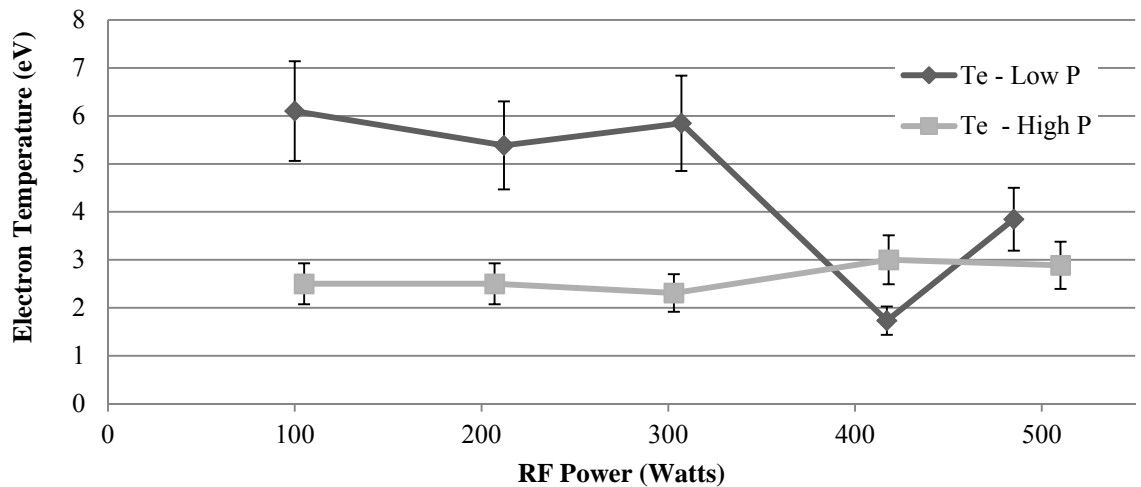


Figure 6.27: Electron temperatures recorded at the exit plane for 2 sccm argon volumetric flow rate and 340 G magnetic field strength thruster operating conditions over a range of 100 W – 500 W RF power at both the ‘low-pressure condition’ (Low P) and ‘high-pressure condition’ (High P).

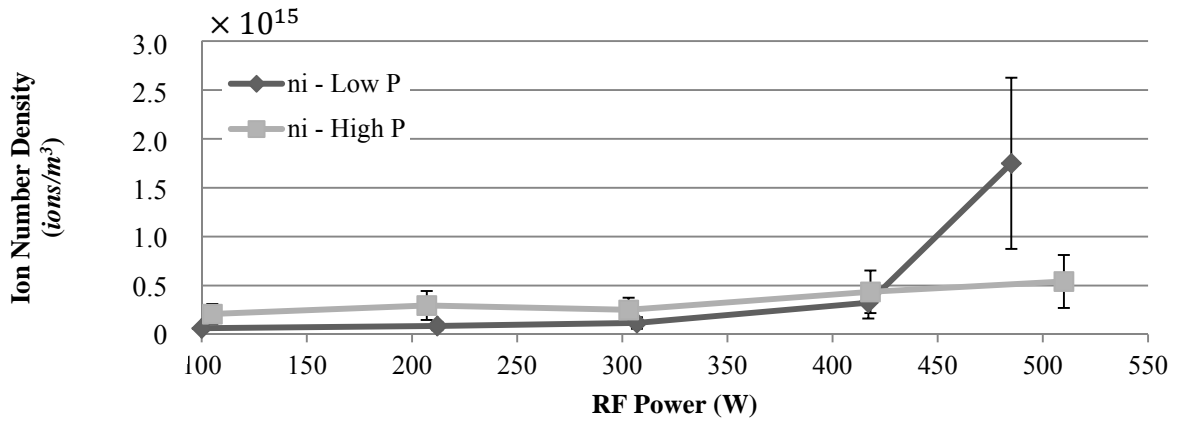


Figure 6.28: Ion number densities recorded at the exit plane for 2 sccm argon volumetric flow rate and 340 G magnetic field strength thruster operating conditions over a range of 100 W – 500 W RF power at both the ‘low-pressure condition’ (Low P) and ‘high-pressure condition’ (High P).

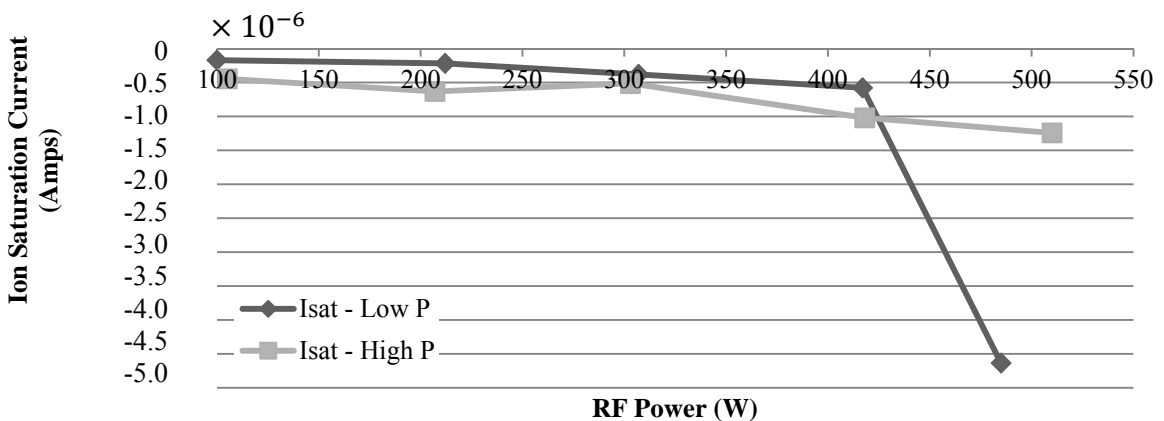


Figure 6.29: Ion saturation currents recorded at the exit plane for 2 sccm argon volumetric flow rate and 340 G magnetic field strength thruster operating conditions over a range of 100 W – 500 W RF power at both the ‘low-pressure condition’ (Low P) and ‘high-pressure condition’ (High P).

Ion number densities for the ‘high-pressure condition’ are always between 1×10^{14} to 2×10^{14} ions/m³ than the ‘low-pressure condition’ ion number densities for RF powers between 100 W to 400 W as shown in Fig. 6.28. Both sets of ion number density increase with increasing RF power. The 485 W operating condition at the ‘low-pressure condition’ however shows a steeper increase in plasma density from 3.2×10^{14} ions/m³

to 1.75×10^{14} ions/m³ that exceeds the 5.4×10^{14} ions/m³ ion number density of the ‘high-pressure condition’ at the 510 W RF power operating condition. This abrupt increase in ion number density is greatly influenced by the sharp increase in ion saturation current for the 485 W operating condition at the ‘low-pressure condition.’ Curve behavior for ion number density at both pressure conditions follows the trends exhibited by the affiliated ion saturation currents shown in Fig 6.29.

6.2.4 Effect of Increasing Magnetic Field Strength on Neutral Ingestion Influence at the ‘High-Pressure Condition’

The IEDFs for the ‘high-pressure condition’ for increasing magnetic field strengths in the source region are recorded for magnetic field strengths of 340 G to 700 G at the thruster exit plane for 2 sccm volumetric flow rate of argon and 116 W RF power. The IEDFs decrease in height as shown in Fig. 6.30.

Most probable voltages experience a minor increase of 8 V across the entire 360 G increase in magnetic field strength. Corrected most probable voltages for 340 G to 500 G magnetic field strength increase 7 V with increasing magnetic field strength as shown in Fig. 6.31. These negative potentials registered on the emissive probe are most likely due to negative-sheath effects during probe tip emission and will not be used for comparison in this work.³⁶

Plasma potential measured by the Langmuir probe increases to 22 V at the 400 G operating condition but then remains within ± 2.5 V of the final plasma potential value of 11.5 V at 700 G magnetic field strength as shown in Fig. 6.32. Floating potential remains within +2.5 V and – 5.5 V across the entire range of magnetic field strengths considered. Electron temperature displayed in Fig. 6.33 exhibits similar behavior to the plasma

potential measured by the Langmuir probe with a minimum of 1.5 eV at 600 G, a maximum of 5 eV at 400 G and staying within 1.5 eV to 3 eV for all magnetic strengths considered at 500 G and over.

Ion number density plotted in Fig. 6.34 stays in the $1.7 \times 10^{14} \text{ ions/m}^3$ to $2.7 \times 10^{14} \text{ ions/m}^3$ range across the entire magnetic field strength range except for the 400 G operating condition with a value of $7.5 \times 10^{13} \text{ ions/m}^3$. All conditions, except for the 400 G operating condition, may remain constant within the uncertainty of the ion number density analysis.

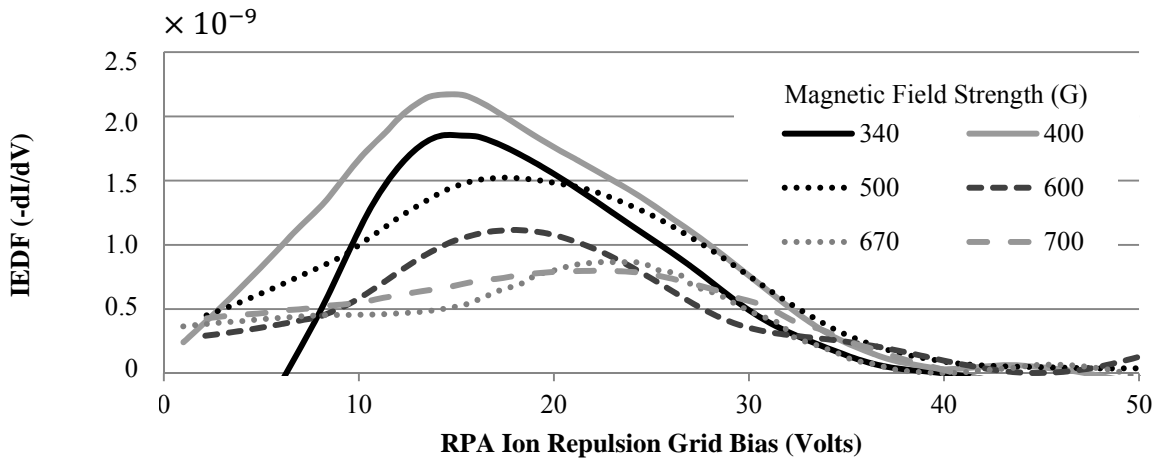


Figure 6.30: IEDF recorded at the exit plane for 2 sccm argon volumetric flow rate and 116 W RF power operating conditions over a range of 340 G – 700 G magnetic field strength at the ‘high-pressure condition.’

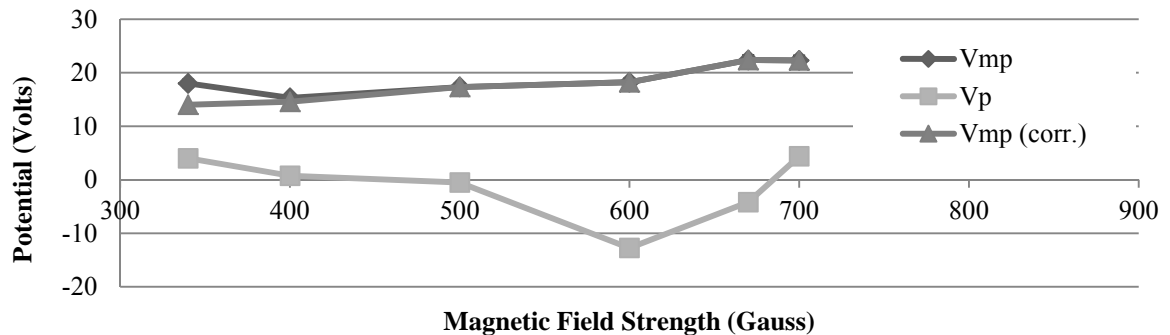


Figure 6.31: Most probable voltage (corrected) recorded at the exit plane for 2 sccm argon volumetric flow rate and 116 W RF power operating conditions over a range of 340 G – 700 G magnetic field strength at the ‘high-pressure condition.’

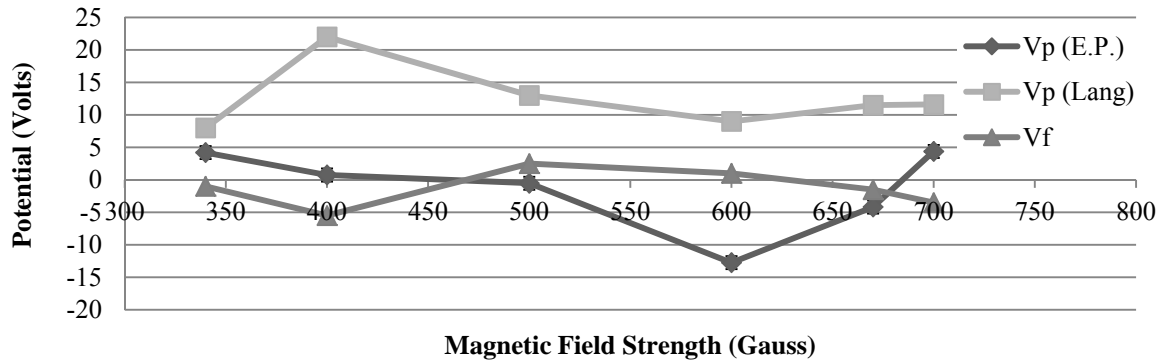


Figure 6.32: Potentials of interest recorded by the emissive probe (E.P.) and the Langmuir probe (L.P.) at the exit plane for 2 sccm argon volumetric flow rate and 100 W RF power operating conditions over a range of 340 G – 700 G magnetic field strength at the ‘high-pressure condition.’

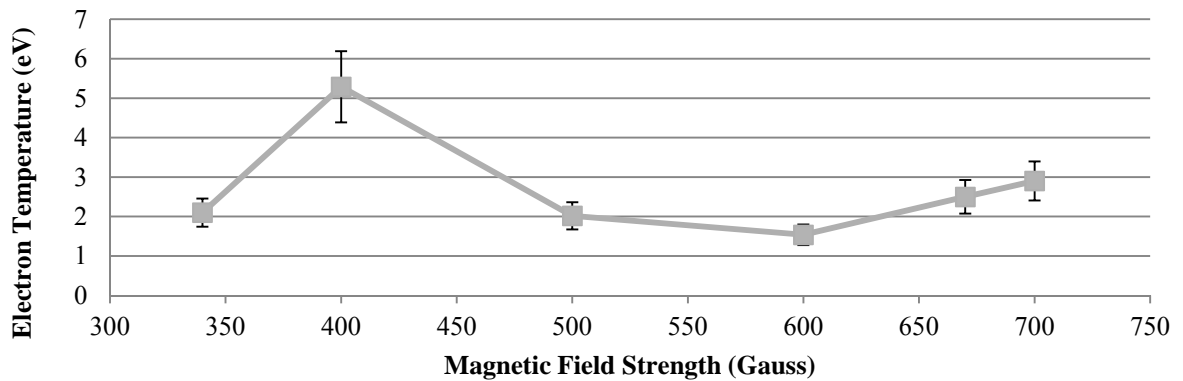


Figure 6.33: Electron temperatures recorded at the exit plane for 2 sccm argon volumetric flow rate and 116 W RF power operating conditions over a range of 340 G – 700 G magnetic field strength at the ‘high-pressure condition.’

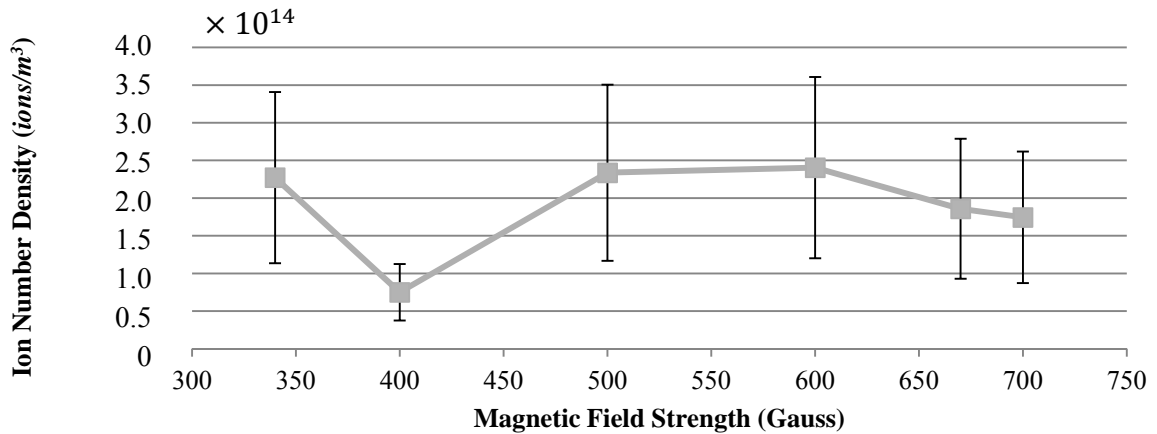


Figure 6.34: Ion number densities recorded at the exit plane for 2 sccm argon volumetric flow rate and 116 W RF power operating conditions over a range of 340 G – 700 G magnetic field strength at the ‘high-pressure condition.’

6.2.5 Effect of Increasing Magnetic Field Strength on Neutral Ingestion Influence at the ‘Low-Pressure Condition’

The IEDFs for 2 sccm argon and 100 W RF power are plotted for increasing source region magnetic field strength from 340 G to 700 G at a distance of 56 mm from the exit plane for the ‘low-pressure condition.’ Distributions drop in height as shown in Fig. 6.35 while the most probable voltage stays between 82 V and 89 V as shown in Fig. 6.36. The plasma potential measured by the emissive probe drops 26 V between the 340 G and the 400 G operating condition after which it remains between 19 V and 23 V. In turn, the corrected most probable voltage increases 25 V between the 340 G and the 400 G operating condition and then remains between 58 V to 69 V up to 600 G operating condition.

Langmuir probe measurements are recorded at the exit plane for the first three magnetic field strengths under consideration. Plasma potential measured using the Langmuir probe decreases steadily from 65 V to 51 V at the 500 G operating condition. The floating voltage stays within 33 – 42 V across the full magnetic field range of interest as shown in Fig 6.37.

Plasma potential drops between the 340 G and 400 G operating conditions and rises back up by the 500 G operating condition for both sets of probe data. Electron temperature calculated using the Langmuir probe stays between 5.6 eV and 3.2 eV across the 160 G increase illustrated in Fig. 6.38. Ion densities for the exit plane of the Helicon ion thruster change marginally over the 160 G range of consideration with a maximum of $5.8 \times 10^{13} \text{ ions/m}^3$ and a minimum of $4.7 \times 10^{13} \text{ ions/m}^3$ as shown in Fig. 6.39. Ion number density may be constant within the uncertainty of the analysis.

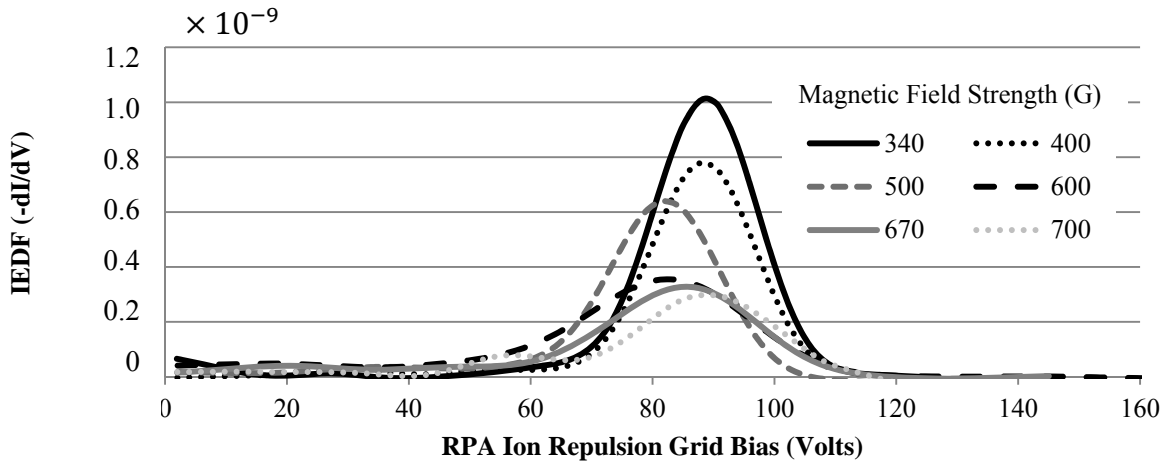


Figure 6.35: IEDF recorded 56 mm downstream from the exit plane for 2 sccm argon volumetric flow rate and 116 W RF power operating conditions over a range of 340 G – 700 G magnetic field strength at the ‘low-pressure condition.’

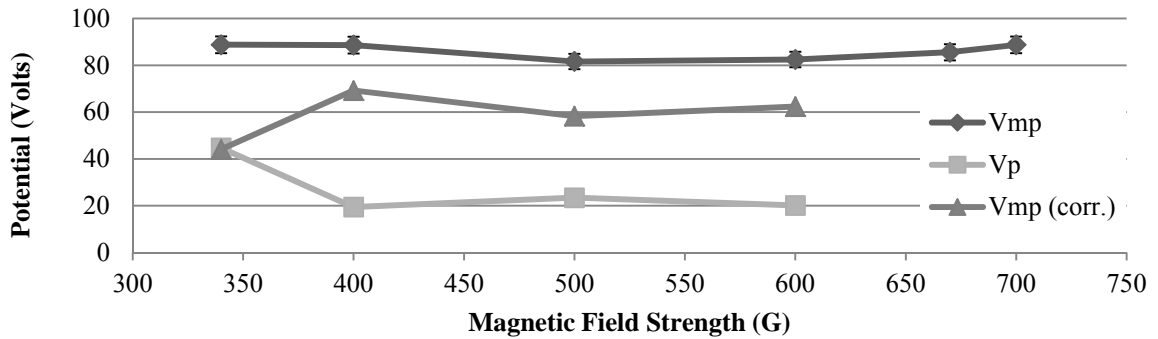


Figure 6.36: Most probable voltages (corrected) recorded 56 mm downstream from the exit plane for 2 sccm argon volumetric flow rate and 116 W RF power operating conditions over a range of 340 G – 700 G magnetic field strength at the ‘low-pressure condition.’

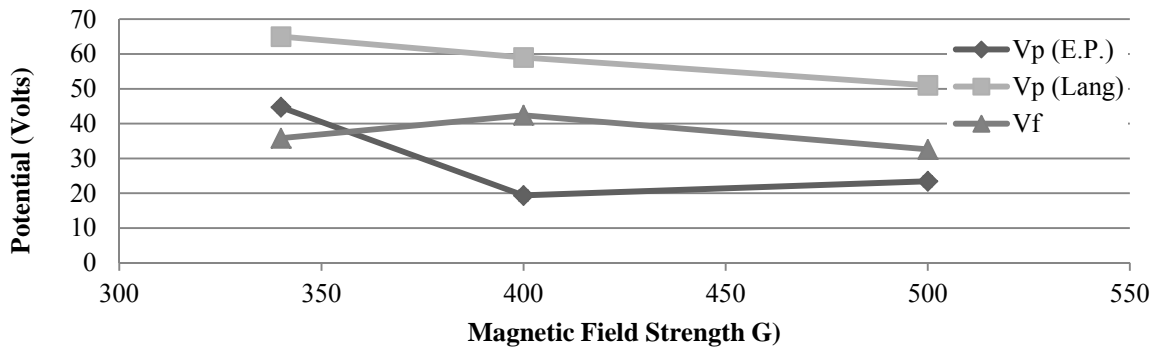


Figure 6.37: Potentials of interest recorded by the Langmuir probe (L.P.) and emissive probe (E.P.) at the exit plane for 2 sccm argon volumetric flow rate and 100 W RF power operating conditions over a range of 340 G – 500 G magnetic field strength at the ‘low-pressure condition.’

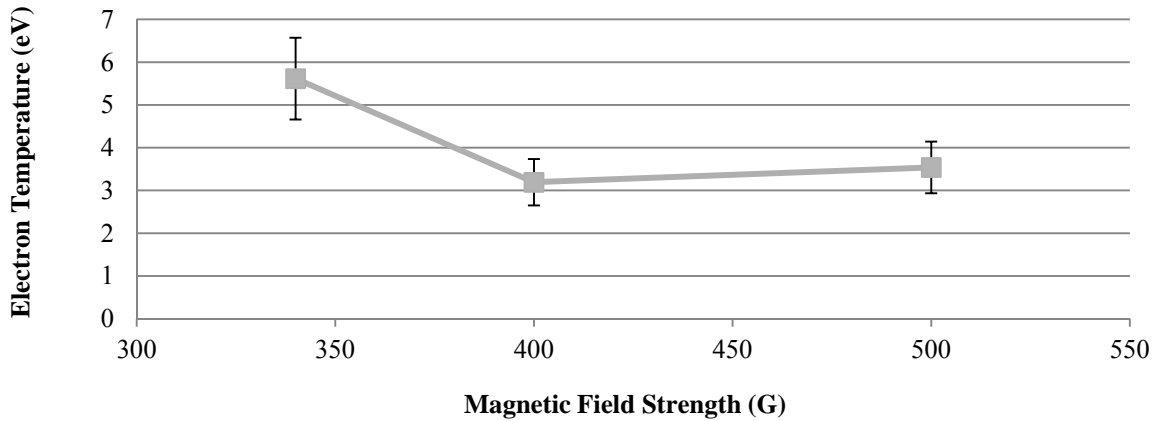


Figure 6.38: Electron temperatures recorded at the exit plane for 2 sccm argon volumetric flow rate and 100 W RF power operating conditions over a range of 340 G – 500 G magnetic field strength at the ‘low-pressure condition.’

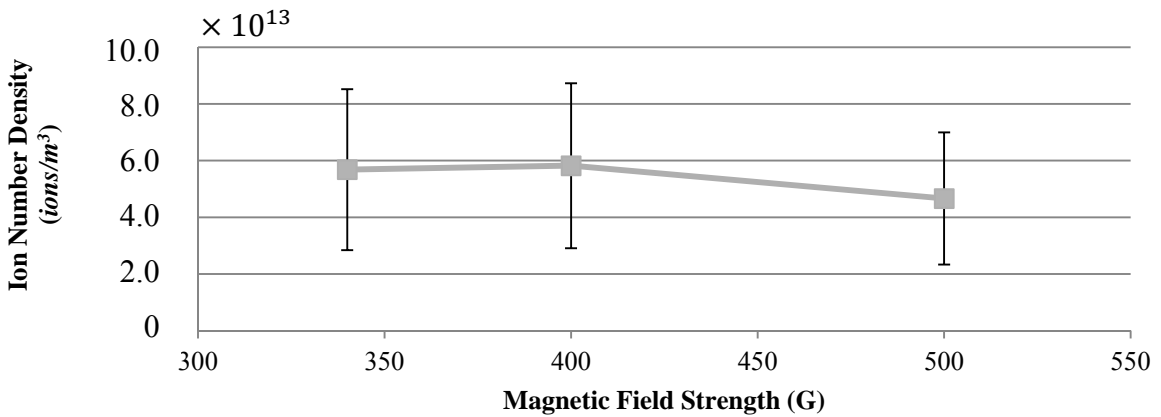


Figure 6.39: Ion number densities recorded at the exit plane for 2 sccm argon volumetric flow rate and 100 W RF power operating conditions over a range of 340 G – 500 G magnetic field strength at the ‘low-pressure condition.’

6.2.6 Comparison of the Effect of Increasing Magnetic Field Strength on Neutral Ingestion Influence at Both Pressure Conditions

Uncorrected most probable voltages deviate only 8 V from the 340 G operating condition across the entire range of magnetic field strengths considered for both pressure conditions as illustrated in Fig. 6.40. Corrected most probable voltage for the ‘low-pressure condition’ is always a minimum of 31 V higher than the corrected most probable voltage for the ‘high-pressure condition.’

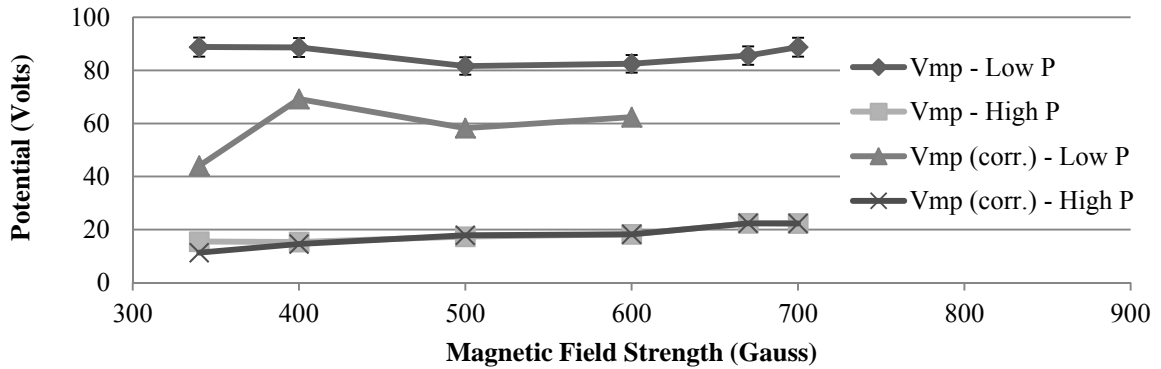


Figure 6.40: Most probable voltage (corrected) recorded for 2 sccm argon volumetric flow rate and 100 W RF power thruster operating conditions over a range of 340 G – 700 G magnetic field strength at both the ‘low-pressure condition’ (Low P) at a distance of 56 mm from the exit plane and the ‘high-pressure condition’ (High P) on the exit plane.

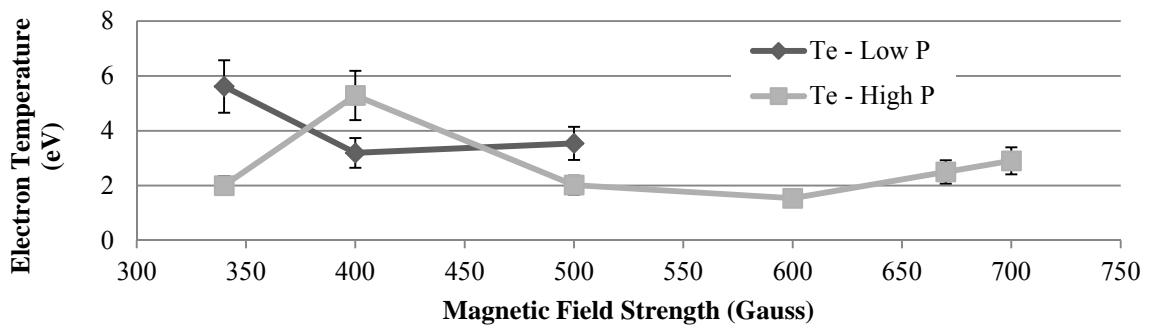


Figure 6.41: Electron temperatures recorded at the exit plane for 2 sccm argon volumetric flow rate and 100 W RF power thruster operating conditions over a range of 340 G – 700 G magnetic field strength at both the ‘low-pressure condition’ (Low P) and the ‘high-pressure condition’ (High P).

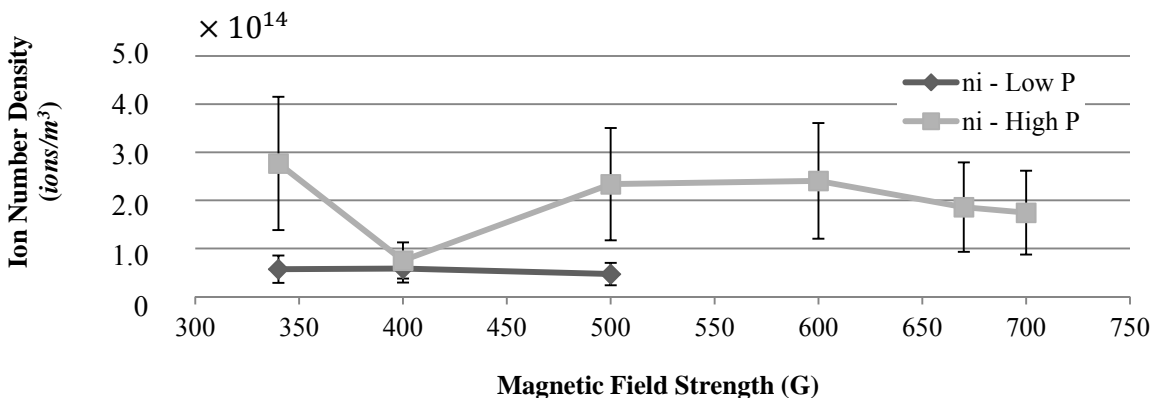


Figure 6.42: Ion number densities recorded at the exit plane for 2 sccm argon volumetric flow rate and 100 W RF power thruster operating conditions over a range of 340 G – 700 G magnetic field strength at both the ‘low-pressure condition’ (Low P) and the ‘high-pressure condition’ (High P).

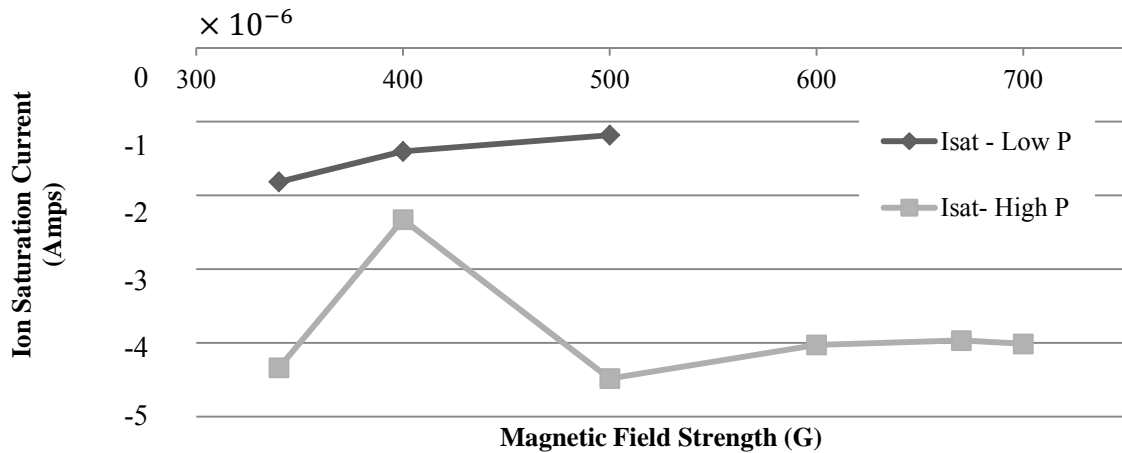


Figure 6.43: Ion saturation currents recorded at the exit plane for 2 sccm argon volumetric flow rate and 100 W RF power thruster operating conditions over a range of 340 G – 700 G magnetic field strength at both the ‘low-pressure condition’ (Low P) and the ‘high-pressure condition’ (High P).

Electron temperature displayed in Fig. 6.41 does not exhibit any distinctive behavior between the two pressure cases unless the 400 G operating condition is excluded. Excluding the 400 G case allows for the assertion that the electron temperature is always higher for the ‘low-pressure condition’ for the additional three magnetic field strengths considered. Ignoring the 400 G operating condition in Fig. 6.42 permits the generalization that ion number density is always higher for the ‘high-pressure condition’ which agrees with the ion saturation currents collected and shown in Fig. 6.43. Ignoring the 400 G operating condition again allows the assertion that ion number density and ion saturation currents change minimally over the full range of magnetic field strengths considered for both pressure conditions. Unaccounted probe errors are thought to have occurred during data collection at the 400 G operating condition making Langmuir probe data collected at that condition unreliable.

6.3 The Effects of Increased Volumetric Flow Rate at the ‘Low-Pressure Condition’ Compared to the Effects of Neutral Ingestion at the ‘High-Pressure Condition’

After establishing the differences in plasma properties due to neutral ingestion in the previous two sections, this portion of the study estimates the magnitude of the plasma property changes due to increased flow rate. Plasma properties are measured over an argon volumetric flowrate of 1.3 sccm to 60 sccm at the ‘low-pressure condition.’ For all trials, a source region magnetic field strength of 340 G is maintained with an RF power level of ~ 100 W. Properties considered include plasma potential, floating potential, the most probable voltage of the IEDF, electron temperature, ion number density, and ion saturation current. Measurements are recorded on the thruster centerline at the exit plane.

6.3.1 Results

The IEDFs shown in Fig. 6.44 shift to lower uncorrected most probable voltages when volumetric flowrate increases from 1.3 sccm to 30 sccm argon. The greatest drop in V/sccm occurs between the 1.3 sccm and 2 sccm cases at a rate of 37 V/sccm. The next largest rate of decrease in most probable voltage occurs between the 2 sccm and 4 sccm cases at a rate of 6 V/sccm. After 30 sccm, the rate of change in most probable voltage is less than 1 V/sccm while the distributions drop in height. Corrected most probable voltage stays between 29 V and 39 V for all operating conditions with the exception of the 4 sccm operating condition at 52 V as shown in Fig. 6.45. Plasma potentials measured by the emissive probe at 40 sccm and above are negative due to sheath effects at the emissive probe tip preventing accurate measurement.³⁶ Most probable voltages are not corrected for flow rates above 40 sccm.

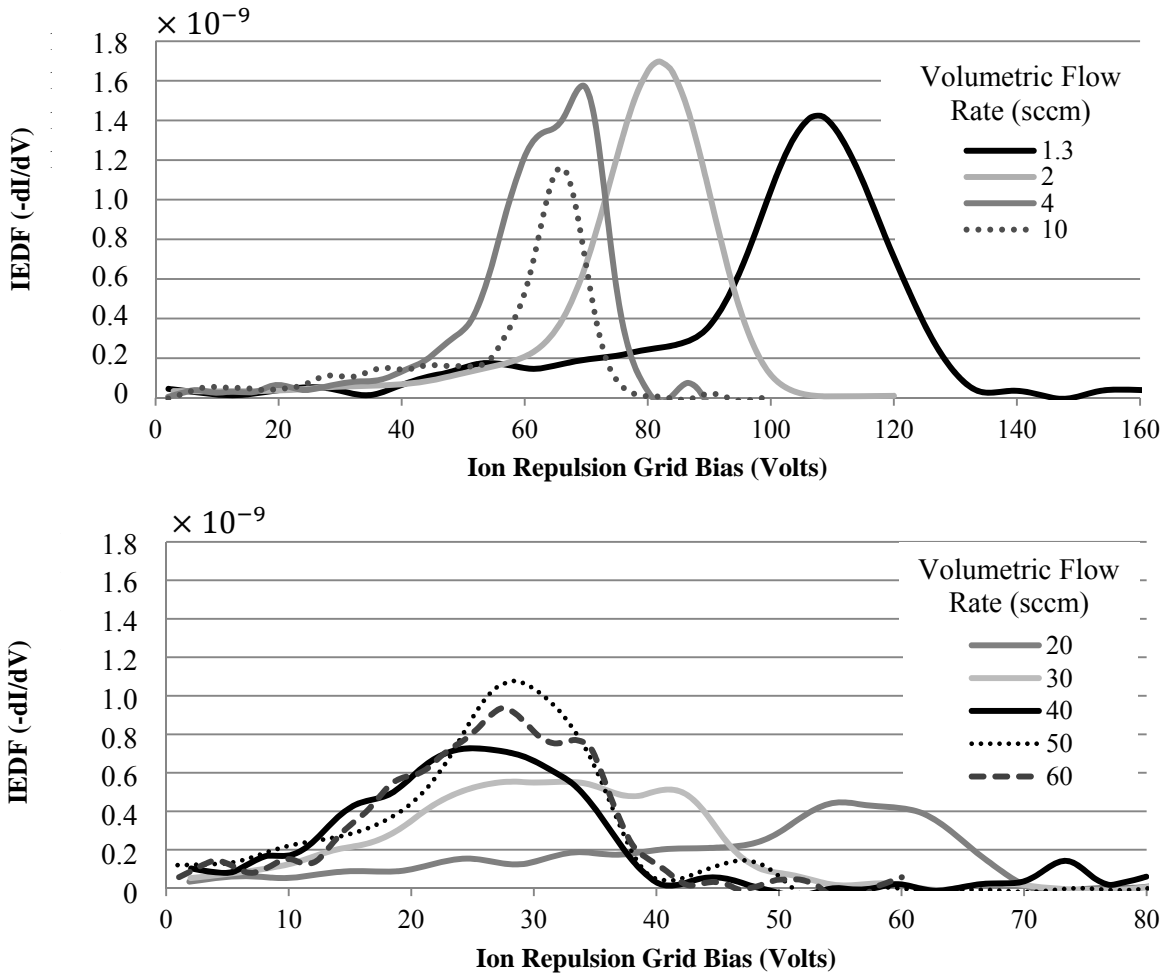


Figure 6.44: IEDF recorded at the exit plane for 100 W RF power and 340 G source region magnetic field strength operating conditions over a range of 1.3 – 10 sccm argon volumetric flow rate (Top) and over a range of 20 – 60 sccm argon volumetric flow rate (Bottom) at the ‘low-pressure condition.’

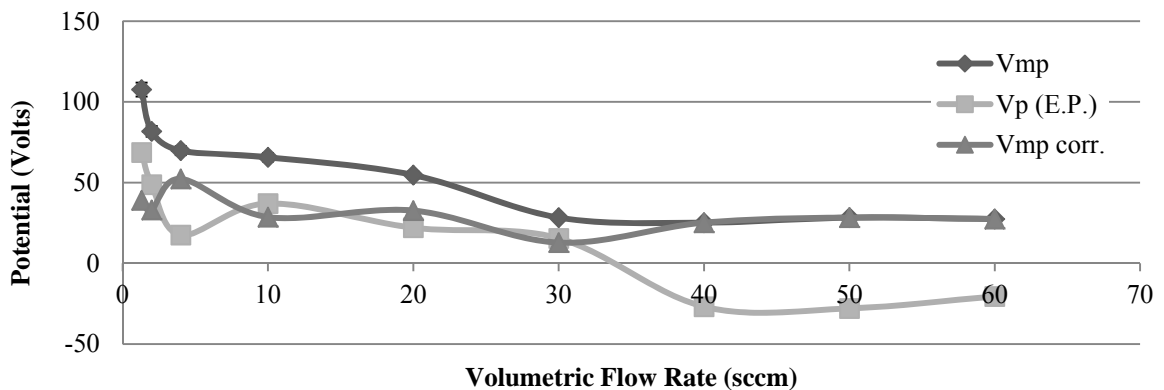


Figure 6.45: Most probable voltage (corrected) recorded at the exit plane for 100 W RF power and 340 G source region magnetic field strength operating conditions over a range of 1.3 – 60 sccm argon volumetric flow rate at the ‘low-pressure condition.’

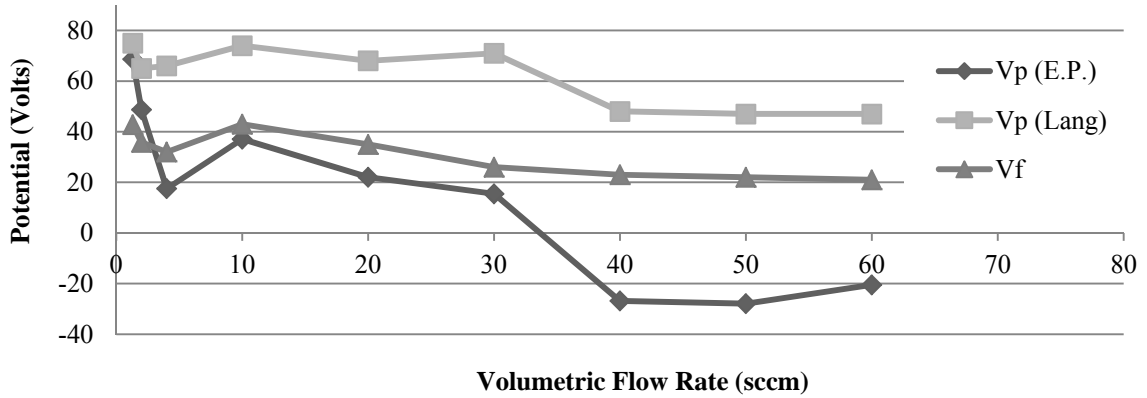


Figure 6.46: Potentials of interest recorded by the Langmuir probe (L.P.) and the emissive probe (E.P.) at the exit plane for 100 W RF power and 340 G source region magnetic field strength operating conditions over a range of 1.3 – 60 sccm argon volumetric flow rate at the ‘low-pressure condition.’

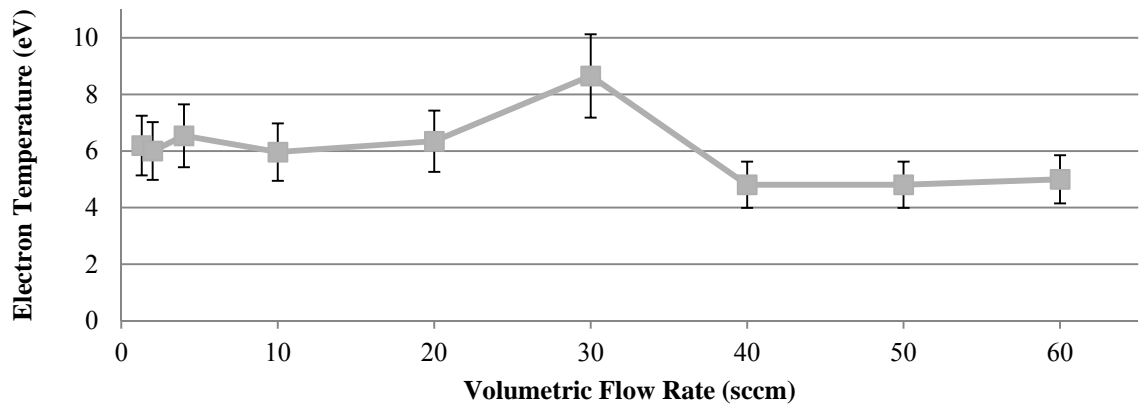


Figure 6.47: Electron temperatures recorded at the exit plane for 100 W RF power and 340 G source region magnetic field strength operating conditions over a range of 1.3 – 60 sccm argon volumetric flow rate at the ‘low-pressure condition.’

Plasma potential measured by the Langmuir probe follows a similar pattern as the plasma potential measured using the emissive probe, decreasing and then increasing in voltage. Plasma potential measured by the Langmuir probe oscillates within the voltage range of 65 V to 75 V for flow rates at or below 30 sccm as displayed in Fig. 6.46. For flow rates between 40 sccm and 60 sccm, plasma potential measured using the Langmuir probe stays at approximately 47 V to 48 V. Floating potential deviates up to 10 V from 42 V at the 1.3 sccm operating condition in the first few conditions but returns to 43 V

for the 10 sccm operating condition after which floating potential asymptotically approaches 20 V with increasing argon volumetric flow rate.

Electron temperature displayed in Fig. 6.47 shifts between 6 eV and 8.6 eV for flow rates of 30 sccm or less. Electron temperature may remain constant from 1.3 sccm to 20 sccm and from 40 sccm to 60 sccm when accounting for analysis uncertainty. Ion number density is a maximum at the 10 sccm operating condition with a value of 4.6×10^{14} ions/m³ as shown in Fig 6.48. Above 10 sccm, ion number density asymptotically approaches a final value of 1.2×10^{14} ions/m³ at 60 sccm. This behavior is governed by the ion saturation trends observed in Fig. 6.49.

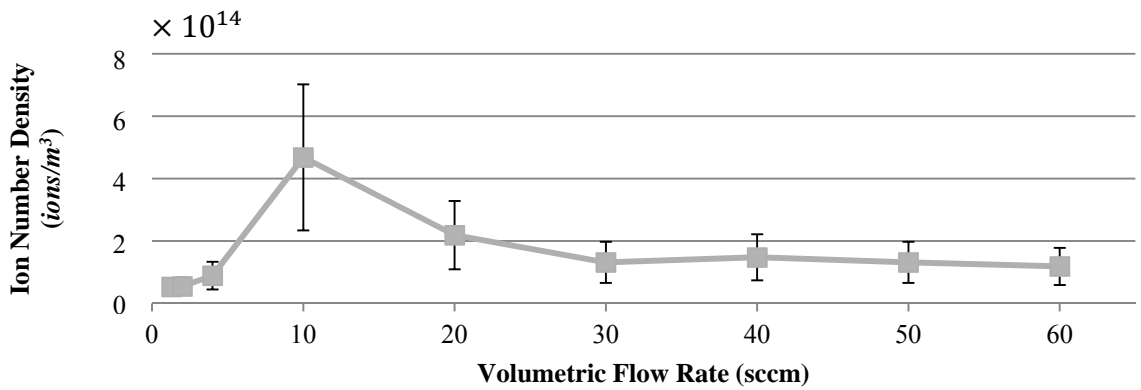


Figure 6.48: Ion number densities recorded at the exit plane for 100 W RF power and 340 G source region magnetic field strength operating conditions over a range of 1.3 – 60 sccm argon volumetric flow rate at the ‘low-pressure condition.’

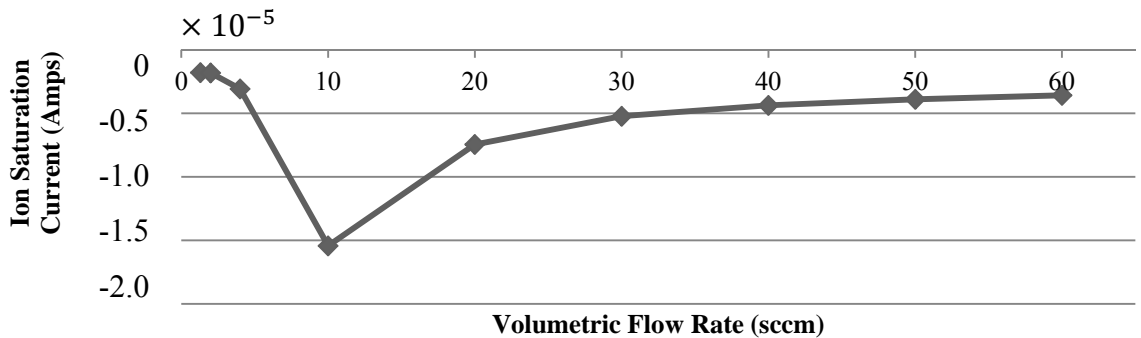


Figure 6.49: Ion saturation currents recorded at the exit plane for 100 W RF power and 340 G source region magnetic field strength operating conditions over a range of 1.3 – 60 sccm argon volumetric flow rate at the ‘low-pressure condition.’

6.4 Neutral Ingestion Effects on Double Layer Formation and RF Coupling Mode Transitions

All conditions previously discussed are examined for evidence of the presence of a Double Layer or a transition in RF coupling modes. Once a performance metric is identified, the corresponding condition at the other operating pressure is examined to see if the same performance metric is present. Existence of a Double Layer acceleration mechanism is determined by a persistent, double-peaked IEDF. An RF coupling mode transition occurs at a discontinuous jump in ion number density.

6.4.1 Double Layer

After considering all available data, two cases exhibit possible Double Layer behavior. The first considered here is the 214 W RF power, 2 sccm volumetric flow rate, and 340 G magnetic field strength operating condition at the ‘high-pressure conditions.’ Fig. 6.17 is repeated below in which a double peaked IEDF is evident for the third trial at the 214 W operating condition but appears as a wider, less distinct distribution for the seventh trial. A comparison of the IEDF profile at the 214 W ‘high-pressure condition’ with the 207 W IEDF at the ‘low-pressure condition’ is shown in Fig. 6.59. The ‘high-pressure condition’ has populations of corrected most probable voltages at 18.5 V and 28.5 V. The ‘low-pressure condition’ does not exhibit double peaked behavior indicative of a Double Layer with only one corrected most probable voltage of 82 V.

Another possible Double Layer occurs at the 327 W RF power, 2 sccm volumetric flow rate, and 340 G magnetic field strength operating condition at the ‘high-pressure condition.’ A shallow double-peaked profile is generated with corrected most probable

voltages of 8 V and 28 V. The ‘low-pressure condition’ does not exhibit double-peaked behavior and has only one corrected most probable voltage at 94 V. Profiles in both Fig. 6.50 and 6.51 for the ‘high-pressure condition’ show shallow peaks close together without distinct separation of distributions of the ion populations at each voltage.

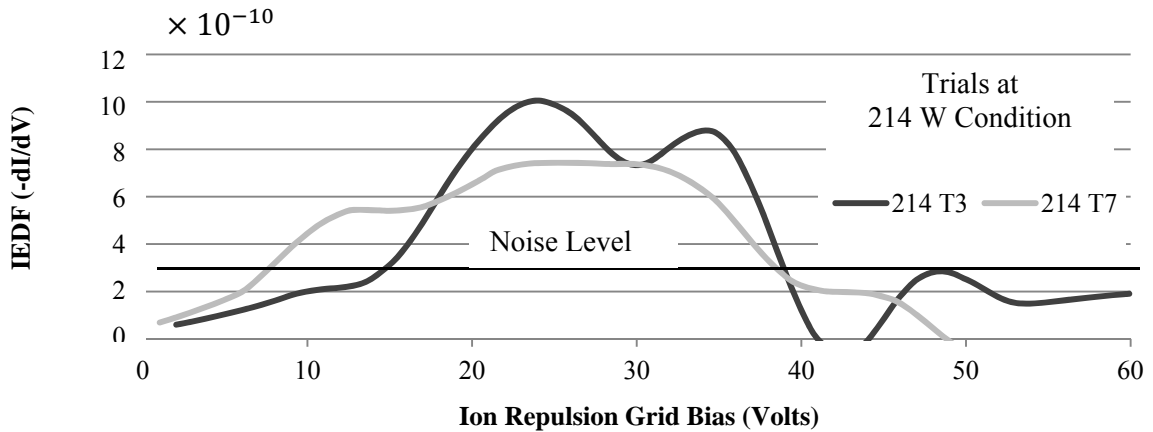


Figure 6.17: IEDFs for Trials 3 (T3) and 7 (T7) recorded at the exit plane for 2 sccm argon volumetric flow rate, 214 W RF power, and 340 G magnetic field strength thruster operating condition at the ‘high-pressure condition.’

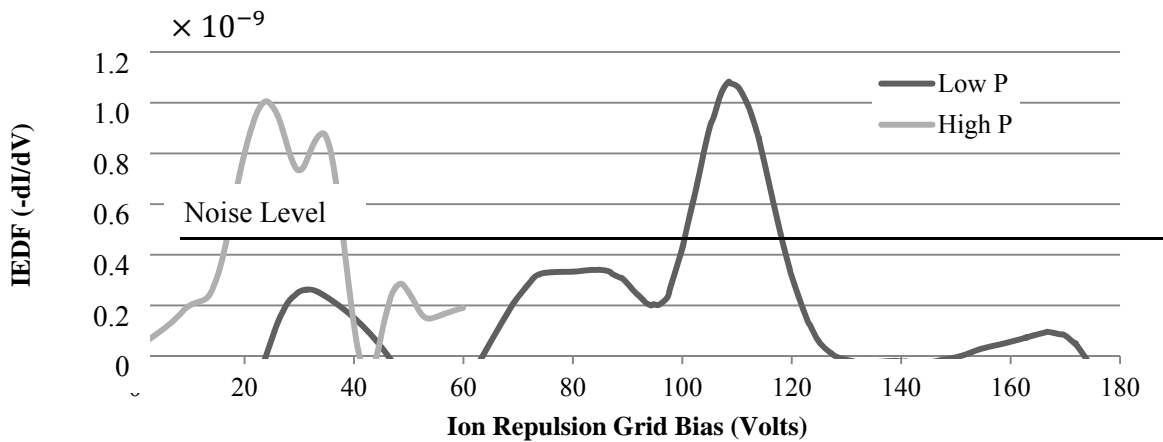


Figure 6.50: IEDFs recorded at 2 sccm argon volumetric flow rate, 200 W RF power, and 340 G magnetic field strength thruster operating condition at the exit plane for the ‘high-pressure condition’ (High P) and 16 mm downstream of the exit plane for the ‘low-pressure condition’ (Low P).

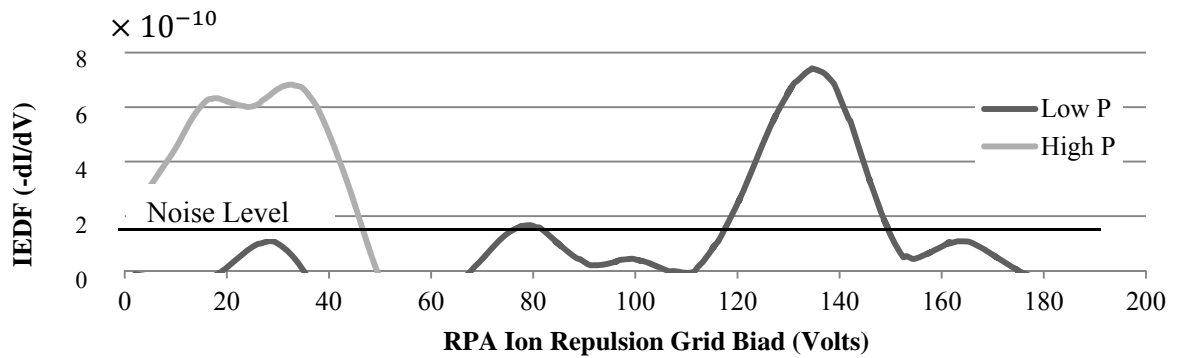


Figure 6.51: IEDFs recorded at 2 sccm argon volumetric flow rate, 300 W RF power, and 340 G magnetic field strength thruster operating condition at the exit plane for the ‘high-pressure condition’ (High P) and 16 mm downstream of the exit plane for the ‘low-pressure condition’ (Low P).

6.4.2 RF Coupling Modes

Ion number density figures were examined for the presence of an RF coupling mode transition in which a discontinuous increase in ion number density occurs. Fig. 6.28 repeated here shows a sharp increase in ion number density for the 485 W RF power, 2 sccm volumetric flow rate, and 340 G magnetic field strength operating condition for the ‘low-pressure condition.’ Ion number density increases from 3.2×10^{14} ions/m³ to 1.7×10^{15} ions/m³ for the ‘low-pressure condition.’ Ion number density for the high-pressure condition does not exhibit this behavior remaining in the 10^{14} ions/m³ range across the full RF power range considered.

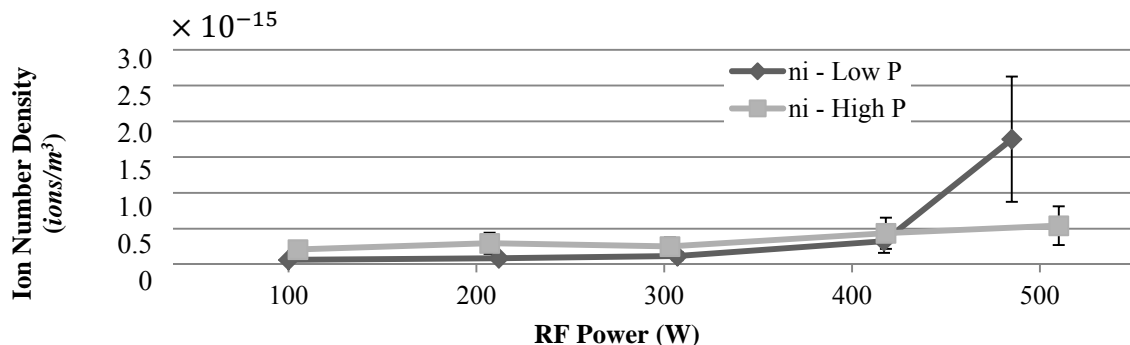


Figure 6.28: Ion number densities recorded at the exit plane for 2 sccm argon volumetric flow rate and 340 G magnetic field strength thruster operating conditions over a range of 100 W – 500 W RF power at both the ‘low-pressure condition’ (Low P) and ‘high-pressure condition’ (High P).

CHAPTER VII

ANALYSIS

7.1 Effects of Neutral Ingestion on Plasma Properties

Section 6.1.3 compared the most probable voltage of the IEDF, electron temperature, plasma potential, and ion number density between the ‘high-pressure condition’ and ‘low-pressure condition.’ Values were recorded for MadHeX Replica operation on 2 sccm argon volumetric flow rate, 100 W RF power, and 340 G magnetic field strength along the thruster centerline from 79 mm upstream of the exit plane up to 216 mm downstream of the thruster exit plane. Using this data, changes in plume behavior and plasma properties are compared to determine the effect of neutral ingestion on Helicon ion thruster operation and the physical mechanisms driving those changes.

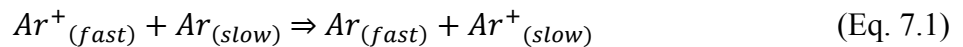
7.1.1 Ion-Neutral Collisions

In comparing the plasma properties for both pressure conditions, clear differences between the accelerated ion populations exist. Most probable voltages at the ‘high-pressure condition’ decrease along the thruster axis. This behavior is in contrast to the increasing most probable voltages observed while operating at the ‘low-pressure condition’ as shown in Fig. 6.11. Trends at the ‘high-pressure condition’ indicate energy losses in the IEDFs not observed at the ‘low-pressure condition.’ The accelerated ion population at the ‘low-pressure condition’ gains energy as ions accelerate along the thruster main axis resulting in increasing most probable voltages correlating with

increasing distance from the source region. Accelerated ions at the ‘high-pressure condition’ lose energy along the thruster axis most likely due to an increased collision rate near the thruster exit plane.

Collisions concerning the accelerated ion population result in energy exchanges that can lead to distribution broadening or, as observed at the ‘high-pressure condition,’ an overall reduction in ion energy. Since physical boundaries of the experimental setup are maintained between both pressure conditions, the cause for this loss in accelerated ion energy at the ‘high-pressure condition’ is thought to be collisions between the accelerated ions and ingested neutrals in the thruster plume. Two primary collision types are suspected to cause the reduction in ion energy: charge exchange collisions and momentum exchange collisions.

Charge exchange collisions are prevalent both close to and downstream of the thruster exit plane. Charge exchange collisions occur when a fast ion from the thruster ion beam collides with a slow moving neutral atom that has traveled into the exhaust plume. This interaction results in the formation of a slow ion and a fast neutral atom as shown in equation 7.1.⁵ Newly formed ions resulting from charge exchange collisions may not yet gain directionality at the time of measurement prior to becoming accelerated by the potential drop in the thruster plume and may not show up as a secondary ion population on the IEDF.



Charge exchange collisions in a Helicon ion thruster result in a reduction of ion energy.⁵ This type of ion energy loss mechanism is more pervasive in a Helicon ion thruster, as compared to other EP devices, due to the diffuse nature of the Helicon ion beam. In a HET, most ion-neutral collisions occur at the edges of the ion beam protecting the core from neutral ingestion effects.⁵ The IEDFs exhibiting decreasing most probable voltages for the Helicon ion thruster are recorded along the thruster centerline, showing that neutral ingestion occurs throughout the entire thruster plume structure.

Momentum exchange collisions also occur near the thruster exit plane resulting in a transfer of energy from the accelerated high-energy ions to any species with which the ions collide. Collisions of particular interest are those between the accelerated ions and the ingested argon neutral atoms as the ingested argon population at the ‘high-pressure condition’ is four times greater than the ingested argon population at the ‘low-pressure condition’ as shown in Table 7.1.

Table 7.1: Comparison of argon neutral ingestion rates for both the ‘Low-Pressure Condition’ and ‘High-Pressure Condition’ at 2 sccm argon volumetric flow rate, 100 W RF power, and 340 G magnetic field strength thruster operation.

| Property | ‘Low-Pressure Condition’ | ‘High-Pressure Condition’ |
|----------------|---------------------------|---------------------------|
| P_{argon} | 1.4×10^{-5} Torr | 6.6×10^{-5} Torr |
| $Q_{ingested}$ | 0.8 sccm argon | 3.8 sccm argon |

A comparison of the mean free paths, calculated using Eq. 7.4, of the ions with environmental neutrals from the ‘high-pressure condition’ with the mean free paths of the ions with environmental neutrals from the ‘low-pressure condition’ is shown in Table 7.2. An additional analysis of collision frequencies at the ‘high-pressure condition’ is also

conducted using Eq. 7.2 and shown in Table 7.3. Collision frequency (ν) is a function of the ion beam velocity (\bar{v}_{beam}) calculated using Eq. 7.3 and mean free path (λ). Mean free path is a function of the neutral number density (n_n) calculated using Eq. 7.5 and the collisional cross-section (σ) of interest. For charge transfer collisions between argon ions and argon neutrals, $\sigma = 7 \times 10^{19} m^2$ for ion energies up to 100 eV.³⁷ For momentum transfer collisions between argon ions and argon neutrals, $\sigma = 1 \times 10^{18} m^2$.³⁷ Neutral number density is a function of the partial pressure of argon (P_{argon}) and the neutral temperature (T) assumed to be 298 K.

$$\nu = \frac{\bar{v}_{beam}}{\lambda} \quad (\text{Eq. 7.2})^1$$

$$\bar{v}_{beam} = \sqrt{\frac{2e(V_{mp}-V_p)}{m_{argon}}} \quad (\text{Eq. 7.3})^1$$

$$\lambda = \frac{1}{n_n \langle \sigma \rangle} \quad (\text{Eq. 7.4})^{24}$$

$$n_n = \frac{P_{argon}}{k_b T} \quad (\text{Eq. 7.5})^{24}$$

Table 7.2: Charge exchange collision mean free paths (λ_{CT}) and momentum transfer mean free paths (λ_{MT}) for both the ‘Low-Pressure Condition’ and ‘High-Pressure Condition’ at 2 sccm argon volumetric flow rate, 100 W RF power, and 340 G magnetic field strength thruster operation.

| Property | ‘Low-Pressure Condition’ | ‘High-Pressure Condition’ |
|----------------|------------------------------------|------------------------------------|
| n_n | 4.54×10^{17} atoms/ m^3 | 2.14×10^{18} atoms/ m^3 |
| λ_{CT} | 3.15 m | 0.67 m |
| λ_{MT} | 2.20 m | 0.47 m |

Table 7.3: Charge exchange collision frequencies (ν_{CT}) and momentum transfer collision frequencies (ν_{MT}) at the ‘High-Pressure Condition’ at 2 sccm argon volumetric flow rate, 100 W RF power, and 340 G magnetic field strength thruster operation.

| Distance from Exit Plane | 0 mm | 16 mm | 66 mm |
|--------------------------|---------------------|---------------------|---------------------|
| $\bar{v}_{beam}(m/s)$ | 8,267 m/s | 7,683 m/s | 6,622 m/s |
| ν_{CT} | 12,383 ($coll/s$) | 11,507 ($coll/s$) | 9,918 ($coll/s$) |
| ν_{MT} | 17,690 ($coll/s$) | 16,439 ($coll/s$) | 14,468 ($coll/s$) |

Examination of Table 7.2 reveals mean free path lengths at the ‘high-pressure condition’ on the same order of magnitude as the 60 cm long distance between the source region where ions are formed and the exit plane of the MadHeX Replica. Ions formed in the source region during operation at the ‘high-pressure condition,’ will start to lose energy due to momentum transfer collisions inside the discharge chamber. Soon after exiting the discharge chamber, charge exchange collisions will occur between accelerated ions and ingested argon neutrals resulting in additional energy losses for the accelerated ion population. Ions formed in the source region during operation at the ‘low-pressure

condition' however, will have on average traveled far beyond the 60 cm long discharge chamber length before experiencing either momentum or charge exchange collisions. This analysis supports the idea that collisions between the accelerated ion population and the ingested argon atoms are responsible for the observed reduction in ion energy (decreasing most probable voltage) observed during operation at the 'high-pressure condition.' A comparison of the collision frequencies between the momentum transfer and charge transfer collisions at the 'high-pressure condition' in Table 7.3 shows that momentum transfer collisions exceed charge exchange collisions across the axis length investigated.

7.1.2 Plume Ionization

While collisions explain the reduction in ion energy, they do not account for the overall increase in ion number density at the 'high-pressure condition' shown in Fig. 6.13. The increase in ion population is due to a second neutral-plume interaction as neutral ions traveling near the thruster exit undergo ionization due to collisions with hot plume electrons or electron excitation from the radio waves broadcast by the thruster antenna. These new ions result in an increase in ion population and represent a more direct augmentation to thrust as the newly formed ions are also free to undergo acceleration due to electric fields present in the thruster exhaust plume.⁵

Slow ion formation in the exhaust plume may exist at both pressure conditions but leads to a significantly higher ion number density at the 'high-pressure condition.' This assertion is tested by comparing the ion production rates at both pressure conditions calculated using Eq. 7.6 for ions formed via electron impact with plume neutrals. Electron number density (n_e) is assumed to be equal to the ion number density (n_i)

accounting for only singly-charged ions in the exhaust plume. Electron velocity (\bar{v}_e) is calculated with Eq. 7.7 using electron temperature and electron mass (m_e). The argon ionization cross section range is assumed constant at $\sigma_i = 1.6 \times 10^{-17} \text{ m}^2$.³⁸ The results are presented in Table 7.4.

$$\frac{dn_i}{dt} = n_e n_n \sigma_i \bar{v}_e \quad (\text{Eq. 7.6})^1$$

$$\bar{v}_e = \sqrt{\frac{2eT_e}{m_e}} \quad (\text{Eq. 7.7})$$

Table 7.4: Mean free path lengths and ion production rates for plume neutral ionization for both the ‘Low-Pressure Condition’ and ‘High-Pressure Condition’ at 2 sccm argon volumetric flow rate, 100 W RF power, and 340 G magnetic field strength thruster operation for plume neutral ionization.

| Property | ‘Low-Pressure Condition’ | | | ‘High-Pressure Condition’ | | |
|--|--------------------------|----------------------|----------------------|---------------------------|----------------------|----------------------|
| λ Ionization | 0.14 m | | | 0.03 m | | |
| Distance from Exit Plane | 0 mm | 16 mm | 66 mm | 0 mm | 16 mm | 66 mm |
| $\frac{dn_i}{dt}$ (ions/s·m ³) | 5.6×10^{20} | 5.3×10^{20} | 2.5×10^{20} | 6.7×10^{21} | 7.2×10^{21} | 9.4×10^{21} |

The mean free path length for the ‘low-pressure condition’ is 4.7 times longer than the plume neutral ionization mean free path length of the ‘high-pressure condition,’ a direct result of the higher neutral pressure corresponding to higher neutral argon ingestion flow rate. Higher neutral number density leads to the difference in magnitude between the ‘low-pressure condition’ ion production rates and the ‘high-pressure condition’ ion production rates. The high plume ionization rates produce the significantly greater ion

number densities observed at the ‘high-pressure condition.’ Higher ion number densities will also result in inflated thrust performance discussed in the following section.

7.1.3 Thrust Augmentation

In order to estimate the thrust generated at each pressure condition, three thrust contributors are of interest: thrust due to the accelerated ion beam, thrust due to electron pressure, and thrust generated by the acceleration of newly formed plume ions. The acceleration of the newly formed plume ions will capture the thrust contribution due to neutral ingestion in the thruster exhaust plume resulting in neutral ionization. Thrust augmentation due to ion-neutral collisions will be captured in the reduction of the corrected most probable voltage.

While charge exchange collisions cause a reduction in plume energy they ultimately result in an increase in thrust as the newly formed ions can still undergo acceleration in the plume due to continuing interaction with the thruster magnetic field. Total momentum transfer for a charge exchange pair is greater than that of an ion beam without charge exchange collisions resulting in greater thrust performance.⁵ This resulting performance inflation is especially powerful when the initial collision does not result in a momentum transfer between the fast ion and slow neutral atom. Newly formed ions due to plume ionization of neutral atoms also undergo acceleration in the plume contributing to increased thrust performance.

Estimating the magnitude of thrust performance unfortunately is not as simple as determining the sources responsible for changes in plasma properties and behavior between both pressure conditions. The mechanisms behind plasma detachment in magnetic nozzles are currently poorly understood although several theories exist.

Understanding detachment and the effect of the magnetic nozzle on the exhaust plume structure is necessary for evaluating propulsive performance of the nozzle.³⁹ Experimental evidence in ion detachment in Helicon Double Layer thrusters has found ion detachment to occur within a few centimeters from the thruster exit.⁴⁰ For these reasons, potential thrust values are calculated at an arbitrary distance of 66 mm downstream of the thruster exit plane in an effort to capture the effect of plume neutral contributions to thrust performance while remaining close to the thruster exit and expanding magnetic field lines of the magnetic nozzle.

In order to calculate the effect of plume neutral ingestion on thrust, three separate thrust contributions are calculated from Eq. 7.8.1: the thrust generated by the ion beam ($\overline{T_{iB}}$), the thrust due to electron pressure ($\overline{T_{eP}}$), and the thrust resulting from the acceleration of newly formed ions ($\overline{T_{iP}}$). From Eq. 2.4, thrust contributions can be calculated by multiplying the number density of the charged specie population with its affiliated temperature as illustrated in Eq. 7.8.2. Equation 7.8.3 is a fully expanded version of Eq. 7.8.2 that calculates thrust at a location $l = 66$ mm where l is the distance from the exit plane to the location of interest.

$$T_{estimate} \equiv \overline{T_{iB}} + \overline{T_{eP}} + \overline{T_{iP}} \quad (\text{Eq. 7.8.1})$$

$$T_{estimate} \equiv 1 \times 10^{-18} \int_0^{r_p(z)} [n_{iB}T_{iB} + n_eT_e + n_{iP}T_{iP}]rdr \quad (\text{Eq. 7.8.2})$$

$$T_{estimate,l} \equiv 1 \times 10^{-18} \int_0^{r_p(z)} \{ [n_{i,accel,l} \times (V_{mp,l} - V_{p,l})] + \dots \quad (\text{Eq. 7.8.3})$$

$$\dots [n_{e,l} \times T_{e,l}] + [(n_{i,TOT,l} - n_{i,accel,l})(\Delta V_P \times d_{0-l})] \} rdr$$

Additional assumptions required for thrust calculation include: 1) The accelerated ion beam population can be captured by computing the ion number density associated with the maximum RPA current collected. Due to LOESS smoothing and removal of outliers, this current is representative of the high-energy ion beam only. 2) Electron number density is equal to the total ion number density at a given location. 3) Electron temperature is representative of the entire electron population (both source electrons and plume electrons released during plume neutral ionization) due to electrons' high mobility and likelihood of equilibrating across the electron population. 4) The effect of thrust from plume ionization can be captured by computing the thrust contribution from the total ion number density as collected by the Langmuir probe (indiscriminant to ion energy) minus the ion number density of the high-energy ion beam as collected by the RPA. 5) The potential drop experienced by the newly formed ions is equal to the potential drop from the exit plane to the location of interest. Since the calculated mean free path lengths are longer than the acceleration region lengths of interest, all ions formed in the plume are assumed to survive and accelerate to the location of interest and beyond. 6) Due to heavy oscillations in plasma potential (a characteristic of capacitively-coupled plasmas), the magnitude of the potential drop is calculated based on the slope of a linear trend line representative of the plasma potential behavior as seen in Fig. 7.1.⁴¹ 7) Thrust augmentation due to charge exchange collisions is captured in the modification of most probable voltages and is not calculated directly. 8) Thrust contribution from neutrals exiting the discharge is not considered in this work.

Calculation of the thrust due to the accelerated ion beam equals the ion number density of the accelerated ion population at 66 mm ($n_{i,accel,66}$) times the difference

between the most probable voltage at 66 mm ($V_{mp,66}$) and the plasma potential at 66 mm ($V_{p,66}$). $V_{p,66}$ is estimated using the equation associated with the corresponding linear trend line as shown in Fig. 7.1. The ion number density of the accelerated ion beam is the corresponding number density calculated from the maximum current collected by the RPA. The contribution to thrust due to electron pressure equals the electron number density at 66 mm ($n_{e,66}$) times the electron temperature at 66 mm ($T_{e,66}$). Electron number density is equal to the total ion density at the 66 mm location ($n_{i,TOT,66}$). The thrust contribution from neutrals ionized in the plume and accelerated by local potential drops assumes that all the ions at the 66 mm location not affiliated with the ion beam are neutrals formed at the exit plane and are accelerated by the potential drop between the local plasma potential at the exit plane and the local plasma potential at 66 mm. Due to heavy oscillations in plasma potential, this value is represented as the slope of the linear trend line representative of the change in plasma potential along the thruster centerline (ΔV_p) times the distance from the exit plane to the area of interest (d_{0-66}).

The resulting calculated thrust values in Table 7.4 represent an estimate of the magnitude of thrust produced by electron pressure ($n_e T_e$) and magnetic field pressure by the ion beam ($n_{iB} T_{iB}$) and the newly formed ions downstream of the thruster exit ($n_{iP} T_{iP}$) on the thruster centerline at a distance of 66 mm downstream of the exit plane. A complete estimate of thrust performance is not possible without direct measurement at all locations in the exhaust plume. Present working models of magnetic nozzle exhaust plumes are unable to predict plasma properties influenced by the magnetic nozzle.⁴²

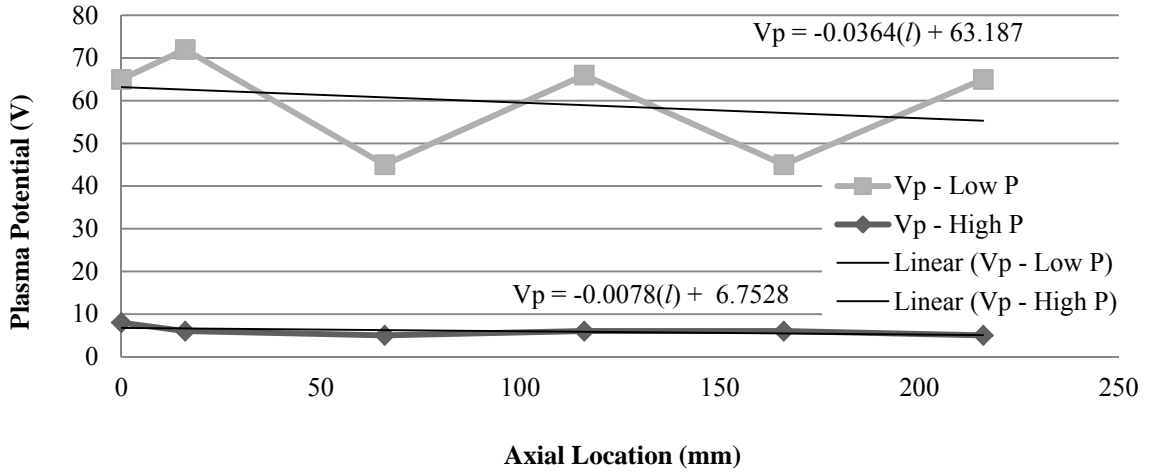


Figure 7.1: Linear plasma potential trend lines for Langmuir probe plasma potential measurements for both the ‘Low-Pressure Condition’ and ‘High-Pressure Condition’ at 2 sccm argon volumetric flow rate, 100 W RF power, and 340 G magnetic field strength thruster operation. Linear trends calculated based on plasma potential measurements from the thruster exit plane to 216 mm downstream of the thruster exit plane.

Table 7.5: Estimated thrust density contributions from the accelerated ion beam ($n_{iB}T_{iB}$), electron pressure (n_eT_e), and newly ionized plume neutrals ($n_{iP}T_{iP}$) calculated for the centerline ($r = 0$ m) at a location 66 mm downstream of the exit plane for both the ‘Low-Pressure Condition’ and ‘High-Pressure Condition’ at 2 sccm argon volumetric flow rate, 100 W RF power, and 340 G magnetic field strength thruster operation.

| Property | ‘Low-Pressure Condition’ | ‘High-Pressure Condition’ |
|----------------|---|---|
| $n_{iB}T_{iB}$ | 1.7×10^{-24} (N/m ²) | 3.1×10^{-25} (N/m ²) |
| n_eT_e | 1.9×10^{-23} (N/m ²) | 1.0×10^{-22} (N/m ²) |
| $n_{iP}T_{iP}$ | 1.3×10^{-23} (N/m ²) | 1.7×10^{-22} (N/m ²) |

Initial thrust density estimations presented in Table 7.5 show that the ‘high-pressure condition’ produces more than three times the thrust of the ‘low-pressure condition’ despite producing an order of magnitude lower thrust from its accelerated ion beam. The thrust contributor with the greatest impact on thrust at both conditions is the thrust due to

electron pressure that is directly influenced by plume ionization; electrons released during the ionization of plume neutrals raise the electron number density, raising the thrust produced by electron pressure. Despite the smaller potential drop available to newly formed plume ions (3 eV versus 28 eV for the ‘low-pressure condition’ and 0.3 eV versus 4 eV for the ‘high-pressure condition’), the large ion number densities in the plume due to plume neutral ionization versus the accelerated ion beam ion number densities ($2.7 \times 10^{13} \text{ ions/m}^3$ versus $3.9 \times 10^{11} \text{ ions/m}^3$ for the ‘low-pressure condition’ and $3.5 \times 10^{14} \text{ ions/m}^3$ versus $4.8 \times 10^{11} \text{ ions/m}^3$ for the ‘high-pressure condition’) result in the second largest contributor to total thrust. When considering the ion beam exclusively, greater thrust is calculated to occur at the ‘low-pressure condition.’ The accelerated ion beam however cannot compete with the thrust contributions from neutrals formed in the plume.

Due to the large contribution to thrust generated by the plume ions and the enhanced population of electrons at both pressure conditions, it is unclear whether plume neutrals would still form at such influential numbers when operating in a true vacuum. The total number of plume ions that will naturally form as unionized propellant leaves the discharge chamber is unclear. Additional tests at lower operating pressure as well as an examination of pressure properties inside the discharge chamber are required to make an estimate of the amount of plume ion production that can be expected during Helicon ion thruster operation.

Thrust values presented in Table 7.5 represent a best estimate of thrust generation outside of conducting direct thrust measurements. From these predictions, it is clear that thrust calculation completed using plasma property values subject to neutral ingestion

results in inflated thrust predictions. Thrust predicted for the ‘high-pressure condition’ exceeds thrust estimated at the ‘low-pressure condition’ and in turn, misrepresents thruster performance possible for actual space applications.

7.1.4 Electron Cooling

Examination of the remaining plasma properties affected by increased neutral number density in the plume reveals electron cooling behavior at the ‘high-pressure condition.’ Electron temperature at the ‘high-pressure condition’ is consistently lower than the electron temperature at the ‘low-pressure condition’ across the full downstream range investigated. A comparison of electron temperatures from the two pressure cases as shown in Fig 6.15 supports the notion of increased neutral collisions at the ‘high-pressure condition.’ Electrons exhibit a cooling behavior during travel through higher neutral density environments due to repeated collisions with neutral atoms resulting in a reduction of electron temperature.⁴³ Electron cooling behavior has been experimentally shown to scale with neutral density and is prevalent here in the reduced electron temperatures at the ‘high-pressure condition.’⁴³

7.1.5 Summary

Differences in plasma behavior between the ‘high-pressure condition’ and the ‘low-pressure condition’ are caused by two primary neutral-plume interactions. The first interaction concerns charge exchange and momentum exchange collisions which result in the reduction of the accelerated ion population energy at the ‘high-pressure condition.’ Reduced ion energy is denoted by a decrease in the most probable voltage of the IEDF. The higher overall ion number density at the ‘high-pressure condition’ is due to the

second interaction: plume neutral ionization. The newly formed ions in the exhaust plume are eligible to undergo acceleration in the plume due to the pre-existing plasma potential drops. Newly formed ions that undergo acceleration result in a greater thrust value prediction at the ‘high-pressure condition. The primary effects of neutral ingestion in the Helicon ion thruster plume are a reduction in ion and electron energies as well as an increase in ion number density. A complete diagram is provided in Appendix B.

7.2 Neutral Ingestions Effects on Increasing RF Power and Performance Metrics

Section 6.2.3 compared the most probable voltage of the IEDF, electron temperature, plasma potential, and ion number density across a range of RF power levels for both the ‘high-pressure condition’ and ‘low-pressure condition.’ Values were recorded for MadHeX Replica operation on 2 sccm argon volumetric flow rate and 340 G magnetic field strength over an RF power range of approximately 100 W to 500 W at the thruster exit plane and, in some cases, 16 mm downstream from the thruster exit plane. Using this data, changes in plume behavior and plasma properties are compared to determine the effect of increasing Helicon ion thruster RF power on the magnitude of the neutral ingestion effects identified in Sec. 7.1 on thrust generation and on performance metrics at both the ‘high-pressure condition’ and ‘low-pressure condition.’

7.2.1 RF Forward Power Absorption by Environmental Neutrals

Increasing RF power in the Helicon ion thruster deposits more energy into the source region propellant as well as depositing energy in any additional gases located in areas not shielded from the RF antenna inside the vacuum chamber. Increases in energy of the ion

population are equivalent to increases in the most probable voltage of the IEDF. For both pressure conditions, increasing RF power results in increases to the most probable voltages as illustrated in Fig. 6.26. The magnitudes of the increases of the most probable voltages for the ‘low-pressure condition’ however are much greater than the corresponding increases in most probable voltages for the ‘high-pressure condition’ as illustrated in Table 7.6.

Table 7.6: Comparison of rate of increase in most probable voltage with increasing RF Power for 2 sccm argon volumetric flow rate and 340 G source region magnetic field strength between ‘low-pressure condition’ and ‘high-pressure condition.’

| RF Power Transition | ‘Low-Pressure Condition’ | | ‘High-Pressure Condition’ | |
|---------------------|--------------------------|------------------|---------------------------|------------------|
| | dV_{mp}/W | $dV_{mp,corr}/W$ | dV_{mp}/W | $dV_{mp,corr}/W$ |
| 100 W – 200 W | 0.206 V/W | 0.451 V/W | 0.045 V/W | 0.091 V/W |
| 200 W – 300 W | 0.234 V/W | 0.106 V/W | 0.082 V/W | 0.051 V/W |

The most probable voltage for the ‘low-pressure condition’ increases five times more per watt than the most probable voltage for the ‘high-pressure condition’ when power is raised from 100 to 200 W RF power. The increase per watt of RF power for the transition from 200 to 300 W at the ‘low-pressure condition’ is three times higher than at the ‘high-pressure condition.’ Despite an equal amount of power leaving the antenna, ion energy gains at the ‘high-pressure condition’ are consistently less than the gains achieved at the ‘low-pressure condition.’ At the ‘high-pressure condition’, both the larger population of environmental neutral argon atoms and the accelerated ion population absorb the additional RF power. RF power absorption can result in increasing ion energy as noted earlier, or in increased ionization of argon propellant. During operation at the ‘high-pressure condition,’ additional ionization is not limited to the propellant inside the discharge chamber.

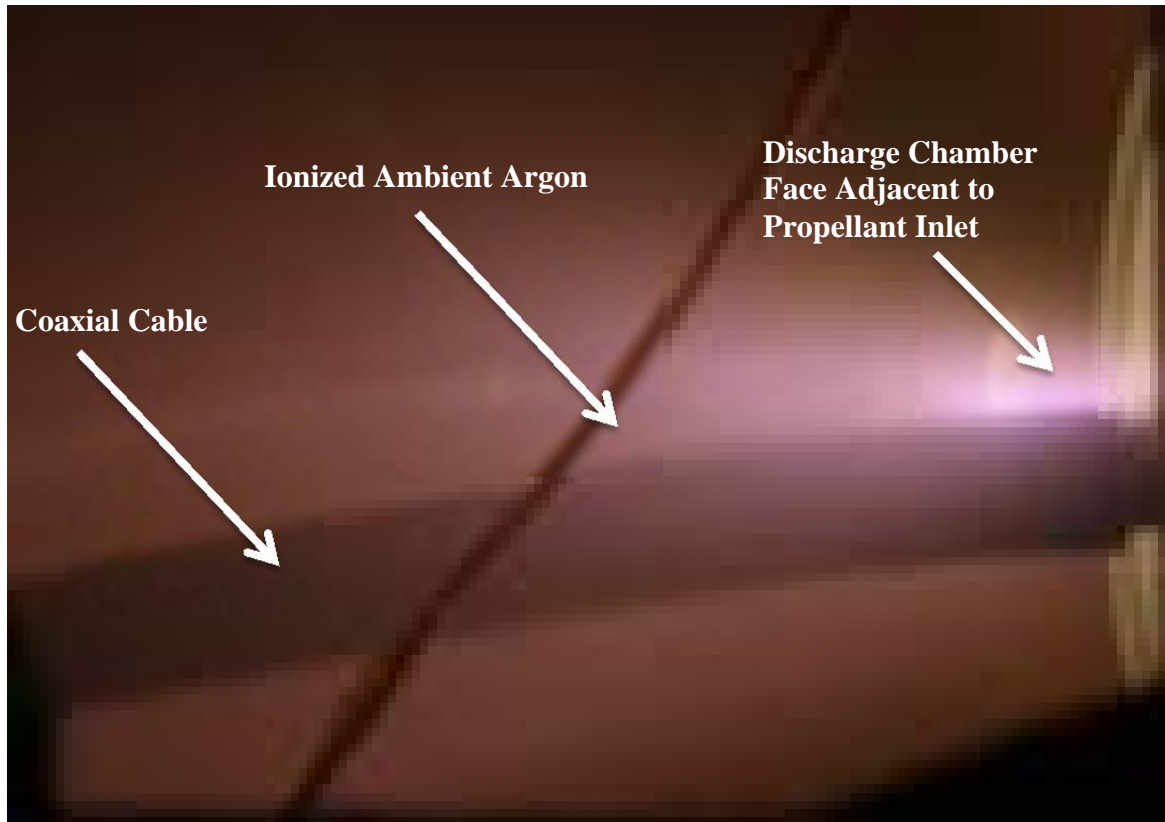


Figure 7.2: Ambient argon ionization around RF coaxial cable at the ‘High-Pressure Condition’ at 2 sccm argon volumetric flow rate, 100 W RF power, and 340 G magnetic field strength thruster operation.

While this process can occur for both pressure conditions, the ambient argon neutral population for the ‘high-pressure condition’ ($n_o = 2.14 \times 10^{18} \text{ atoms/m}^3$) is so much greater than for the ‘low-pressure condition’ ($n_o = 4.54 \times 10^{17} \text{ atoms/m}^3$) that the increases in the ion energy and the subsequent increases on the most probable voltages are damped as observed in Table 7.6. This damping effect due to energy absorption by the environmental neutral atom population can also lead to ionization of neutral atoms surrounding the thruster. Figure 7.2 illustrates ambient neutral ionization where argon plasma is generated around the magnet coils and RF coaxial power line. These ions

however, are too far from the exit plane and diverging magnetic field to contribute to thrust like ions generated in the exhaust plume.

7.2.2 Neutral Ingestion Effects on Collision Frequency and Plume Ionization at Increasing RF Power

The neutral ingestion effects on plasma properties discussed in Sec. 7.1 related the collision rates and plume neutral ionization occurring in the exhaust plume to the facility background pressure. The effect of increasing RF power on the collision and plume ionization rates requires an examination of the affiliated plasma properties from Eq. 7.2 – 7.7. Since background argon pressures remain the same within each pressure condition, the neutral number density and resulting mean free paths remain the same as shown in Table 7.2 and 7.4 at all RF power levels. Other properties that change with increasing RF power include the corrected most probable voltage which affects the beam current velocity calculated using Eq. 7.3 and the electron number densities used in calculating the production rate of plume ions from Eq. 7.6.

Without a change in mean free path, charge exchange and momentum exchange collisions continue to occur far downstream of the range of consideration during thruster operation at the ‘low-pressure condition.’ Collision frequencies at the ‘high-pressure condition’ however, are directly affected by changes in RF power due to changes in ion beam velocity related to the corrected most probable voltages displayed in Fig.6.26. Collision frequencies are calculated in Table 7.7 for operation of the MadHeX replica at the ‘high-pressure condition.’ Collision frequencies for both collision types considered at the ‘high-pressure condition’ increase with increasing corrected most probable voltage.

Table 7.7: Comparison of charge exchange (v_{CT}) and momentum exchange (v_{MT}) collision frequencies at the ‘high-pressure condition’ at the exit plane at 2 sccm argon volumetric flow rate and 340 G magnetic field strength thruster operation for charge exchange collisions and plume argon ionization over an RF power range of ~100 W – ~500 W.

| ‘High-Pressure Condition’ | | | | | |
|----------------------------------|--------------|--------------|--------------|--------------|--------------|
| RF Power Level | 101 W | 223 W | 333 W | 430 W | 521 W |
| v_{CT} ($coll/s$) | 9,346 | 14,152 | 16,215 | 15,529 | 14,954 |
| v_{MT} ($coll/s$) | 13,277 | 20,104 | 23,035 | 22,060 | 21,243 |

Plume neutral ionization affects both pressure conditions and is calculated over the RF power range of interest in Table 7.8. In addition to ion number density, electron temperature will also effect the production of plume neutrals due to its relationship with electron velocity from Eq. 7.7. Electron temperature however, is not significantly influenced by changing RF forward power over this range.²²⁻²³ As discussed in Sec. 7.1.4, the electron cooling effect influencing electron temperature scales with neutral number density which does not change with increasing RF power. Electron cooling due to collisions with the neutral population remains steady at the ‘high-pressure condition’ as observed in Fig. 6.27 where electron temperature deviates a maximum of 0.4 eV from the average electron temperature of 2.6 eV across the full RF power range considered. Electron temperature for the ‘low-pressure condition’ also remains within 0.4 eV of its average electron temperature of 5.8 eV up to the 307 W operating condition. The drop in electron temperature at the 417 W and 485 W operating conditions is not a result of electron cooling and will be discussed later in Sec. 7.2.3 as it relates to RF coupling mode transitions.

Table 7.8: Comparison of plume neutral ionization collision frequencies and production rates for both the ‘low-pressure condition’ and the ‘high-pressure condition’ at the exit plane at 2 sccm argon volumetric flow rate and 340 G magnetic field strength thruster operation for charge exchange collisions and plume argon ionization over an RF power range of ~100 W – ~500 W.

| ‘Low-Pressure Condition’ | | | | | |
|--|----------------------|----------------------|----------------------|----------------------|----------------------|
| RF Power Level | 100 W | 212 W | 307 W | 417 W | 485 W |
| $\nu_{Plume} (coll/s)$ | 1.1×10^7 | 1.0×10^7 | 1.0×10^7 | 5.7×10^6 | 8.5×10^6 |
| $\frac{dn_i}{dt}_{Plume} (ions/s \cdot m^3)$ | 6.6×10^{20} | 8.6×10^{20} | 1.2×10^{21} | 1.8×10^{21} | 1.5×10^{22} |
| ‘High-Pressure Condition’ | | | | | |
| RF Power Level | 105 W | 207 W | 303 W | 418 W | 510 W |
| $\nu_{Plume} (coll/s)$ | 3.2×10^7 | 3.7×10^7 | 3.1×10^7 | 3.5×10^7 | 3.5×10^7 |
| $\frac{dn_i}{dt}_{Plume} (ions/s \cdot m^3)$ | 7.0×10^{21} | 8.0×10^{21} | 1.1×10^{22} | 1.2×10^{22} | 1.2×10^{22} |

Plume neutral ionization collision frequencies continue to be higher for the ‘high-pressure condition’ than the ‘low-pressure condition’ across the full RF power range considered. Due to the correlation of collision frequency with the relatively constant electron temperature, neutral ionization collision frequency for the ‘high-pressure condition’ is consistently three times the collision frequency at the ‘low-pressure condition’ up until the 400 W operating condition when electron temperature drops. This behavior however is a result of transitioning to a new RF coupling mode and not a function of the RF power as discussed in Sec. 7.2.3.

While the collision frequencies between corresponding RF powers remain consistently higher for the ‘high-pressure condition,’ the same behavior is not observed for ion production rate in the plume. Ion production rate for the ‘low-pressure condition’

at the 485 W operating condition exceeds the ion production rate at the ‘high-pressure condition.’ This change in ion production follows trends observed in the ion number density behavior illustrated in Fig. 6.28. The ratio of ion production at the ‘high-pressure condition’ to the ion production at the ‘low-pressure condition’ drops with increasing RF power as observed in Fig. 7.3. This behavior follows the behavior of the ratio of the ion number density at the ‘high-pressure condition’ to the ion number density at the ‘low-pressure condition’ represented in Fig. 7.3.

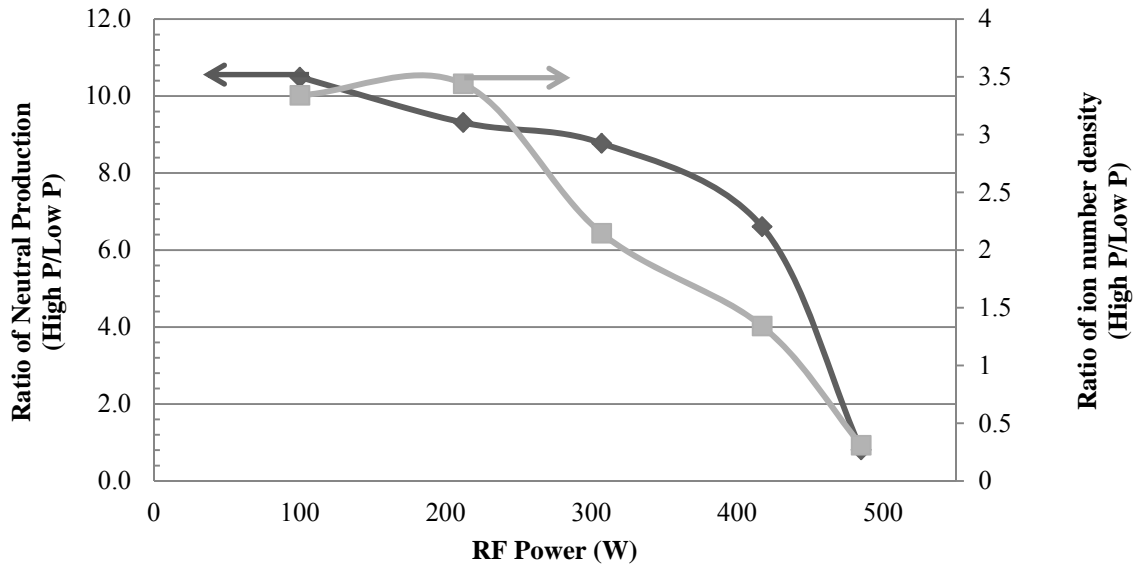


Figure 7.3: (Left) Ratio of the plume ion production rate at the ‘high- pressure condition’ divided by the ion production rate at the ‘low- pressure condition’ at 2 sccm argon volumetric flow rate and 340 G magnetic field strength thruster operation over an RF power range of 100 W – 500 W. (Right) Ratio of the ion number density at the ‘high- pressure condition’ divided by the ion number density at the ‘low-pressure condition’ at 2 sccm argon volumetric flow rate and 340 G magnetic field strength thruster operation over an RF power range of 100 – 500 W.

As RF power increases, the rate of ion production in the plume at the ‘low-pressure condition’ approaches and exceeds the rate of ion production in the plume at the ‘high-

pressure condition.’ This behavior is due to increased ion number density and the resulting increase in hot plume electrons available for ionizing collisions with plume neutrals. Despite the larger neutral population available at the ‘high-pressure condition,’ the increase in hot plume electrons at the 485 W operating condition for the ‘low-pressure condition’ yields greater rates of ion production in the exhaust plume.

7.2.3 Neutral Ingestion Effects on RF Coupling Mode Transitions at Increasing RF Power

Figure 7.3 shows that the rate of ion production in the plume for the ‘low-pressure condition’ overtakes the ion production rate of the ‘high-pressure condition’ at approximately 500 W of RF power. This behavior is attributed to the order of magnitude increase of ion number density that occurs during operation at 485 W in the ‘low-pressure condition.’ This order of magnitude increase in ion number density is indicative of a transition between RF coupling modes discussed in Sec. 2.2.1. Due to the lack of a blue core, transition is assumed to occur from a CCP to an ICP at the ‘low-pressure condition’ between 417 W and 485 W.

A similar increase in ion number density is not observed for the ‘high-pressure condition’ leading to the assumption that an RF coupling mode transition does not occur and thruster operation is observed in the CCP mode only. Due to the physical mechanisms that drive the change in RF coupling mode, the RF power loss due to absorption by ambient neutral population is assumed responsible for disabling a transition at the ‘high-pressure condition.’ Additional neutral atoms may interfere with a coupling mode transition due to increased neutral collisions as well as shown in Table 7.7. A thrust comparison is conducted in Sec. 7.2.5 to determine if the transition to an ICP and the

affiliated increase in ion number density enables the ‘low-pressure condition’ to exceed the ‘high-pressure condition’ in thrust generation.

A transition to the Helicon coupling mode does not occur in this study of MadHeX replica operation. The mechanisms that result from neutral ingestion however are still valid concerns for Helicon ion thruster operation. While the magnitude of the effects of neutral ingestion would be affected by a transition to Helicon mode, the effects themselves would not be ameliorated by operating in a different RF coupling mode.

7.2.4 Neutral Ingestion Effects on Double Layer formation at Increasing RF Power

The other performance metric of interest in this study is the formation of a double Layer potential structure. In comparing IEDF trace behavior for RF power levels between 100 W and 300 W, additional contrasting behavior emerges during operation at the ‘high-pressure condition.’ At the 214 W RF power, 2 sccm argon volumetric flowrate, and 340 G magnetic field strength thruster operating condition, a double peaked IEDF is observed as shown in Fig. 6.17. A persistent, double-peaked IEDF indicates the formation of the Double Layer as described in Section 2.2.2. Examination of the IEDF at the ‘low-pressure condition’ does not reveal a double peaked IEDF and the Double Layer is presumed absent.

Examination of additional trials at the 214 W operating condition during operation at the ‘high-pressure condition’ does not reveal persistent, double-peaked profiles. The behavior observed during Trial 3 may indicate an unsteady Double Layer or an oscillating RF sheath.

If an unsteady Double Layer is assumed, the benefits of a Double Layer are not achieved. The intention of the Double Layer is to produce a large plasma potential drop

to accelerate ions over a short distance (a few Debye lengths) to generate thrust. In comparing the corrected most probable voltages for the possible Double Layer IEDF at the ‘high-pressure condition’ with the ‘low-pressure condition’ corrected most probable voltages, the ‘low-pressure condition’ has a corrected most probable voltage more than 30 V higher at 200 W than either corrected most probable voltage for the ‘high-pressure case.’ Despite producing two accelerated ion populations, the potential Double Layer formed at the 200 W, ‘high-pressure condition’ does not produce a potential drop for the ion beam larger than the potential drop at the ‘low-pressure condition.’

7.2.5 Magnitude of Estimated Thrust Augmentation due to Neutral Ingestion While Increasing RF Power

In order to quantify the effect neutral ingestion has on estimated thruster performance at different RF power levels, some simplified thrust calculations are conducted assuming that the bulk ion thrust is generated by newly formed ions outside the discharge chamber. Since electron pressure and plume ion acceleration were the two largest thrust contributing terms in the previous section, those two will be considered here in order to compare estimated thrust magnitudes across the available RF power range.

For these calculations, the exit plane ion number density at each RF power level is used with a presumed potential drop to represent new ions accelerated in the plume. Since plasma potential values are found to remain relatively constant across the power level range of 100 – 500 W as recorded by the emissive probe, potential drops of 0.3 V for the ‘high-pressure condition’ and 3 V for the ‘low-pressure condition’ are assumed to be applicable for this study. An estimate of thrust at the exit place ($T_{estimate,0}$) is calculated using Eq. 7.8.4 where electron number density ($n_{e,0}$) is assume to be the same

as the total ion number density ($n_{i,TOT,0}$) and the potential drop across which the plume ions travel (ΔV) is given by the aforementioned values.

$$T_{estimate,0} \equiv 1 * 10^{-18} \int_0^{r_p(z)} [n_{e,0} * (T_{e,0})] + [(n_{i,TOT,0}) * (\Delta V)] r dr \quad (\text{Eq. 7.8.4})$$

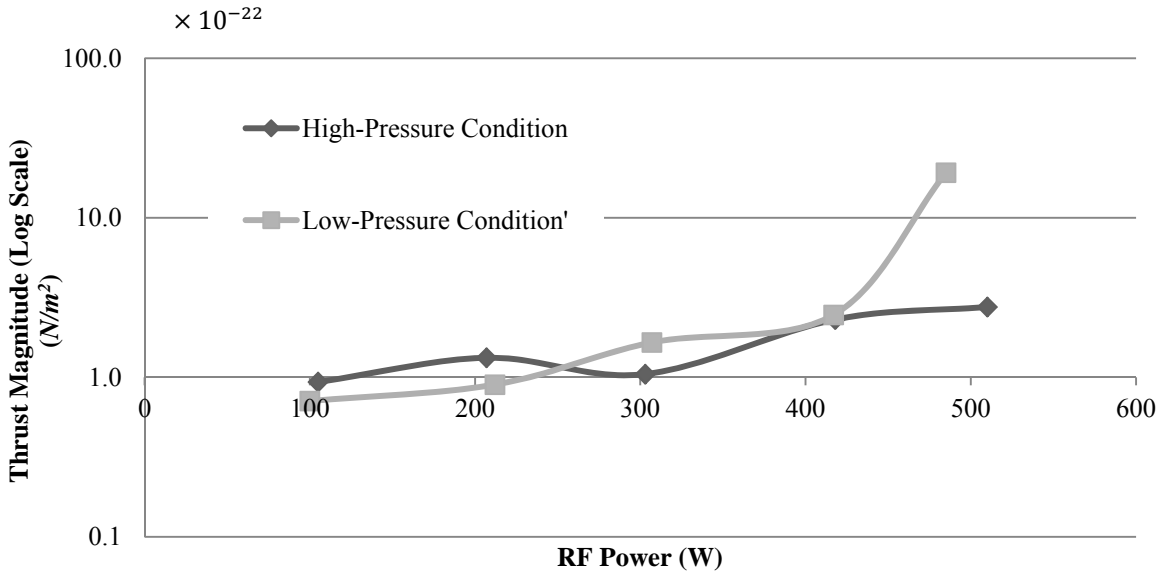


Figure 7.4: Total calculated magnitude of thrust generated at $r = 0$ for 2 sccm argon volumetric flow rate and 340 G source region magnetic field strength at the ‘low-pressure condition’ and the ‘high-pressure condition’ over an RF power range of ~100 W – ~500 W.

Thrust increases with increasing RF power for both pressure conditions due to the associated increase in ion number density. The RF power level of greatest interest is the ~500 W power level where the ‘low-pressure condition’ produces a magnitude of thrust greater than the corresponding ‘high-pressure condition.’ This exponential increase in thrust generation at the ‘low-pressure condition’ is due to the corresponding increase in ion number density of $1.4 \times 10^{15} \text{ ions/m}^3$ between the 400 W and ~500 W power levels shown in Fig. 6.28. Thrust generation at the ‘low-pressure condition’ is estimated to

exceed thrust generated at the ‘high-pressure condition’ once the RF mode transitions to an ICP increasing ion number density which is estimate to generate greater thrust. The inability of the thruster to transition to a different coupling mode at the ‘high-pressure condition’ is due to absorption of RF power by ambient propellant.

7.2.6 Summary of Neutral Ingestion Effects with Increasing RF Power on Thrust Generation, Plasma Properties, RF Coupling Mode Transition, and Double Layer Formation

As RF power increases, the effect of neutral ingestion on thruster performance becomes detrimental. Increases in most probable voltages occur at greater rates for the ‘low-pressure condition’ as compared to the ‘high-pressure condition’ due to RF power absorption by ambient propellant leading to environmental neutral ionization and lowering the energy available to propellant located in the thruster source region. Collision frequencies for charge exchange and momentum exchange collisions increase at the ‘high-pressure condition’ leading to additional losses of ion energy. Plume neutral ionization is consistently higher for the ‘high-pressure condition,’ but the rate of ion production is exceeded at the ‘low-pressure condition’ for the 485 W operating condition.

Double Layer formation may occur at the ‘high-pressure condition’ but fails to yield a more favorable potential drop of the accelerated ion population than the ‘low-pressure condition’ potential drop. Thrust generation is estimated to be most greatly affected by the ability of the thruster to transition from a CCP to an ICP at the ‘low-pressure condition.’ Operation in Helicon mode is not achieved; however, the mechanisms resulting from neutral ingestion still affect thruster performance. The magnitude of the effects of neutral ingestion during thruster operation at Helicon mode is a future point of

study. At higher RF power levels, higher operating pressures degrade thruster performance by inhibiting RF coupling transitions and absorbing RF power.

7.3 Neutral Ingestions Effects and Increasing Magnetic Field Strength

Section 6.2.6 compared the most probable voltage of the IEDF, electron temperature, plasma potential, and ion number density across a range of magnetic field strengths for both the ‘high-pressure condition’ and ‘low-pressure condition.’ Values were recorded for MadHeX Replica operation on 2 sccm argon volumetric flow rate and 100 W RF power over a magnetic field strength range of approximately 340 G – 500 G (up to 700 G) at the thruster exit plane and, in some cases, 56 mm downstream from the thruster exit plane. Using this data, changes in plume behavior and plasma properties are compared to determine the effect of increasing Helicon ion thruster magnetic field strength on the magnitude of the neutral ingestion effects identified in Sec. 7.1 on thrust generation and on performance metrics at both the ‘high-pressure condition’ and ‘low-pressure condition.’ Due to anomalous readings at the 400 G operating condition during testing at the ‘high-pressure condition,’ properties recorded at 400 G are excluded from this analysis. Probe failure at the 400 G condition is suspected as the cause of the anomalous readings since the 400 G condition was the final condition measured.

7.3.1 Neutral Ingestion Effects on Charge Exchange Collisions and Plume Ionization at Increasing Magnetic Field Strength

Examination of plasma properties subject to increasing magnetic field strength from Sec. 6.2.6 reveals limited differences due to neutral ingestion across the magnetic field strength range considered. The IEDFs for both cases drop in height with slight shifting of

the most probable voltage to higher values. This behavior along with the decreasing ion number density and decreasing electron temperature (at the ‘low-pressure condition’) can be attributed to increasing electron confinement and restricted electron mobility caused by increasing magnetic field strength.⁴⁴⁻⁴⁵

In assessing the magnitude of confinement’s influence on the accelerated ion beam in the presence of neutral ingestion, corrected most probable voltages between the ‘low-pressure condition’ and the ‘high-pressure condition’ are compared. At the ‘low-pressure condition,’ corrected most probable voltage increases 14 V between the 340 G and 500 G conditions whereas the ‘high-pressure condition’ corrected most probable voltage increases only 4 V over the same magnetic field increase. Beyond 500 G however, corrected most probable voltage deviates less than 3 V for both pressure conditions from their respective averages.

Ion number density for both pressure conditions also exhibits similar behavior due to increasing magnetic field strength. Ion number density for the ‘low-pressure condition’ decreases by 15% of the 340 G ion number density by 500 G magnetic field strength. Likewise, the ‘high-pressure condition’ ion number density decreases by 15% of its 340 G value by the 500 G operating condition. While the rate of decrease in ion number density of -3×10^{11} ions/m³per G is greater at the ‘high-pressure condition’ than the -7×10^{10} ions/m³per G rate of decrease at the ‘low-pressure condition,’ magnetic field confinement effects the same percentage of the ion population at both pressure conditions. The changes in ion number density however may be obscured when accounting for the ion number density uncertainty of $\pm 50\%$.

In contrast, property trends are not the same for the electron temperature behavior illustrated in Fig 6.41 for both pressure conditions. Electron temperature for the ‘high-pressure condition’ deviates less than 30% from its average value of 2.1 eV from the 340 G operating condition to 700 G operating condition. This behavior is in contrast to the cooling behavior observed at the ‘low-pressure condition’ when electron temperature decreases from 5.6 eV to 3.5 eV. Electron temperature at the ‘low-pressure condition’ decreases due to increased electron confinement and mobility whereas electron temperature at the ‘high-pressure condition’ is dominated by the electron cooling mechanism discussed in Sec. 7.1.4. Electron-neutral collisions dominate at the ‘high-pressure condition’ overwhelm any potential decrease in electron temperature due to magnetic field confinement.

Beyond the 500 G operating condition, most probable voltage and electron temperature remain constant despite increasing magnetic field strength. Since corrected most probable voltage and electron temperature govern the charge exchange and plume ionization collision rates, collision frequencies for both pressure conditions remain constant beyond the 500 G operating condition. Plume ion production decreases due to the influence of ion number density for both pressure conditions as shown in Table 7.9.

Table 7.9: Comparison of plume ion production rates for both the ‘Low-Pressure Condition’ and the ‘High-Pressure Condition’ at the exit plane at 2 sccm argon volumetric flow rate and 100 W RF power thruster operation for charge exchange collisions and plume argon ionization over a magnetic field strength range of 340 G to 700 G.

| ‘Low-Pressure Condition’ | | | | | |
|--|----------------------|----------------------|----------------------|----------------------|----------------------|
| Magnetic Field Strength | 340 G | 500 G | 600 G | 670 G | 700 G |
| $\frac{dn_i}{dt}_{plume}$ (ions/s · m ³) | 5.8×10^{20} | 3.8×10^{20} | -- | -- | -- |
| ‘High-Pressure Condition’ | | | | | |
| Magnetic Field Strength | 340 G | 500 G | 600 G | 670 G | 700 G |
| $\frac{dn_i}{dt}_{plume}$ (ions/s · m ³) | 8.0×10^{21} | 6.7×10^{21} | 6.1×10^{21} | 6.0×10^{21} | 6.0×10^{21} |

7.3.2 Thrust Augmentation and Increasing Magnetic Field Strength

In order to quantify the effect neutral ingestion has on thruster performance at different magnetic field strengths, some simplified thrust calculations are conducted using Eq. 7.8.4. Calculated thrust values are shown in Fig. 7.5 assuming that electron pressure and ion plume ionization are still the bulk contributors to thrust. Due to decreasing ion number density and low electron temperatures, thrust for both pressure conditions decreases with increasing magnetic field strength. In addition, plume ions formed at the 500 G condition and above for the ‘high-pressure condition’ no longer contribute to thrust due to the nearly 0 V/mm plasma potential gradient outside the thruster.

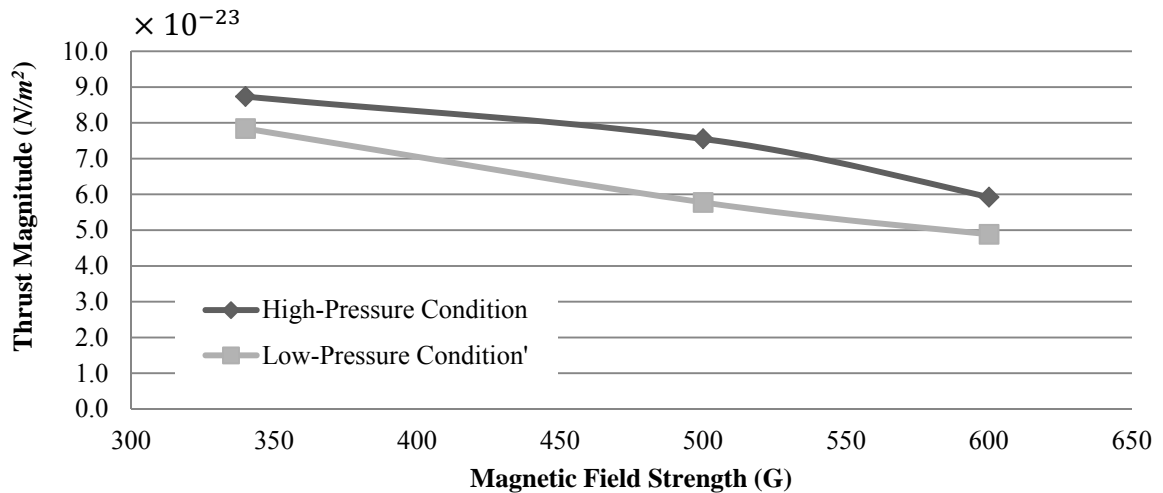


Figure 7.5: Magnitude of thrust generated at $r = 0$ for 2 sccm argon volumetric flow rate and 100 W RF Power thruster operation at the ‘low-pressure condition’ and the ‘high-pressure condition’ over 340 G – 600 G magnetic field strength.

Thrust for both pressure conditions decreases at a rate of $-8.2 \times 10^{26} \text{ N/m}^2$ per G with increasing magnetic field strength. Decreasing thrust is a result of reduced ion number density and electron temperature due to electron confinement and reduced electron mobility that is independent of background pressure. Thrust for the ‘high-pressure condition’ is also reduced by the decline of plasma potential in the first 140 G increase. While plasma potential remained the same for magnetic field strengths above 500 G for both conditions, because the plasma potential at the ‘high-pressure condition’ was only 4 V at the exit plane, this reduction eliminated the potential gradient needed to accelerate newly formed plume ions. While plasma potential was lowered for both pressure conditions, it had a greater detrimental effect on the ‘high-pressure condition.’

7.3.3 Summary of Neutral Ingestion Effects while Increasing Magnetic Field Strength on Thrust Generation and Plasma Properties

The primary effects of increasing magnetic field strength are universal across both pressure conditions. Both pressure conditions experienced reduced ion number density across the full range of magnetic field strengths tested and increased corrected most probable voltage until the 500 G operating condition. Electron temperature for the ‘low-pressure condition’ was reduced due to increased electron confinement and reduced electron mobility with correspondingly minimal change in electron temperature at the ‘high-pressure condition’ due to dominating electron cooling caused by electron-neutral collisions. Thrust at both conditions decreased due to reducing ion number density. Thrust augmentation for the ‘high-pressure condition’ was more severe due to the elimination of the potential gradient outside the thruster exit plane disabling the ability of newly formed plume ions to contribute to acceleration. Despite the reduction in plasma potential affecting both pressure conditions, due to the already low values of plasma potential at the ‘high-pressure condition’ only thrust generated at the ‘high-pressure condition’ was affected by changing plasma potential values in the first 160 G increase.

7.4 Volumetric Flow Rate Effects at the ‘Low-Pressure Condition’

Section 6.3 compared the most probable voltage of the IEDF, electron temperature, plasma potential, and ion number density across a range of 1.3 sccm – 60 sccm argon volumetric flow rate for thruster operation at the ‘low-pressure condition.’ Values were recorded for MadHeX Replica operation on 100 W RF power and 340 G magnetic field

strength at the thruster exit plane. An examination of these values reveals the nature of increased neutral ingestion interactions with thruster operation and performance.

7.4.1 Trends of Increasing Volumetric Flow Rate Compared to Neutral Ingestion Trends

Changes in plasma property values, in response to changing volumetric flow rate, occur in distinct segments. IEDFs consistently shift to lower most probable voltages or reduce in height with increasing volumetric flow rate. Most probable voltages plotted in Fig. 6.45 follow the same behavior as the plasma potential resulting in a corrected most probable voltage that remains within 6 V of its average value of 31 V for all conditions except for the 4 sccm and 30 sccm operating conditions.

The 30 sccm operating condition also has the outlying electron temperature of 8.7 eV while all remaining conditions exhibit a slightly decreasing electron temperature with increasing volumetric flow rate from 6.1 eV to 5 eV over the full flow range considered. These changes in electron temperature may be ameliorated however when accounting for the $\pm 17\%$ analysis error. This slight decrease in temperature however may also be a result of electron cooling due to the increased availability of plume neutrals caused by the increase in propellant flow rates. The magnitude of electron cooling however is much less than the 2 sccm argon volumetric flow rate, 100 W RF power, and 340 G magnetic field strength operating condition at the ‘high-pressure condition.’ This difference in electron cooling is due to the increased occurrence of electron-neutral collisions occurring at the ‘high-pressure condition’ due to the 3.8 sccm environmental neutral ingestion rate. Environmental neutrals at the ‘high-pressure condition’ are not as energetic as neutrals

leaving the thruster source chamber at high volumetric flow rates at the ‘low-pressure condition’ resulting in less electron cooling behavior at the ‘low-pressure condition.’

Ion number density as a function of volumetric flow rate shown in Fig. 6.48 does not exhibit the monotonic trends present in the other plasma properties. Ion number density increases from the 1.3 sccm operating condition to a maximum value of $4.7 \times 10^{14} \text{ ions/m}^3$ at the 10 sccm operating condition. Beyond 10 sccm, ion number density asymptotically decreases to a final value of $1.2 \times 10^{14} \text{ ions/m}^3$ by the 60 sccm operating condition. This behavior is similar to the power absorption behavior exhibited by environmental neutrals at the ‘high-pressure condition’ discussed in Sec. 7.2.1. Ion number density increases with increasing propellant flow rate due to increased collisions in the source region of the thruster for a 100 W RF power resulting in increased ion production. Beyond 10 sccm, ionization in the source region becomes power limited and the increase in propellant neutral population in the source region prevents additional ionization by absorbing available RF energy much like the environmental neutrals in the ‘high-pressure condition.’ In this instance, power is deposited throughout the source region without a significant increase in ionization.

7.4.2 Summary of Increased Volumetric Flow Rate Effects and Neutral Ingestion Effects

Similar to the behavior induced by neutral ingestion at the ‘high-pressure condition,’ IEDFs approach lower most probable voltages with an increase in neutral propellant. Electron temperatures also exhibited cooling behavior at the higher volumetric flow rates similar to the cooling behavior previously observed at the ‘high-pressure condition’ but did not approach the 2.5 eV value exhibited at the ‘high-pressure condition’ for the 100

W RF power and 340 G magnetic field strength operating condition. Ion number densities at the 10 sccm operating condition and above meet or exceed the ion number density at the 100 W RF power and 340 G magnetic field strength operating condition during operation at the 'high-pressure condition.' Ion number density is the only 'high-pressure condition' plasma property able to be achieved by increasing volumetric flow rate.

While similar behavior was observed for higher volumetric flow rates of argon at the 'low-pressure condition,' most neutral ingestion effects at the 'high-pressure condition' occurred at a greater magnitude. Ion energies are lower and electron cooling is more prevalent in the presence of neutral ingestion. Comparison of plasma properties at the 'high-pressure condition' with plasma properties recorded for a range of flow rates tested at the 'low-pressure condition' reveals that neutral ingestion has greater influence in the exhaust plume of the Helicon ion thruster and not in the source region as originally expected.

CHAPTER VIII

CONCLUSIONS

8.1 Effect of Neutral Ingestion on Helicon Ion Thruster Operation

In order to quantify the effect of neutral ingestion on Helicon ion thruster operation, a replica of the MadHeX was operated over a range of 1.3 – 60 sccm argon volumetric flow rate, 100 W – 700 W RF power, and 340 G – 700 G magnetic field strength for two distinct operating pressure conditions. Operating pressures were chosen based on Randolph's limit for HET characterization of 5×10^{-5} Torr and are designated as the 'low-pressure condition' for thruster operation below Randolph's limit and the 'high-pressure condition' for thruster operation above Randolph's limit. Plasma properties were compared between both pressure conditions to understand the physical mechanisms behind changes in most probable voltage of the IEDF, electron temperature, ion number density, and plasma potential due to neutral ingestion.

Differences in plasma behavior between the 'high-pressure condition' and the 'low-pressure condition' were caused by two primary neutral-plume interactions: collisions between accelerated beam ions and ingested neutrals resulting in a reduction of ion energy at the 'high-pressure condition' and neutral ionization downstream of the thruster exit due to increased electron-neutral collisions at the 'high-pressure condition.' The primary effects of neutral ingestion in the Helicon ion thruster exhaust plume at the 'high-pressure condition' are an increase in ion number density due to ionization of neutral propellant by hot plume electrons, a reduction in electron temperature due to

electron-neutral collisions resulting in electron cooling, and a reduction in the corrected most probable voltage due to energy losses between accelerated ions and ingested neutrals through charge exchange and momentum exchange collisions.

In examining the effect of increasing RF power on neutral ingestion effects, power absorption by propellant in the source region and downstream of the exit plane was inhibited at the ‘high-pressure condition’ due to power absorption by environmental neutrals affiliated with the increased operating pressure. Increases in most probable voltages occurred at greater rates for the ‘low-pressure condition.’ Ion number density also increased with increasing RF power leading to a coupling mode transition from a CCP to an ICP that occurred only for the ‘low-pressure condition.’ The primary effects of increasing magnetic field strengths were minimal and governed by the increased electron confinement and reduced electron mobility.

Increasing volumetric flow rate to mimic the increase in total flow rate due to neutral ingestion did exhibit some behaviors similar to the behaviors observed at the ‘high-pressure condition’ such as reduced electron temperature, decreased most probable voltages, and an overall increase in ion number density. Only ion number density was matched between operation at inflated propellant flow rates at the ‘low-pressure condition’ with operation at the nominal condition at the ‘high-pressure condition.’ These results suggest that the area of the thruster most heavily influenced by neutral ingestion at the ‘high-pressure condition’ is not the source region but in the exhaust plume.

Neutral ingestion in the plume of the Helicon ion thruster does affect the accelerated ion beam core. Changes in plasma properties on the thruster centerline imply that neutral ingestion in the exhaust plume is pervasive and the density of the ion beam is not high

enough to rely on scattering collisions at the edges of the exhaust plume to maintain the accelerated ion beam core as observed in HET operation.

8.2 Future Work

In order to determine an operational limit required for proper thruster characterization, additional testing at operating pressures below 1.2×10^{-5} Torr is required. Operation below Randolph's limit still allowed for a neutral ingestion rate of 0.8 sccm argon, exceeding his suggested 3% propellant ingestion limit. In addition, a shorter discharge chamber would also contribute extensively to the understanding of neutral ingestion effects on Helicon ion thruster operation. The collisional mean free paths involved in this work were 0.47 m and longer, a length on the order of the discharge chamber length but far beyond the exit plane for other Helicon ion thruster designs. An additional analysis involving discharge chambers shorter than the collisional mean free paths of interest may provide additional insights into operating pressure requirements based on thruster design.

Due to the extensive plume ionization observed at the 'low-pressure condition,' better understanding of acceleration mechanisms of RF magnetic nozzles is required to determine if the level of plume ionization can be expected during operation at vacuum or if Helicon ion thrusters require a higher vacuum for performance characterization. An overall improved understanding of thrust generation will also assist in quantifying the effect of estimating thrust performance in the presence of neutral ingestion. Additional study of Helicon ion thruster operation is required before their advantages can be capitalized.

APPENDIX A

Derivation of Quasi-1-D Model of Thrust Force for an Expanding Plasma in a Magnetic Nozzle

Assumptions

- Quasi 1-D
- Plasma expands along z in cylindrical geometry (variables independent of θ)
- Steady state
- Isotropic electron pressure (p_e)
 - $r_l > 10$ cm
 - $\bar{B} < 0.5$ G at location of thrust estimation for $T_e = 2.1$ eV minimum
- Neglect ion pressure
- Ignore induced supersonic rotation (no centripetal force)
- Neutral-gas pressure is neglected
- Ion-neutral collisions are an internal force and do not enter Thrust Calculations
- u_z & T_e are approximately constant across plasma.
- $u_z(z, r) \cong u_z(z)$
- $T_{el}(z, r) \cong T_e(z)$
- All values independent of θ

Variables

| | |
|--|---|
| \bar{B} : applied magnetic field \vec{E} : ambipolar electric field e : elementary charge N : neutral gas density n : plasma density r_l : Larmor radius T_b : Thrust due to magnetic field pressure | T_e : electron temperature T_s : Thrust due to electron pressure \vec{u} : ion velocity U_r : Radial neutral gas velocity U_z : Radial neutral gas velocity ν : ion-neutral collision frequency \vec{v} : electron velocity |
|--|---|

Calculations

Stead-State Momentum Equations:

Electrons

$$\begin{aligned}
 -en(E_r + V_\theta B_z) &= \frac{\partial P_e}{\partial r} \\
 -en(E_z - V_\theta B_r) &= \frac{\partial P_e}{\partial z}
 \end{aligned} \tag{1}$$

Ions

$$en(E_r + u_\theta B_z) = 0 \quad (2)$$

$$en(E_z - u_\theta B_r) - F_z = \frac{1}{r} \frac{\partial}{\partial r} (rmnu_r u_z) + \frac{\partial}{\partial z} (mnu_z^2)$$

Drag on ions due to ion-neutral collisions

$$F_z = mnu_z v \quad (3)$$

Axial Component of Momentum Equation of Neutral Gas

$$F_z = \frac{1}{r} \frac{\partial}{\partial r} (rmNu_r u_z) + \frac{\partial}{\partial z} (mNu_z^2) \quad (4)$$

Combining Steady-State Momentum Equations (1) & (2)

$$en(u_\theta - V_\theta)B_z = \frac{\partial p_e}{\partial r} \quad (5)$$

(expresses azimuthal current)

$$[en(V_\theta - u_\theta)]B_r = \frac{1}{r} \frac{\partial}{\partial r} (rmnu_r u_z) + \frac{\partial}{\partial z} (mnu_z^2 + p_e) + [F_z] \quad (6)$$

Use equation (5) to express azimuthal current and plug in to equation (6); plug in equation (4) to F_z term.

$$en(U_\theta V_\theta) = \frac{1}{B_z} \frac{\partial p_e}{\partial r} = -[en(V_\theta - u_\theta)] \quad \text{yields...}$$

Momentum Equation for Plasma-Neutral Gas Fluid

$$-\frac{B_r}{B_z} \frac{\partial p_e}{\partial r} = \left[\frac{1}{r} \frac{\partial}{\partial r} (rmnu_r u_z + rmNU_r U_z) \right] + \frac{\partial}{\partial z} (mnu_z^2 + p_e + mNU_z^2) \quad (8)$$

$$T_{total} = T_s + T_B \equiv \int_0^{r_p(z)} (mnu_z^2 + p_e + mNU_z^2) 2\pi r dr \quad (9) \& (11)$$

First term of (8) vanishes in integration across plasma radial cross section.

$$T_{total} \equiv \int_0^{r_p(z)} [(mnu_z^2 2\pi r dr) + (p_e 2\pi r dr) + (mNU_z^2 2\pi r dr)]$$

$$\equiv \int_0^{r_p(z)} [\omega \pi r mnu_z^2 dr + \omega \pi r p_e dr + 2\pi r mNU_z^2 dr]$$

$$\{fn(r): r, n, u_z\} + \{fn(r): r, p_e\} + \{fn(r): r, N, U_z^2\}$$

$$p_e = n_e k T_e$$

$$T_{Total} \equiv 2\pi \int_0^{r_p(z)} (m n u_z^2 + P_e + m N U_z^2) r dr$$

Calculating beam velocity

$$\equiv 2\pi \int_0^{r_p} \left[m n_i \left(\sqrt{\frac{k T_i}{m}} \right)^2 + n_e k T_e + m N \left(\sqrt{\frac{k T_N}{m}} \right)^2 \right] r dr$$

$$\equiv 2\pi \int_0^{r_p(z)} [n_i k_B T_i + n_e k_B T_e + N k_B T_N] r dr$$

$$\equiv 2\pi k_B \int_0^{r_p(z)} [n_i T_i + n_e T_e + N T_N] r dr \quad \begin{array}{l} \text{Assume singly-charged ions} \\ n_i = n_e \end{array}$$

$$\text{Using IEDF, } T_i = \left[\frac{(MPV - V_p)eV}{(8.62 \times 10^{-5} eV/K)} \right]$$

$$\equiv \frac{2}{\pi} k_B \int_0^{r_p(z)} [n_i (MPV - V_p) + n_e T_e + N T_N] r dr \quad \begin{array}{l} \text{Since singly charged,} \\ 1 V = 1 eV \end{array}$$

$$\text{Units: } (N \cdot m) \int_0^{r_p(z)} \left(\frac{\text{atoms}}{m^3} \right) \left(\frac{m^2}{2} \right)$$

Derivations completed by consulting References 13-14.

APPENDIX B

Diagram of Neutral Ingestion Effects on MadHeX Replica

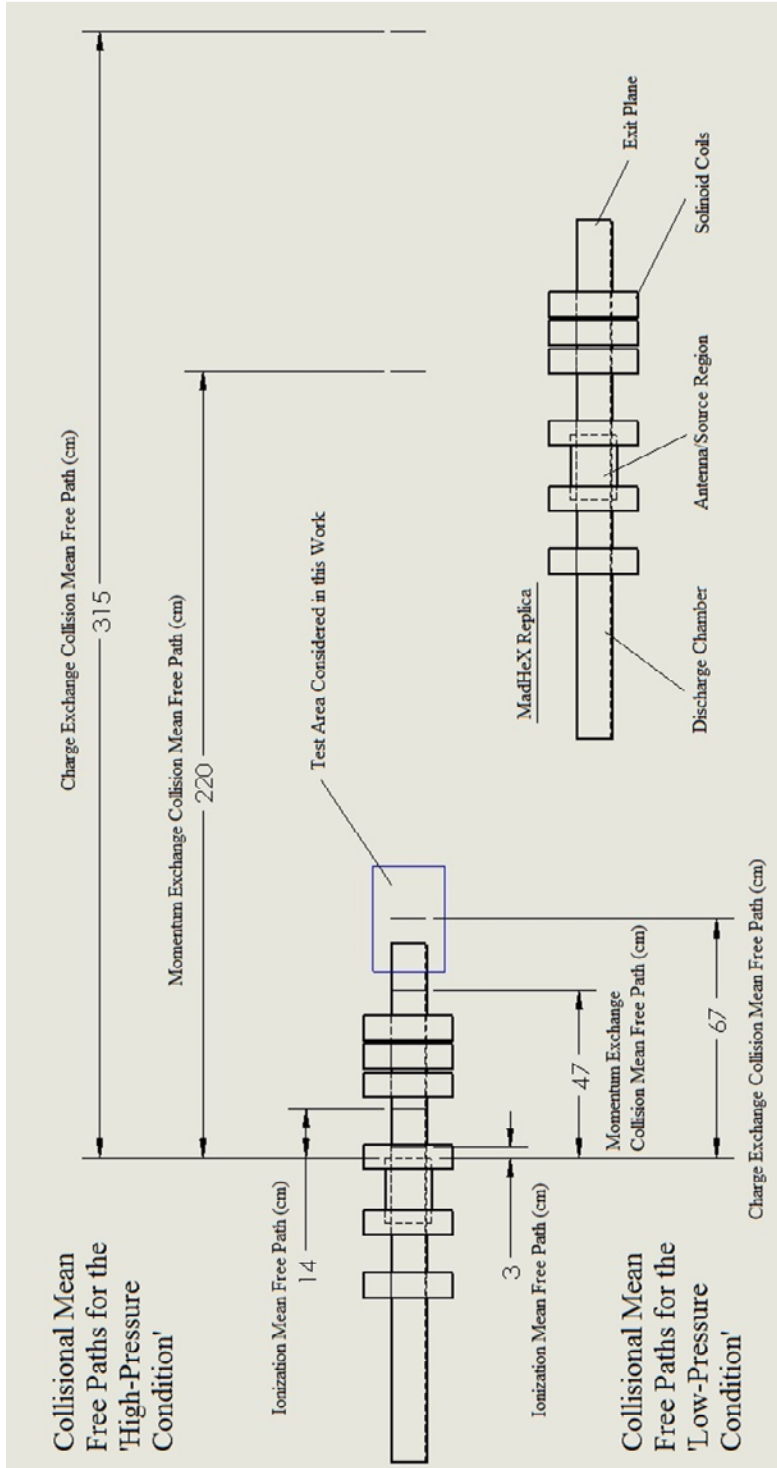


Figure B.1: Diagram of collision mean free paths resulting from neutral ingestion at both pressure conditions for MadHeX replica operation at 2 sccm argon volumetric flow rate, 340 G source region magnetic field strength, and 100 W RF forward power. Diagram is to scale.

REFERENCES

1. Goebel, D., and Katz, I., *Fundamentals of Electric Propulsion: Ion and Hall Thrusters*, John Wiley & Sons, Inc., New Jersey, 2008.
2. Aanesland, A., et al., "The PEGASES gridded ion-ion thruster performance and predictions" *33rd International Electric Propulsion Conference*, The George Washington University, Washington, D.C., 2013.
3. Semenkin, A., et al., "Development of Electric Propulsion Standards-Current Status and Further Activity," *27th International Electric Propulsion Conference*, Electric Rocket Propulsion Society, IEPC Paper 2001-070, Pasadena, California, 2001.
4. Hofer, R., Peterson, P., & Gallimore, A. "Characterizing Vacuum Facility Backpressure Effects on the Performance of a Hall Thruster," *27th International Electric Propulsion Conference*, Pasadena, Ca. 2001.
5. Crofton, M. & Boyd, I., "Momentum Modeling of a Hall Thruster Plume," *33rd International Electric Propulsion Conference*, The George Washington University, Washington, D.C., 2013.
6. Chen, F.F., *Introduction to Plasma Physics and Controlled Fusion Vol. 1: Plasma Physics 2nd Ed.*, Plenum Press, New York, 1984
7. Wiebold, M., "The Effect of Radio-Frequency Self Bias on Ion Acceleration in Expanding Argon Plasmas in Helicon Sources," Ph.D. Dissertation, Electrical and Computer Engineering Dept., University of Wisconsin - Madison, Madison, WI, 2011
8. Schloeder, N., Frieman, J., & Walker, M., "Facility Effects on Helicon Plasma Source Operation," *50th Joint Propulsion Conference*, JPC Paper, Cleveland, Ohio, 2014.
9. Williams, L., "Ion Acceleration Mechanisms of Helicon Thrusters," Ph.D. Dissertation, Aerospace Engineering Dept., Georgia Institute of Technology, Atlanta, Ga, 2013.
10. Lafleur, T., Charles, C., & Boswell, R. W. "Detailed plasma potential measurements in a radio-frequency expanding plasma obtained from various electrostatic probes," *Phys. Plasmas*. 16 044510, 2009.
11. West, M., Charles, C., & Boswell, R., "Testing a Helicon Double Layer Thruster Immersed in a Space-Simulation Chamber," *Journal of Propulsion and Power*, Vol 24, No. 1. 2008.
12. Chen, F.F., & Chevalier, G., "Experiments on Helicon Plasma Sources," *J. Vac. Sci. Technol. A* 10. 1992.
13. Takahashi, K., et al., "Effect of Magnetic and Physical Nozzles on Plasma Thruster Performance," *Plasma Sources Sci. Technol.* 23 044004, 2014.

14. Fruchtman, A. "The Thrust of a Collisional-Plasma Source," *IEEE Transactions on Plasma Science*, Vol 39. No. 1, 2011.
15. Navarro-Cavalle, et al., "Helicon Plasma Thrusters: Prototypes and Advances on Modeling," *33rd International Electric Propulsion Conference*, The George Washington University, Washington, D.C., 2013.
16. Franck, C. M., Grulke, O., & Klinger, T. "Mode Transitions in Helicon Discharges," *Physics of Plasmas*, 10, No. 1, 2003.
17. Charles, C., & Boswell, R. "The Magnetic-Field-Induced Transition from an Expanding Plasma to a Double Layer Containing Expanding Plasma," *Appl. Phys. Lett.* 91, 201505 (2007)
18. Charles, C., & Boswell, R., 'Current-free Double-Layer Formation in a High-density Helicon Discharge', *Applied Physics Letters*, vol. 82, no. 9, 2003.
19. Charles, C., 'A review of recent laboratory double Layer experiments', *Plasma Sources Science and Technology*, vol. 16, 2007.
20. Gahan, D., et al., "Retarding Field Analyzer for Ion Energy Distribution Measurement Through a Radio-Frequency or Pulsed Biased Sheath," *Plasma Proc. & Poly*, 2009
21. Wiebold, M., Sung, Y., & Scharer, J. E., "Experimental observation of ion beams in the Madison Helicon eXperiment," *Physics of Plasmas*, Vol. 18, No. 6, 2011.
22. Wiebold, M., Sung, Y., & Scharer, J. E., "Ion acceleration in a Helicon source due to the self-bias effect," *Physics of Plasmas*, Vol. 19, No. 5, 2012.
23. Charles, C. "TOPICAL REVIEW: Plasma for spacecraft propulsion." *J. Phys. D: Appl. Phys.* 42 163001, 2009.
24. Vincenti, G. & Kruger, C., *Introduction to Physical Gas Dynamics*, Robert E. Krieger Publishing Company, Malabar, Florida 1982
25. Randolph, et al., "Facility Effects on SPT Thruster Testing," *23rd International Electric Propulsion Conference*, Seattle, Washington, D.C., 1993.
26. Snyder, J. S., et al., "Flow Control and Measurement in Electric Propulsion Systems: Towards an AIAA Reference Standard," *33rd International Electric Propulsion Conference, Electric Rocket Propulsion Society, IEPC 2013-425*. The George Washington University, Washington, D.C., 2013.
27. Williams, L. T., & Walker, M. L. R., "Thrust Measurements of a RF Plasma Source," *Journal of Propulsion and Power*, Vol. 29, No. 3, 2013
28. Tilford, C. R., "Sensitivity of hot cathode ionization gages," *J. Vac. Sci. Technol. A* 3, 1985
29. J P Sheehan, J. P. & Hershkowitz, N. "TOPICAL REVIEW: Emissive probes," *Plasma Sources Sci. Technol.* 20 063001, 2011.

30. Demidov, V., Ratynskaia, S., & Rypdal, K. "Electric probes for plasmas: The link between theory and instrument," *Review of Scientific Instruments* 73 3409, 2002.
31. Keithley Product Specifications, *Series 2400 Data Sheet*, Keithley Instruments Inc., pg. 5.
32. Keithley Product Specifications, *Model 6485 Picoammeter Instruction Manual*, Keithley Instruments Inc., pg A-2, 2001.
33. Xu, K.G., "Ion Collimation and In-Channel Potential Shaping using In-Channel Electrodes for Hall-Effect Thruster," Ph.D. Dissertation, Aerospace Engineering Dept., Georgia Institute of Technology, Atlanta, Ga, 2012.
34. Brown, D. L. "Investigation of Low Discharge Voltage Hall Thruster Characteristics and Evaluation of Loss Mechanism," Aerospace Engineering Vol. Ph.D. Dissertation, University of Michigan, Ann Arbor, MI, 2009
35. Reid, B. M., "The Influence of Neutral Flow Rate in the Operation of Hall Thrusters," *Aerospace Engineering*, Ph.D. Dissertation, University of Michigan, Ann Arbor MI, 2009.
36. Campanell, M.D., "Negative Plasma Potential Relative to Electron-Emitting Surfaces," *Phys. Rev. E*. 88. 2013.
37. Phelps, A.V., "Cross Sections and Swarm Coefficients for Nitrogen Ions and Neutrals in N₂ and Argon Ions and Neutrals in Ar for Energies from 0.1 eV to 10 keV," *J. Phys. Chem.* Vol. 20, No. 3, 1991.
38. Raju, G., "Electron-atom Collision Cross Sections in Argon: An Analysis and Comments," *IEEE Transactions on Dielectrics and Electrical Insulation*, Vol. 11, No. 4, 2004.
39. Little, J., "Magnetic Nozzle Plasma Dynamics and Detachment," Electric Propulsion and Plasma Dynamics Lab, <http://alfven.princeton.edu/projects/MagneticNozzle.htm> 2016.
40. Cow, W., et al. "Spatial Retarding Field Energy Analyzer Measurements Downstream of a Helicon Double Layer Plasma," *Appl. Phys. Lett.* 93. 2008.
41. Godyak, V., "TOPICAL REVIEW: Ferromagnetic Enhanced Inductive Plasma Sources," *J. Phys. D: Appl. Phys.* 46. 2013.
42. Bose, D., Govindan, T., & Meyyappan, M., "Modelling of Magnetic Field Profile Effects in a Helicon Source," *Plasma Sources Science and Technology*, Vol. 13, No. 4, 2004.
43. Fossum, E., & King, L., "Effects of Neutral Density on Electron Temperature and Mobility in a Crossed-field Trap," *44th Joint Propulsion Conference, JPC Paper*, Hartford, CT. 2008.
44. Lee, M., Ku, J., Hwang, K., & Chung, C., "Electron Temperature Control by an External Magnetic Field in Solenoidal Inductive Discharge," *Physics of Plasmas*, 16, 2009.
45. Fukano, A., & Hatayama, A., "Electric Potential in Plasma and Sheath Regions with Magnetic Field Increasing toward a Wall," *J. Plasma Fusion Res.* Vol. 9. 2010.